Copyright

by

Jasmina Pozderac Marsh

2006

The Dissertation Committee for Jasmina Pozderac Marsh
Certifies that this is the approved version of the following dissertation:

Production and Evaluation of Silicon Diffractive Optics for Infrared Astronomy

Committee:

Daniel T. Jaffe, Supervisor

Christopher A. Sneden

Neal J. Evans II

Gary J. Hill

John H. Lacy

Alan T. Tokunaga

PRODUCTION AND EVALUATION OF SILICON DIFFRACTIVE OPTICS FOR INFRARED ASTRONOMY

by

JASMINA POZDERAC MARSH, B.S.; M.S.

DISSERTATION

Presented to the Faculty of the Graduate School of

The University of Texas at Austin

in Partial Fulfillment

of the Requirements

for the Degree of

DOCTOR OF PHILOSOPHY

THE UNIVERSITY OF TEXAS AT AUSTIN

August 2006

Dedication

This dissertation is dedicated to my parents, Nadira and Ibrahim Pozderac, who always encouraged me to pursue my goals.

Acknowledgements

I would like to thank Dan Jaffe for taking me as his student and for his patience and guidance. Members of my dissertation committee, with their helpful advice and guidance, have made both the project and the dissertation interesting and challenging. I would also like to mention Oleg Ershov who taught me the techniques of silicon crystal micromachining and diffraction grating and would have been an excellent teacher of Russian language had he not passed away four years ago. Douglas Mar, who has taken Oleg's place, has been an invaluable source of information having a different perspective on silicon micromachining as well as a great person to work with. His optimism and willingness to work on a problem until it is solved is one of the main reasons for the success of our project. Many people from many different areas of expertise have contributed along the way to make this dissertation possible. I would like to thank Luke Keller and Greg Doppmann for their advice and guidance in all issues varying from spectroscopy and diffraction gratings to graduate school; Jimmy Welborne and George Barczak for making various custom pieces of processing equipment as well as upgrades to our clean room; Hao Ling and Hosung Choo for their continuing support of our project through the development of their grating efficiency modeling code and the application of that code to our gratings; Katelyn Allers for RIE process development; and many others at the Center for Nanomaterials and Microelectronics Research Center who contributed

their time and knowledge and helped us with equipment training and troubleshooting. Finally, I would like to mention my friends and colleagues Jennifer Simmerer and Diane Paulson. It is they who finally made me feel at home again.

Production and Evaluation of Silicon Diffractive Optics for Infrared Astronomy

Publication No._____

Jasmina Pozderac Marsh, Ph.D

The University of Texas at Austin, 2006

Supervisor: Daniel T. Jaffe

The silicon diffractive optics we have been developing over the past 15 years have reached the level where they compete with and, in some cases, exceed the performance of commercially available diffraction gratings. The main goal of our program is to produce high quality immersion gratings with coarsely spaced grooves appropriate for use in the near-infrared (1.1 - 5 μm), as well as a set of grisms for the near-IR and longer wavelength bands (5 - 35 μm). We tested all gratings as front-surface devices as well as immersed gratings or grisms. Results of our testing show that our echelles behave according to the predictions of the scalar efficiency model and that tests done on front surfaces are in good agreement with tests done in immersion. Relative efficiencies of all gratings were better than 60% and as high as 97% at 632.8 nm. All gratings except our older prototype had diffraction limited performance at 632.8 nm.

Having produced several diffraction gratings on silicon substrates up to 75 mm in diameter, we evaluate the current state of the silicon grating technology as well as discuss further developments necessary for making gratings on larger silicon substrates.

Table of Contents

List of Tables

List of Figures

Chapter 1.

Introduction

The goal of this dissertation is to describe the manufacturing process and testing of silicon diffraction gratings, a novel technology for infrared spectroscopy. Gratings with grooves immersed in a material with the index of refraction *n* and with the incident beam passing through the material before hitting the grating are called immersion gratings. An immersion grating can be manufactured on a hypotenuse of a prism made of a dielectric material with a high index of refraction. Silicon is a particularly interesting material in the infrared because of its high index of refraction ($n \sim 3.4$) and good material properties. Silicon immersion gratings offer significant improvements over front surface devices in areas of resolving power and angular dispersion while maintaining small grating dimensions. Silicon grisms not only offer increased resolving power and dispersion over grisms made with currently used materials but also enable us to make very compact straight through cross-dispersed systems using two silicon grisms.

Current high resolution spectrographs for observations at 1-5 μm include PHOENIX on Gemini South (Hinkle et al. 1998), CSHELL on IRTF (Greene et al. 1993), NIRSPEC on Keck Telescope (McLean et al. 1998), and CRIRES on VLT (Wiedemann et al. 2000). Only NIRSPEC is a cross-dispersed spectrograph while the other three are single order instruments. None offer a continuous spectral coverage of more than a small fraction of the wavelength within a given atmospheric window. The maximum resolving power of these instruments ranges from 20,000 to 70,000. If one were to increase the resolving power, it would be at the expense of slit width (currently in the range 0.15”-

0.25” for 8 m telescopes), thus decreasing throughput for seeing-limited systems. A new instrument with higher resolving power would need a larger grating length to achieve the improvement while keeping the slit size constant. The existing instruments do not satisfy the needs of the astronomical community for a cross-dispersed near-IR instrument with high resolving power (up to 100,000) with simultaneous coverage of a large range of continuous wavelengths.

The resolving power of a diffraction grating scales as the beam diameter divided by wavelength. The beam diameter is equal to the product of the length of the used area of the grating and the cosine of the blaze angle. While most conventional gratings aim at increasing the resolving power by increasing either the length of the grating, the blaze angle or both, another approach was offered by Hulthén and Neuhaus (1954). It involves decreasing the effective wavelength at which the grating operates. The wavelength decrease comes from immersing the grating inside a transparent medium so that light passes through the medium before reaching the grating. The effective wavelength of an “immersion grating” is decreased by the index of refraction of the medium thus increasing resolving power by a corresponding factor for a given grating length.

The idea of immersing the grating in a transparent medium is actually much older than the references normally made to it in the current literature and dates back to Fraunhofer (1822). He experimentally determined the grating equation inside a refracting medium by immersing his gratings in various liquids. Hulthén and Neuhaus rediscovered the idea in 1954 but it was not immediately implemented. Immersion gratings for visible wavelengths did not offer a great promise because the available materials for visible wavelengths have small indices of refraction ($n \sim 1.5$). Not until semiconductor materials became available and processing techniques became feasible has this idea been taken up again. A number of new materials with high indices of refraction became available for

use in infrared systems. The advantage of using these materials to make IR spectrographs more compact lies not only in the larger size reduction factor enabled by the high index of refraction (n ~ 3-4) but also in the fact that thermal background makes it necessary to cool the spectrographs to cryogenic temperatures, something that is not normally necessary at visible wavelengths. Among many materials used in IR systems, silicon is one of the most important ones. The material properties of silicon are very well matched to cryogenically cooled infrared systems and its index of refraction is among highest available. Also, the advent and rapid development of Very Large Scale Integration (VLSI) and micromachining technology has given us access to large quantities of inexpensive yet pure monocrystalline silicon as well as to two decades of manufacturing experience and processing equipment. The first silicon gratings were chemically etched on thin wafers in 1975 (Tsang & Wang 1975). However, silicon processing equipment was available only for small substrate sizes and thicknesses (up to 2" in diameter and 1 mm thick) until early 1990s. Since then, the rapid increase in the size of available silicon substrates forced the faster technological development of silicon processing equipment. The development of diffraction gratings chemically micromachined on large, bulky silicon substrates for astronomical applications has followed.

We have used the existing knowledge and expertise of Micro-Electro-Mechanical Systems industry to develop gratings chemically etched in silicon and optimize them for spectroscopic applications. In Chapter 2, we describe our current manufacturing process for making silicon immersion gratings on large substrates. Our current gratings are manufactured on substrates up to 4" in diameter and up to 1" thick. An R2 echelle grating recently completed is an example of the current state of art of immersion echelles. We are currently able to manufacture gratings that are appropriate for high resolution

cross-dispersed near-IR spectrographs (resolving power from 50,000 to 100,000). The results of tests performed at several wavelengths on our completed echelles are analyzed. We measured relative efficiencies of our echelles both as front surface and as immersion devices. Diffraction limited performance was tested using interferometric tests and direct observation of the point-spread function of the gratings. We also performed a detailed analysis of grating defects (scattered light in grass, diffuse scattered light and ghosts) to determine where the bulk of the wave front error is coming from.

In Chapter 3, we report on the results of the testing and analysis of our old prototype grating. The results are significant because the technology used for the production of the prototype is simpler and more inexpensive and can be used for mass production of silicon gratings if one is not concerned with diffraction limited performance at the shortest wavelengths (1.1-2 μm).

Silicon grisms were a natural by-product of our echelle program. The requirements on the quality of grating patterns is easier to meet for grisms than it is for immersion grating by a factor of $2n/(n-1)$ and they were easy to make compared to immersion gratings. The results of our grism program are described in Chapter 4. In addition to the grism manufacturing process and performance of the completed grisms, we discuss the transmission of silicon from 5-35 μm and the limitations of using silicon grisms over the entire range.

Finally, Chapter 5 is devoted to summarizing the current state of art of making gratings on silicon substrates and discussing future improvements and changes. The next generation of immersion gratings will be manufactured on substrates up to 12" in diameter and diffraction limited resolving powers of $\sim 10^6/\lambda$. The Giant Magellan Telescope Near-Infrared Spectrograph (GMTNIRS) for the Giant Magellan Telescope has been proposed to enable large instantaneous coverage at very high resolving power

(2×10^4 - 2×10^5) by utilizing such a grating. However, large gratings necessitate changes to our process and we will discuss some technological improvements to our process that are either available now or will become available in the near future.

Chapter 2.

Silicon Diffraction Gratings and Their Applications as Front-Surface and Immersion Devices

2.1 INTRODUCTION

The University of Texas IR group has spent the last 15 years developing techniques for etching precisely placed grooves into monocrystalline silicon substrates in order to produce silicon grisms (see Chapter 4) and echelle gratings (Graf et al. 1994, Jaffe et al. 1998, Keller et al. 2000, Ershov et al. 2003). The goal of our silicon echelle program is to produce gratings chemically etched in silicon which can be used as immersion echelles from 1.1 to 5 μm.

An immersion grating is a diffraction grating in which the light incident on the grooves passes through a medium with the index of refraction, *n*, greater than 1. Upon being diffracted, light exits through the same entrance face. The advantage of immersion gratings over front-surface devices is that of resolving power vs. grating length (and therefore the overall mass and volume of the grating). The maximum attainable resolving power *R* for an immersion grating when used in Littrow configuration is given by:

$$R = \frac{2nL\sin\delta}{\lambda} = \frac{2nW\tan\delta}{\lambda} = mN \qquad (2.1)$$

where L is the illuminated grating length, W is the beam diameter, δ is the blaze angle, λ is the vacuum wavelength, N is the number of illuminated grooves, and m is the grating order. The difference between a front-surface grating and an immersion grating of the same size is that the wavelength of light in a dielectric is decreased by a factor of n which

makes the phase difference between the extremes of the illuminated parts of the grating surface *n* times larger (see Figure 2.1 *top*, *middle*) and increases the resolving power by the same factor. The grating equation inside the medium is

$$m\lambda = \sigma n(\sin\alpha + \sin\beta) \tag{2.2}$$

where σ is the groove period, α and β are the incident and diffracted angles inside the material, and λ is the vacuum wavelength. Eq. 2.2 implies that the immersed echelle is operating in an order which is *n* times the order of a non-immersed echelle. In addition to the increased resolving power of an immersion grating compared to a front-surface device of the same size, another advantage of immersion gratings is the large angular dispersion and compactness of orders. The angular dispersion, $d\beta/d\lambda$ is given by

$$\frac{d\beta}{d\lambda} = \frac{m}{\sigma\cos\delta} = \frac{\sin\alpha + \sin\beta}{\lambda\cos\beta} \tag{2.3}$$

where α and β are the incident and diffracted angles outside the material.

The *n*-fold increase in the angular dispersion of an immersed echelle can be thought of as resulting from the refraction of light exiting the material-air interface or as resulting from the grating operating in order m which is *n* times the order of the front surface grating at the same wavelength. The light exiting the material is diffracted according to the Snell's law resulting in the high angular dispersion of the immersed grating. The free spectral range (FSR) is given by λ/m and is *n* times smaller when the grating is used in immersion making immersion echelles a perfect choice for compact spectrographs in which a combination of large angular dispersion and small orders are

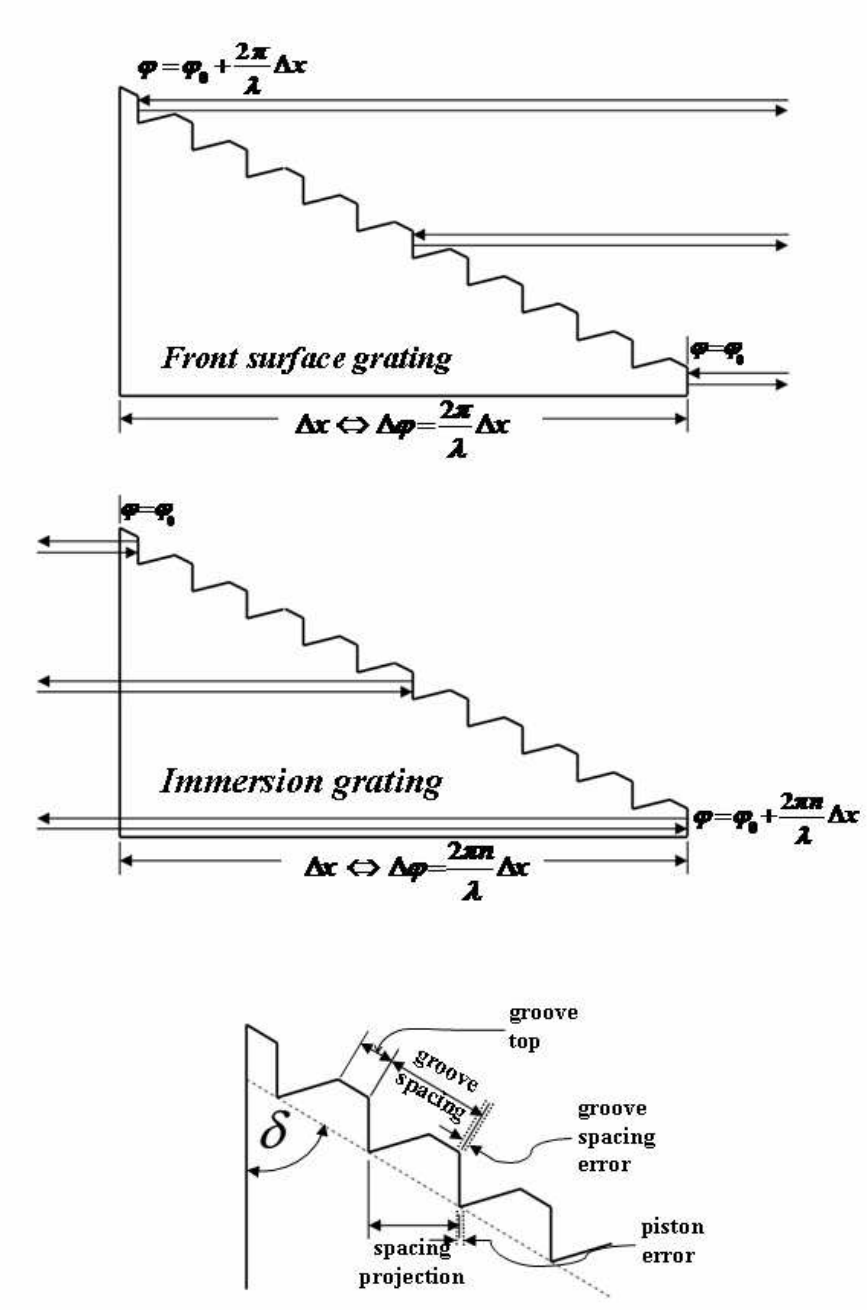

Figure 2.1. Difference in optical paths between a front surface device (*top*) and an immersion grating (*middle*). The phase difference between the first and the last groove is *n* times larger when the light passes through a material with an index of refraction *n* before hitting the grating than for the front surface device. The relationship between the groove spacing error and the phase error is given by $\varepsilon_{spacing}=\varepsilon_{phase}/sin\ \delta$ (*bottom*).

desired. While the increase in the phase difference over the whole illuminated length of the grating due to the immersion of grooves in a dielectric works to our advantage by producing a significant increase in the resolving power of the grating, it also imposes stricter tolerances on the groove positioning (see Figure 2.1, *bottom* and the discussion of tolerances in Section 2.2.1).

The principle of immersion gratings has been known for almost 200 years since Fraunhofer experimentally determined the grating equation for diffractive optics immersed in various fluids (Fraunhofer 1822, Leitner 1975). It was rediscovered by Hulthén and Neuhaus half a century ago (Hulthén & Neuhaus 1954), but not many practical attempts were made to follow up on this concept. The immersion grating concept was patented in 1984 (Sica 1984) and started appearing in astronomical literature in the late 1980s and early 1990s. Early investigations used diffraction gratings immersed in BK7 (Dekker 1987) and quartz (Wynne 1991). These papers mark the shift from using liquids to using glasses and dielectrics as immersing media. In the infrared, silicon became the primary choice for several groups in the early and mid 1990s which experimented with diffraction gratings chemically etched in silicon (Wiedemann & Jennings 1993, Graf et al. 1994, Kuzmenko et al. 1994, Käufl et al. 1998, Ebizuka et al. 1998, Vitali et al. 2000) and remains the top choice even though diamond-machined gratings in germanium (Kuzmenko et al. 2003), ZnS, ZnSe (Smith et al. 1998), and thallium bromoiodade (KRS-5; Rayner 1998) have recently been produced.

The most commonly chosen dielectric for production of infrared grisms and immersion gratings has been silicon not only because it has a high index of refraction (n=3.45 at 1.5 μm) but also because of the rapid technological developments in the semiconductor industry in the past 30 years which enable us to micromachine small structures in silicon. In addition to highly developed technological methods for

production of silicon devices, silicon is readily available in various boule sizes and purities (resistivity from a few Ω cm to a few thousand Ω cm) and is relatively inexpensive unlike other IR materials (see Chapter 4 for the summary of materials suitable for IR diffractive optics). Properties of silicon as a material are very well suited to the needs of IR spectroscopy (Hinkle 1994). Its low coefficient of thermal expansion (between -0.5×10^{-6} K^{-1}@77K and 2.6×10^{-6} K^{-1}@300K) translates into small changes in the blaze wavelength when the grating is cooled and its high thermal conductivity (between 1300 W mK^{-1} @77K and 160 W mK^{-1}@300K) results in short cool-down times for silicon optics inside cryogenic systems. Crystalline silicon has a very small coefficient of absorption from 1.2 to 5 μm (Sze 1981). It transmits light at wavelengths greater than 1.2 μm but the cutoff wavelength shifts to shorter wavelengths at low temperatures (MacFarlane et al. 1958).

A large amount of silicon processing takes advantage of crystal plane geometry of monocrystalline silicon and the effect of anisotropic etchants like aqueous potassium hydroxide (KOH) which etches {100} planes much faster than {111} planes (Bassous 1978). When making a diffraction grating in silicon, if we cut a silicon wafer so that a (100) plane is exposed, the high anisotropy ratio of the KOH etchant solution (anisotropy ratio is the ratio of the etch rates of crystal planes) for (100) and (111) planes will produce symmetric, V-shaped grooves with their walls defined by slow etching (111) planes (Tsang & Wang 1975). The grating will be blazed at 54.74°. We often need echelles and grisms with a blaze angle different than 54.74° resulting from the crystal geometry of (100) oriented wafers, so we expose a surface which does not correspond to any of the major crystal planes (Fujii et al. 1980, Philippe et al. 1985; also see Figure 2.2). The etchant will expose (111) planes in this case as well but the resulting profile

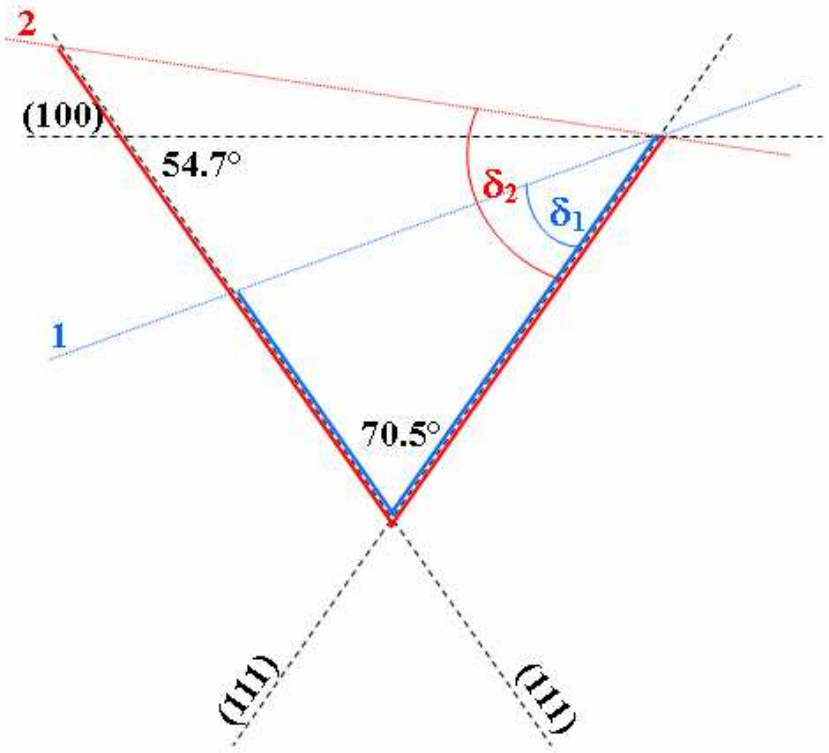

Figure 2.2. Relationship between silicon crystal planes and blaze angle. The positions of the (111) and (100) planes are indicated by dashed lines. Cutting a surface in the silicon boule at the (100) plane results in a blaze at the "natural" angle of 54.74°. Cuts 1 and 2 will result in blaze angles δ_1 (<54.74°) and δ_2 (>54.74°) respectively.

will be asymmetric and blazed at the desired angle δ. An illustration of an immersion grating produced in silicon is shown in Figure 2.3. Light enters through the entrance face and, after hitting the grating inside the material, it is diffracted back toward the entrance face (which now becomes the exit face). At the interface between the prism material and air, light is refracted and produces the final diffraction pattern.

The process of making a monolithic silicon grating consists of many steps shown in Figure 2.4. The basic steps are: growing a boule of silicon, orienting the boule, dicing the boule into disks, polishing disks and coating them with a layer of passivation material, depositing photoresist and transferring a pattern from a photolithographic mask onto photoresist by exposing through the mask, transferring the pattern down onto the passivation layer which now becomes an etch mask, etching grooves in silicon, removing the remaining passivation layer, and shaping the disk into a prism and polishing the entrance face. Coatings can be deposited based on the intended application of the grating. If the grating is used as an immersion grating, then an anti-reflection coating needs to be applied to the entrance face and a reflection coating needs to be applied to the surfaces of grooves.

The groove profile of diffraction gratings etched in silicon differs from that of their ruled counterparts in two ways (see Figures 2.2 and 2.3). The angle between groove sides is determined by silicon crystal geometry or, more specifically, the angle between two (111) planes is 70.5° whereas most ruled gratings have right triangular groove shape. Silicon gratings have a flat groove "top". The flat groove top occurs as a result of the manufacturing process and is also not present in ruled gratings. However, groove tops are irrelevant for high order gratings used in immersion since they are hidden behind groove walls and result in no loss of light.

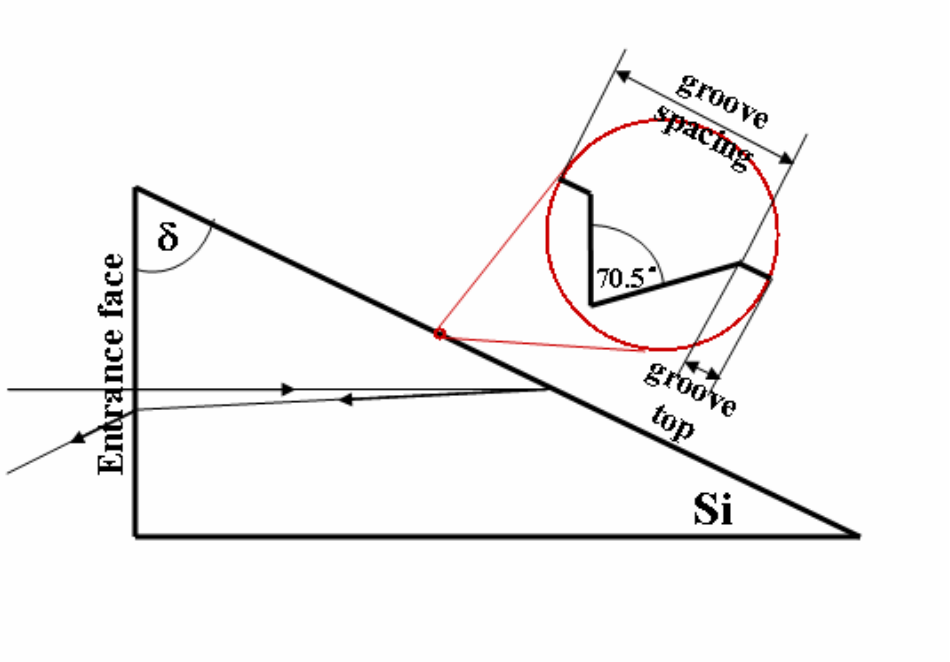

Figure 2.3. Immersion grating etched in silicon. The detail inside the red circle shows the groove geometry resulting from the orientation of crystal planes in silicon.

The effects of the unorthodox groove shape and the remnant groove tops on the efficiency behavior of silicon gratings represented a concern when gratings were used as front-surface devices. When used in high orders, gratings operate in the scalar limit and the efficiency performance of an error-free silicon immersion grating is indistinguishable from that of an error-free ruled grating with the same groove constant. However, in low orders, a more rigorous approach using vector modeling should be used because the wavelength at which the grating operates is a significant fraction of the groove width and grooves are no longer simple reflecting surfaces (Loewen et al. 1977). Our group investigated the efficiency behavior of low-order gratings (Moore et al. 1992) before we began extensively experimenting with methods to make gratings on thick substrates. Graf et al. (1994) measured the efficiency of our first gratings produced on silicon wafers and confirmed that no significant differences exist between ruled and etched gratings and that etched gratings are a feasible alternative to ruled gratings.

We outline here the results for three completed gratings (see Table 2.1 for the summary of grating parameters and process details). G1, completely cut and coated, was designed for the use in a spectrograph proposed for the NASA IRTF telescope (Immersion Grating Echelle Spectrograph, ImGES). Its predecessor G0, also completely cut and coated, was the first grating we successfully etched on a thick silicon substrate and we used it as a prototype in order to test many concepts which we subsequently applied to G1. G1's successor G3 is a completed grating, cut but not yet coated. In Section 2.2, we will talk about the process of chemically ruling grooves into silicon crystal as well as tolerances. Section 2.3 contains results from tests performed on our gratings and the analysis of errors and their sources. In Section 2.4, we summarize the results of our research up to date.

Table 2.1. Summary of grating parameters of the gratings discussed in this dissertation.

Grating	Blaze angle	Groove spacing	Groove top	Passivation material	Mask
G0	54.7°	142 μm	10 μm	6000 Å of thermal oxide	Ruled
G1	63.4°	80 μm	6 μm	600 Å of silicon nitride	Photolithographic
G3	32.6°	87 μm	6 μm	600 Å of silicon nitride	Photolithographic

2.2 MATERIAL PROCESSING

There are three distinct stages in the process of etching grooves in silicon: substrate preparation (outsourced to contractors which include growing the boule, orientation, cutting, polishing and coating), production of the grooves (chemical "ruling"), and shaping and coating for use in immersion. Figure 2.4 is a flow chart of our process whose details are discussed in Sections 2.2.2 – 2.2.5.

2.2.1 Tolerances

We will now examine the strict requirements during key steps of the process of making gratings on bulk silicon substrates. The tolerances at each step are determined by our goal to make an echelle grating with >80% peak blaze efficiency in immersion at 2 μm (Jaffe et al. 1998). From the standpoint of sensitivity to manufacturing errors, a silicon immersion grating operating at 2 μm is equivalent to a front-surface device operating at 580 nm. To get an initial estimate, we assumed that all errors are due to randomly misplaced grooves which produce wave fronts out of phase with the rest of the grating. These wave fronts are not completely able to interfere constructively with the light coming from periodically placed groove facets and some of the light therefore propagates in undesired directions. We used the following formula to estimate the allowable RMS groove positioning error (Mahajan 2001):

$$\frac{\eta}{\eta_0} = \exp\left[-\left(\frac{2\pi}{\lambda} 2\varepsilon_{RMS}\right)^2\right] \tag{2.4}$$

where η is the grating efficiency, η_0 is the maximum efficiency, and ε_{RMS} is the RMS wave front error. If the error is a result of the random groove displacement from the

grating constant σ, then the groove placement error $\Delta\sigma_{RMS} = \varepsilon_{RMS} \sin \delta$. For η/η_0>80%, the maximum allowable wave front error is ε_{RMS} = 22 nm from Eq. 2.4. Assuming we want to make an R2 echelle, the groove placement error can be up to $\Delta\sigma_{RMS}$ =24.6 nm.

Errors in groove positioning can be separated, based on part of the process from which they originate, into errors in the substrate layer flatness, errors in the pattern transfer from the mask to the passivation layer (including errors in the mask itself), and errors in the etching of grooves in silicon. Since errors resulting from each step are uncorrelated, the tolerances imposed on each step are such that errors produce less than $\varepsilon_{RMS}/\sqrt{3}$ =12.7 nm RMS wave front error. We examine each of these errors and how they translate into manufacturing tolerances. In this example, tolerances are calculated for G1 (63.4° blaze angle) but formulae are given so the same calculation can be repeated for different blaze angles.

The first source of error is due to the disk cutting and polishing steps. Uncoated substrates inevitably deviate from a perfectly flat surface. The approximate RMS error of the surface is calculated from the maximum allowable wave front error of 12.7 nm for each source of error. Through groove geometry, we calculate the allowable RMS error of the surface as being equal to 12.7 nm/cos δ = 12.7 nm/cos 63.4° = 28.3 nm RMS or ~λ/20 at 580 nm. This estimate is not exact since the deviation from a perfectly flat surface is more likely to occur on large scales for cutting and polishing errors so the error is not truly Gaussian.

The second source of error is the combined error of the pattern transfer steps (first from the mask to photoresist and then from photoresist to the passivation layer). The mask itself contains errors that propagate through subsequent production steps. If the photoresist thickness varies over the area of the substrate, it will displace images of mask

lines. The final pattern in the passivation layer can deviate from a perfectly periodic pattern by 12.7 nm/sin δ = 12.7 nm/sin 63.4° = 14.2 nm RMS.

Errors during chemical etching of grooves into silicon are the direct result of etch rate variations, both temporal and spatial. The expression for the RMS wave front error resulting from etch rate variations is

$$\frac{\varepsilon_{RMS}}{\sqrt{3}} = \Delta R_{111} t_{etch} = 12.7\,\text{nm} \tag{2.5}$$

ΔR_{111} is the RMS deviation from the mean etch rate in <111> direction and t_{etch} is the time needed to etch a complete groove. Here we decided to neglect the temporal variations in the etch rate because the goal is to keep the etch rate uniform across the whole surface and not necessarily over the whole etch time. If R_{100} is the etch rate in the <100> direction and h is the groove depth, then $t_{etch} = h/ R_{100}$. In all cases, h is the depth of the symmetric groove profile (see Section 2.2.4 for the explanation of etch times), so

$$h = \frac{\sigma - \text{groove top length}}{2} \tan 54.7^{\circ} \tag{2.6}$$

The wave front error is given by

$$\frac{\varepsilon_{RMS}}{\sqrt{3}} = \frac{\Delta R_{111}}{R_{100}} \frac{\sigma - \text{groove top length}}{2} \tan 54.7^{\circ} \tag{2.7}$$

If we want to calculate the etch rate variation allowed during the KOH etch, we can rewrite the above formula

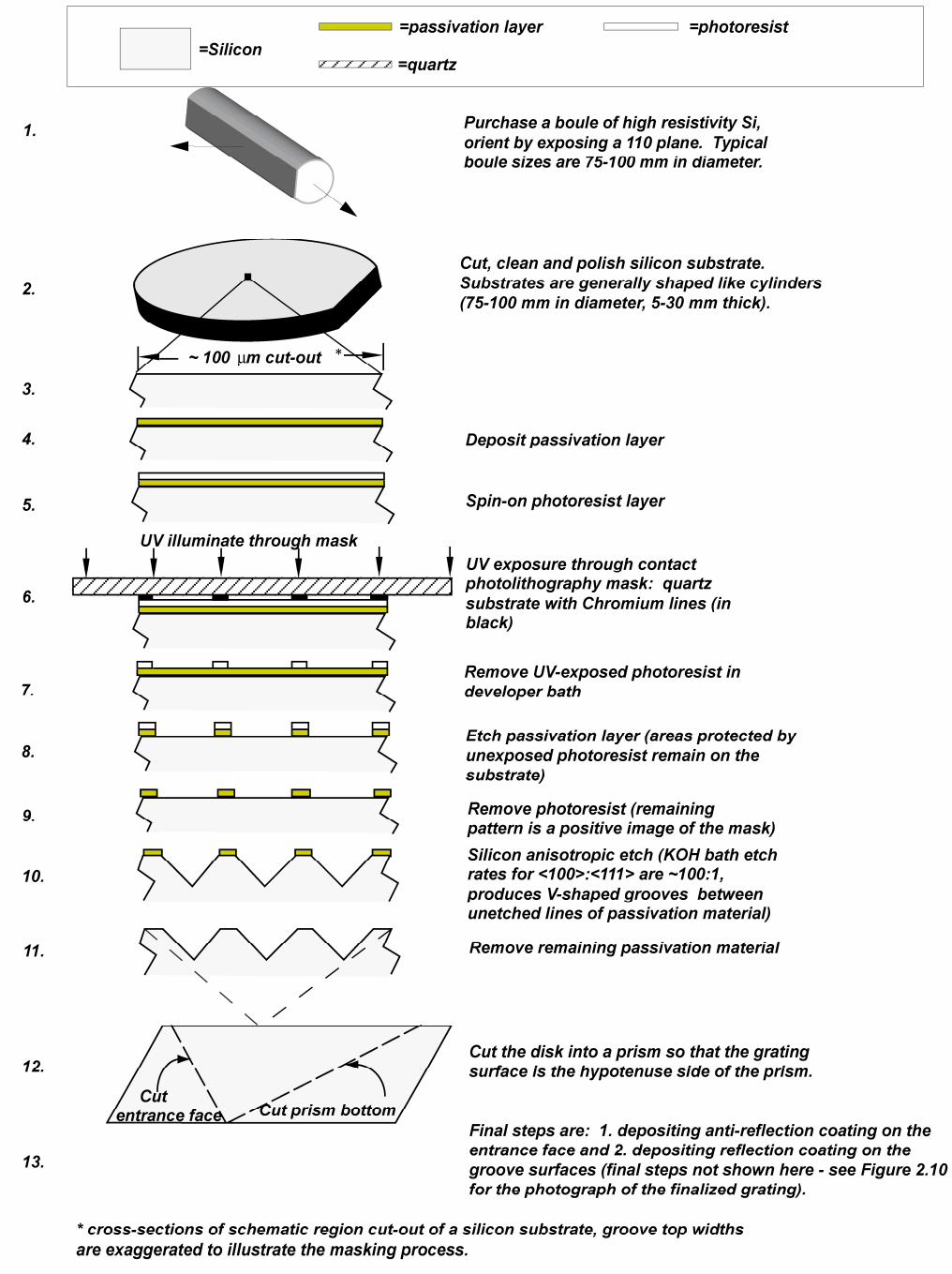

Figure 2.4. Steps involved in chemically “ruling” a grating in silicon material.

$$\frac{\Delta R_{111}}{R_{111}} = 17.8\,\text{nm}\,\frac{R_{100}/R_{111}}{\sigma - \text{groove top length}} \tag{2.8}$$

Now it becomes obvious that having high anisotropy ratios, R_{100}/R_{111}>100, is desirable. For groove periods of approximately 100 μm and anisotropy ratios of ~100, we would need to keep the etching rates constant to within 1-2% across the whole surface of the grating. If the anisotropy ratio dropped to 50, the requirement would be twice as strict and the conditions would have to be such that the etch rates could change by only 0.5-1%.

Even though the flatness of the entrance face is a factor in the performance of the finished device, we found that it is generally not a source of significant error with vendors delivering surfaces with λ/50 flatness or better for immersion gratings with large blaze angles (>30°). It becomes an issue for very thin pieces which are normally used as grisms so we will discuss it in Chapter 4.

2.2.2 Substrate Preparation

Gratings can be etched in silicon substrates of any quality. However, we avoid using substrates with low resistivities and crystals grown using the Czochralski (CZ) method and instead use high purity float-zone (FZ) silicon boules up to 3" in diameter with resistivities of approximately 2000 Ω cm. There are no significant differences in the surface quality of anisotropically etched silicon gratings in CZ vs. FZ type silicon (Kuzmenko & Ciarlo 1998). We already procured high purity FZ silicon for our grism project because of its low oxygen content which improves transmission at several long wavelengths relevant for mid-IR grisms (see Chapter 4). In order to make the subsequent processing steps more convenient and easier, we decided to dice the boule into a set of

disks. We contracted an outside vendor for dicing the boule and polishing disks. Their task was to locate a (110) plane using x-ray diffractometry and grind in a wide flat (~40-50 mm), a so-called precision flat, corresponding to this plane with a precision of 0.05° or better (the boule is illustrated in step 1 in Figure 2.4). The boule was then mounted and diced into disks (step 2 in Figure 2.4) at 8.66° and 22.14° away from the (100) plane (but in opposite directions) toward the (111) planes corresponding to 63.4° and 32.6° blaze angles. Errors larger than 0.05° in grinding the precision flat would result in groove defects, such as dislocations in the groove walls (Kendall 1990). Tilting the boule relative to the (100) plane during the dicing produced asymmetric disks which are not as convenient as circular disks because they are awkward to spin during step 5. The tilt is still necessary in order to blaze gratings at angles different from 54.7° (see Figure 2.2).

These asymmetric disks were ground on one side to desired flatness and then polished using the chemical mechanical polishing (CMP) method which does not cause sub-surface damage to the crystal lattice. The flatness of silicon substrates was measured interferometrically by the polisher. Over the inner 86% of the area of the 3" disk, the RMS error of the polished silicon surface was smaller than $\lambda/100$ at 632.8 nm for all disks, which is well within our tolerances (see Section 2.2.1). In addition to the interferometric tests performed by the vendor, we also tested the surface quality of selected samples by etching them in a KOH solution for several hours. Any subsurface damage would be magnified and made visible during this test since lattice defects and lattice damage represent sites where the etchant can enter the silicon crystal and etch pits and crevices. After inspecting etched substrates visually and with the help of a microscope, we did not notice any damage other than the normal roughening of the surface.

Polished substrates were coated with a passivation layer (step 4 in Figure 2.4). There are two generally accepted materials used as passivation layers for silicon - silicon dioxide and silicon nitride. We have used both in our processing but recently we favored silicon nitride because of its negligible etch rate in KOH solutions. Silicon dioxide has a significant etch rate in KOH of ~100 nm/hr (Kendall & Shoultz 1997) and tends to fail causing groove wall defects (Kuzmenko & Ciarlo 1998, Keller et al. 2000). The typical thickness for an oxide layer is 600 nm and it is limited by the requirement that it be at least as thick as $R_{SiO_2}\, t_{etch}$ (R_{SiO_2} is the etch rate of SiO_2). For a nitride layer, the thickness can be as low as 60-100 nm with the nitride thickness uniformity as good as 5% P-V over the whole surface which is well within our calculated tolerance for substrate flatness. The thickness of the passivation layer also affects the groove positioning errors. Thicker passivation layers tend to cause larger transfer errors thus diminishing grating performance (Jaffe et al. 1998).

2.2.3 Pattern Transfer

Before we even start the pattern transfer stage, we clean the substrate thoroughly. Each piece is cleaned using acetone, isopropanol, methanol and water. After drying with a stream of dry nitrogen gas, the substrate needs to be baked for 1 hr to evaporate any water and solvent remains.

Standard silicon processing techniques make use of photolithographic masks to define the pattern which needs to be transferred to the passivation layer. We use contact masks consisting of several hundred to several thousand parallel chrome lines (a few μm wide by 50-100 mm long) on quartz substrates. At first, we tried to have the pattern ruled in the chrome layer by a manufacturer of ruled gratings because it was the only way we could use very thick (2") and flat mask substrates. However, we quickly discovered that

the ruled mask suffered from significant periodic errors in the pattern (Keller et al. 2000, Marsh et al. 2003). Since then, we have used photolithographic masks, a standard in VLSI processing. Our supplier is able to produce patterns on 6"×6" quartz substrates which are up to 0.25" thick. These masks tend to flex when they are placed in contact with silicon substrates smaller than the mask surface. We determined that the mask flatness, when placed on a large flat surface, was still better than $\lambda/20$ using an optical flat as reference and observing the number of interference fringes between the optical flat and the mask. When placed in contact with a silicon substrate, however, we observed fringes resulting from the mask flexure. The masks are produced using photolithographic techniques. The quartz substrate is coated first with a uniform chrome coating and then a photoresist layer. The process used to write the pattern on our photolithographic masks uses laser beams to "write" the whole length of the line in one pass in the photoresist layer and the interferometrically controlled stage makes highly accurate line positioning possible (Grenon et al. 1995). The pattern in the chrome layer is produced by etching between unexposed photoresist lines. This process eliminates errors present in ruled masks (ghosts) and older photolithographic masks written using e-beam systems (stitching errors made by writing only small sub areas of the whole pattern in one pass). The mask vendor performed measurements of line positions on a random sample of lines on completed masks. The measured RMS error in line placement (relative to the first measured line) of 5 nm and 10 nm for two tested masks used to make G1 and G3 respectively was well within the required precision (see Section 2.2.1). The patterns defined by the masks now need to be transferred twice until their images are formed in the passivation layer.

The first step in the pattern transfer involves the deposition of a uniform photosensitive organic emulsion (photoresist) on top of the passivation layer and

exposure through the mask (steps 5 and 6 in Figure 2.4). The exposed areas are removed (step 7) thus transferring the mask image to the emulsion. After the initial substrate cleaning and baking, we quickly transfer the substrate to the spin table and mount it in a holder which keeps substrates in place during spinning. The role of the spin table is to spin the substrate up to 3500-4500 RPM spreading primer and photoresist evenly over the whole surface. The primer only promotes the adhesion of the photoresist layer to the passivation layer but has no role in the chemical reaction during the exposure step. We deposit photoresist in the center of the substrate and then spin it for approximately 1 minute. The uniformity of primer+photoresist can be verified by observing the color change across the substrate due to reflection from silicon and interference inside the photoresist layer. Shipley S1805 photoresist produces a layer approximately 500 nm thick. After baking photoresist for 20 minutes to harden it, we are now ready to "write" the pattern in photoresist.

The mask needs to be precisely oriented to the substrate precision flat (either parallel or perpendicular to it) and we do this by manually aligning mask chrome lines and the substrate flat while keeping the mask in the close vicinity of the substrate (without physical contact between the two at this point) with the help of a microscope. If the mask lines deviate by more than 0.1° from the orientation defined by the flat, we start to see defects in grooves such as breaks in grooves and jogs (Kendall 1990, Keller et al. 2000). Once we are satisfied with the mask alignment, we contact the mask with the photoresist and expose uncovered areas between chrome lines using our custom UV-exposure system. The UV exposure system is housed in an enclosure open only on the side where a stage moves in and out of it. At the top is the UV lamp 6” in length whose output is collimated by a parabolic mirror. The series of 6 baffles is positioned directly under the lamp-collimator system in order to reduce stray uncollimated light coming

directly from the lamp. Both the substrate and the mask on top of it are mounted on the moving stage which slides them through the collimated beam of UV light and back out so that the whole area receives the same amount of radiation. After exposure, the substrate is rinsed in a developer solution which dissolves the exposed parts of the photoresist. We now have a positive image of the mask in photoresist. The substrate is then quickly transferred into a water bath to stop the developing process and to clean the remaining developer and exposed photoresist from the surface.

The second stage is the transfer of the mask image formed in photoresist down to the passivation later (step 8 in Figure 2.4). The exact mechanism for removal depends on the type of passivation layer used. For a SiO_2 passivation layer, we need to immerse the substrate in a buffered oxide etch (BOE) which will etch SiO_2 between photoresist lines. The process takes about 15 minutes for a 600 nm thick layer of SiO_2 at room temperature and is followed by a water rinse. The resulting SiO_2 stripe profile is not rectangular but rather bowl-shaped as a result of an isotropic etching of SiO_2 in a BOE solution. The spacing between the stripes will be maintained as long as conditions are uniform across the whole surface of the substrate (temperature and concentration). The isotropic nature of SiO_2 etch in BOE and KOH solutions provides a fundamental limit on the minimum width of mask lines as they have to be sufficiently wide to withstand both etches. For a Si_3N_4 passivation layer, we use reactive ion etcher (RIE) to remove the exposed portions of nitride while the photoresist protected stripes of nitride remain intact. RIE uses a combination of sputtering and chemical reaction to remove the exposed areas of the passivation layer. The PlasmaTherm 790, the etcher we used, employs a combination of trifluoromethane (CHF_3) and oxygen (O_2) gasses to etch silicon nitride. It is optimized for thin wafers (up to a few mm thick) so we found that it was necessary to use focusing rings in order to make the plasma density across the surface of the substrate more

uniform. Our average etch rates for this particular combination of substrate thickness and focusing rings was 350 Å/min which is slightly less than the published rates (Mele et al. 1984) but it was not unexpected due to the lower plasma density close to the upper electrode. After RIE, the remaining photoresist is stripped in acetone (step 9 in Figure 2.4) and we are left with the final etch mask consisting of parallel stripes of SiO_2 or Si_3N_4 on a pure silicon substrate.

2.2.4 Etching Grooves

We are now ready to etch grooves into silicon using a water based KOH etch (step 10 in Figure 2.4). V-shaped grooves in silicon are a result of anisotropic etching of silicon when a rectangular mask is applied. Two major planes in silicon crystal are affected differently by different etchants and, in the case of KOH-H_2O system, the ratio of (100):(111) rates has been reported as high as 400:1 (cited in Madou 1997). In order to produce a good grating, we must minimize errors in groove spacing over a large area (see Figure 2.1, *bottom* for the relationship between groove spacing and phase errors and Section 2.2.1 for the discussion of tolerances). We wanted to optimize the anisotropy ratio to be as high as possible because we wanted to minimize our groove positioning errors which are due (partially) to the undercut created by the finite (111) etch rate. The variation in the undercut rate is a result of varying conditions in the etch solution, so we must keep the temperature and concentration uniform inside the bath in order to keep the etch rate within 1% over the whole area of the substrate. Silicon etch rates in aqueous KOH solutions are empirical and experimental results in the literature vary widely (Kendall & Shultz 1997), so we measured our own rates for both symmetric and asymmetric groove profiles and found that they are almost identical.

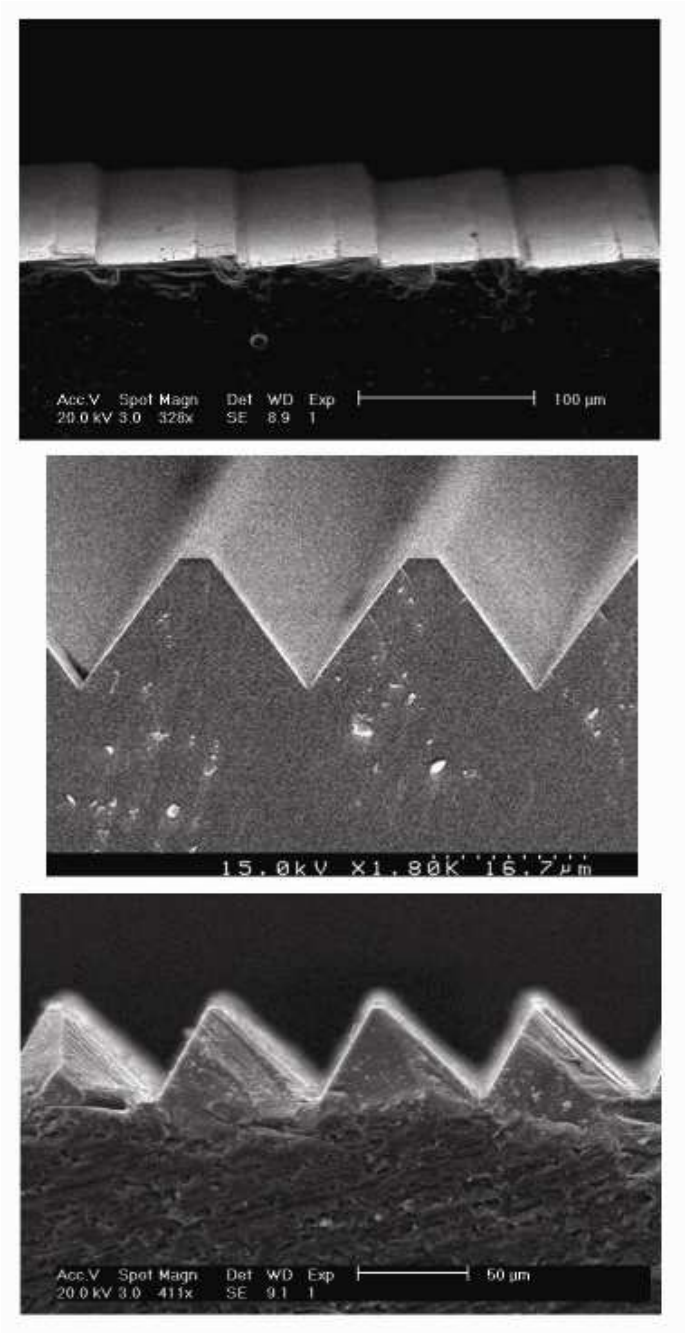

Figure 2.5. SEMs of gratings etched on silicon wafers (Ershov et al. 2003). Shown are gratings blazed at 6.16° (*top*), 54.7° (*middle*), and 63.4° (*bottom*).

The KOH etching apparatus is another custom piece of equipment consisting of an outer container modified into a recirculating bath which keeps the inner container and its contents at constant 68°C (the temperature we determined empirically as providing the maximum etch anisotropy in our etching setup) as well as providing ultrasonic agitation. The 35 wt.% KOH solution is premixed in a beaker and the beaker, once covered, is then used as the inner bath where the etching takes place. Once it has been placed in the outer bath, we add 100-200 mL of isopropanol which serves as a surfactant (Baum and Schiffrin 1997), start the recirculating bath and let the temperature stabilize at 68°C. The substrate is immersed into the etchant. The reaction, which takes place in several steps, can be summarized in this equation (Seidel 1990):

$$Si + 2OH^- + 2H_2O \rightarrow SiO_2(OH)_2^{--} + 2H_2$$

An important by-product of the reaction is molecular hydrogen which forms into bubbles and floats up to the surface of the solution and diffuses into air. However, as they form and grow, these bubbles block the surface of silicon crystal and cause small localized changes in the etch rate resulting in the microroughness of the exposed surface. The addition of isopropanol and the ultrasonic vibrations serves the purpose of promoting quicker detachment of hydrogen bubbles and production of smoother surfaces (Baum and Schiffrin 1997). After the etch time elapses, we quickly transfer the substrate from the KOH etch into a beaker with clean, distilled water to stop the etch. Then, it is transferred into a second beaker, also filled with distilled water, where it stays for at least 15 min in order to thoroughly rinse the substrate. We have produced gratings on large silicon disks with various blaze angles and groove periods (see Figure 2.5). The scanning electron

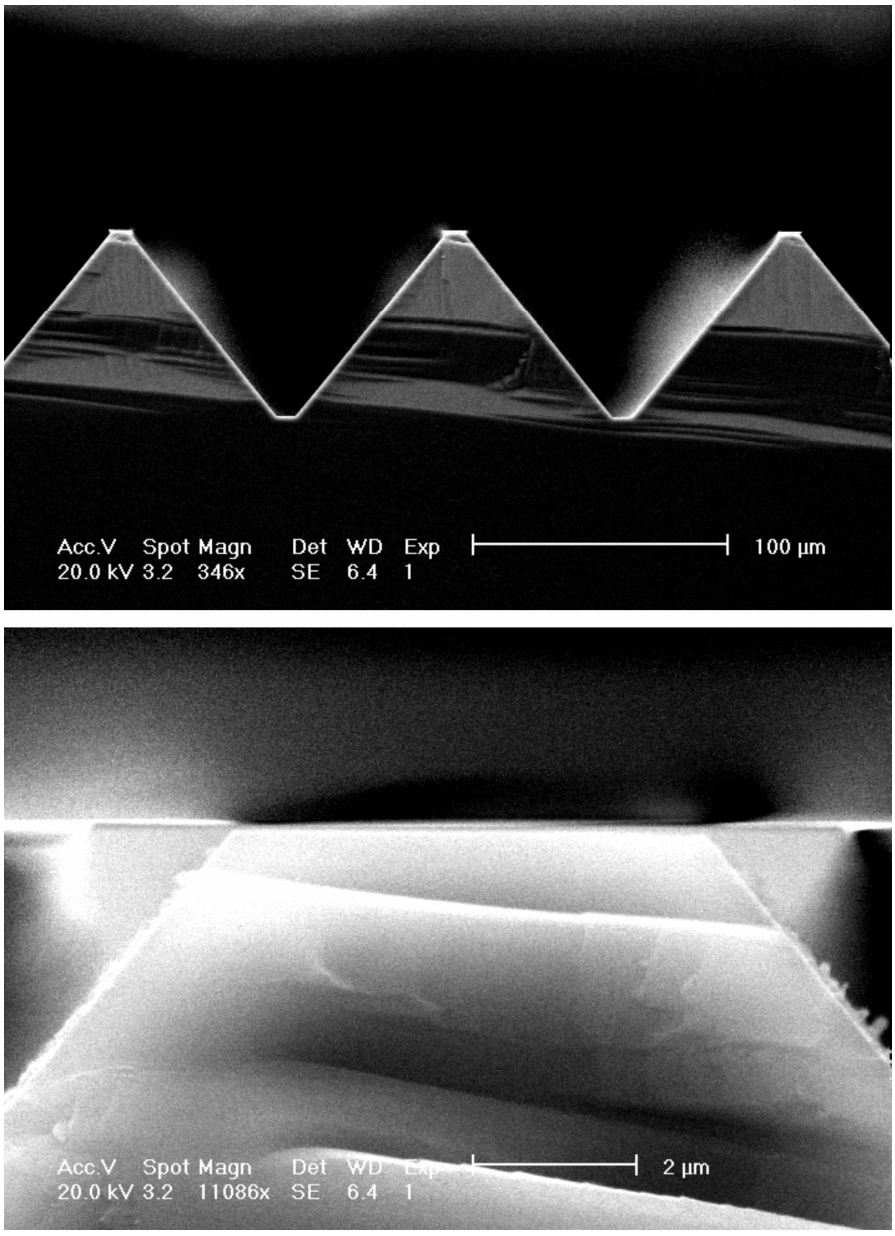

Figure 2.6. We used SEMs of etched gratings to determine etch rates R_{100} and R_{111} for (100) and (111) planes. R_{100} is calculated by measuring the etch depth from the top SEM (etching was not completed so that we could accurately determine the etch depth) and dividing by the etch time. R_{111} is determined from the bottom SEM by measuring length of exposed silicon nitride layer and multiplying that length by sin 54.7°

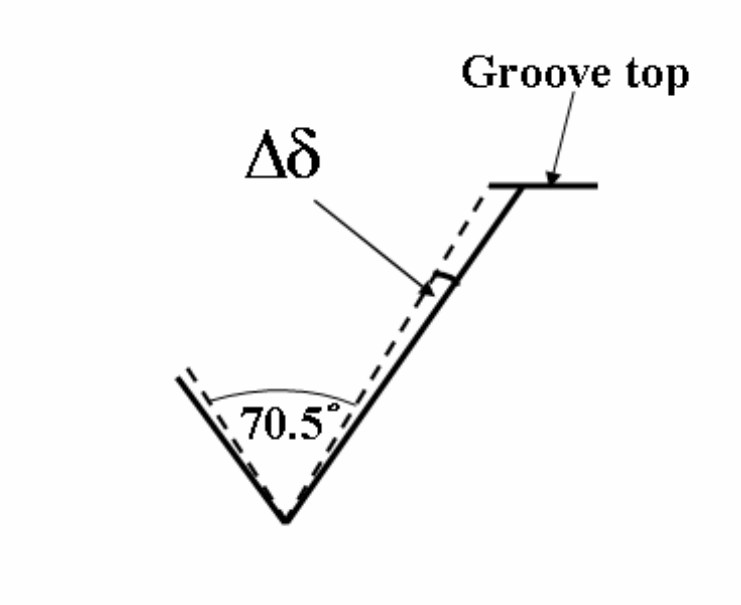

Figure 2.7. Material at the top of the groove is exposed to the etchant for longer than material near the vertex. As a result, the opening angle of the groove increases with time causing a change in the blaze angle.

microscope (SEM) and profilometer were indispensable tools in directly measuring etch rates and anisotropy ratios and we used them to fine-tune the etch times for our chosen temperature and KOH concentration. We can measure horizontal and, to some extent, vertical distances from SEM images. The etch rates are determined from SEM images by measuring the etched depth in the <100> and <111> directions and dividing each by the etch time (see Figure 2.6). Our measurements result in R_{100} = 28 μm/hr and R_{111} = 0.46 μm/hr. The anisotropy ratio is R_{100}/ R_{111} = 60 which fell short of the desired value of 100 (see Section 2.2.1). Because the finite (111) etch rate causes the angle at the groove bottom to differ from the ideal 70.5° (see Figure 2.7), we can also use the vertex angle measured with a profilometer to determine the anisotropic etch ratio. We found the rate of change in this angle to be 0.4°/hour and inferred an anisotropy ratio R_{100}/ R_{111} = 69, in good agreement with the value determined from the SEM measurement of the mask undercut. One implication of this result is that, in order to attain the desired blaze angle, the finite value of the (111) etch rate must be taken into account during the design and material cutting. For example, after etching G1 for 2 hours, the blaze angle has changed from 63.4° to approximately 63.0°. At 2 μm in immersion, when the grating is operated in the 247th order, the blaze wavelength will shift from the predicted 1.998 μm for δ = 63.4° to 1.991 μm for δ = 63.0°, a shift of -0.007 μm, or approximately one full order.

2.2.5 Shaping and coating

We now have a diffraction grating etched into the surface of a thick disk. Before we send it out for shaping into a prism, we need to strip the remaining etch mask (step 11 in Figure 2.4). To etch the remaining silicon nitride strips, we suspend the grating (or the whole disk if one wishes to clean the back side as well) in a commercially available concentrated phosphoric acid solution (85%) close to the boiling point (158°C).

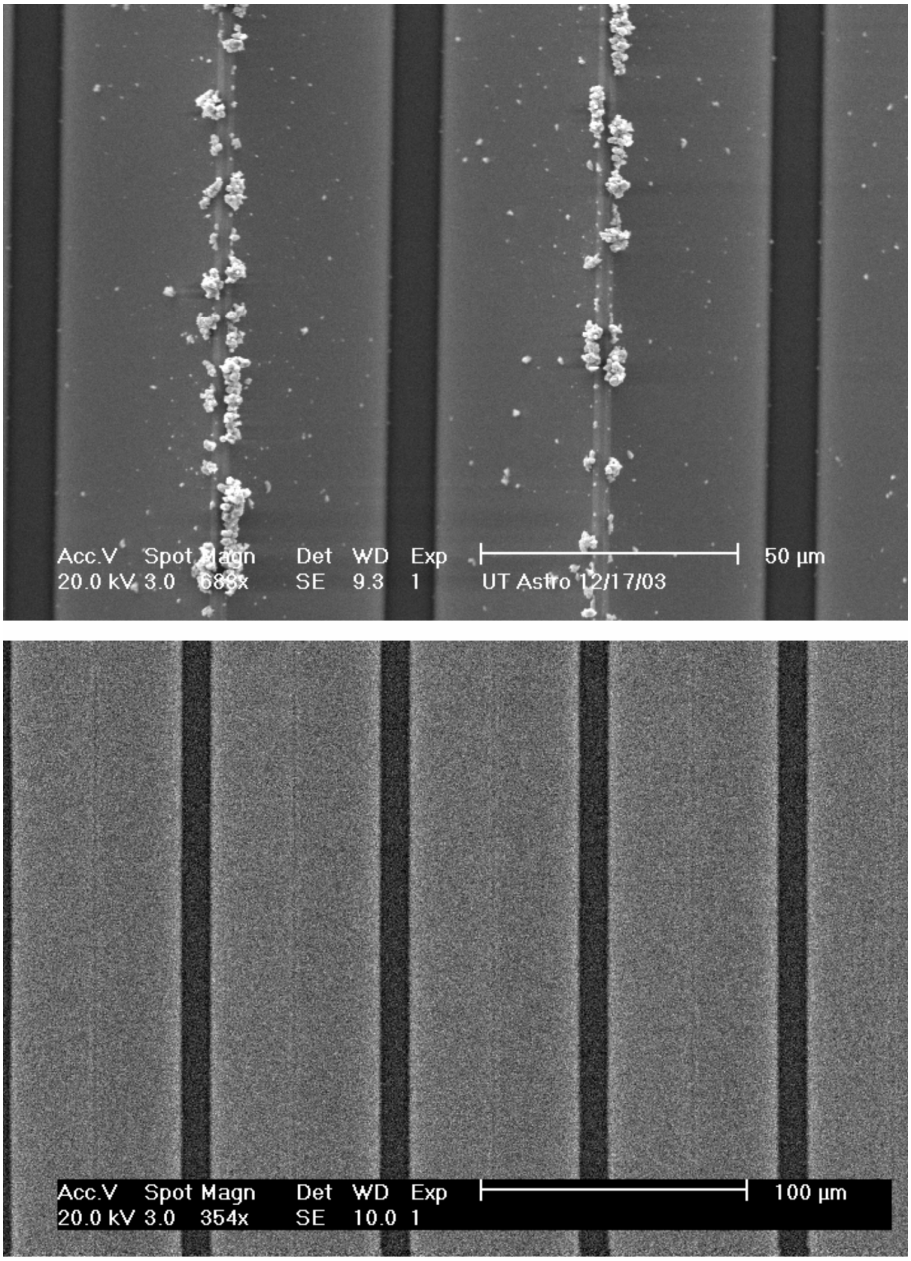

Figure 2.8. *Top:* SEM of a grating etched on a thin wafer showing thin strips of residual passivation layer. A byproduct of KOH etching, $Si(OH)_4$, polymerizes and creates white grains. *Bottom:* The same grating after hot phosphoric acid etch. Both nitride strips and etch residue are removed by the phosphoric acid.

Phosphoric acid etches silicon nitride at 10-20 Å/min (van Gelder and Hauser 1967) at 150°C but the exact rate depends strongly on the temperature. The etch rate of silicon under these conditions is less than 1-2 Å/min. The stripping of the remaining nitride layer is accompanied by the removal of polymer formations of $Si(OH)_4$ which are a by-product of KOH etch and tend to settle near the groove top (see Figure 2.8). If left intact, these formations would become a source of scattered light. Even more important than for decreasing scattered light (in immersion, this material, in fact, does not contribute to scattered light), the residue removal is vital for a uniform and unbroken deposition of a reflective coating (see the second paragraph below and Figure 2.9, *top, middle*).

We contracted outside vendors to perform the post-processing cutting steps. The grating, which is etched into one side of a thick silicon substrate, is shaped into a prism with the grating covering the hypotenuse side and the entrance side tilted by a small amount from the groove surface (usually ~1° but the exact tilt depends on the grating and instrument specifications) thereby introducing a displacement between incident light and diffracted light thereby removing unwanted reflections in the spectra (step 12 in Figure 2.4). We also introduced a wedge shaped bottom in G1 in order to further minimize and redirect secondary reflections and stray light resulting from diffracted light hitting the bottom surface of the prism in an attempt to tune our grating for performance as an immersion grating (see Appendix A).

Anti-reflection coating on the entrance face was done by II-VI Inc. for two out of three gratings evaluated in this paper (G0 and G1). The coating was optimized for transmission in the 1.1-5 μm band because of the requirements of ImGES for which grating G1 was designed. The quality of both coatings was very good and the maximum reflectivity measured in 1.1-5 μm band was 10% at 1.5 μm. The reflectance of the AR

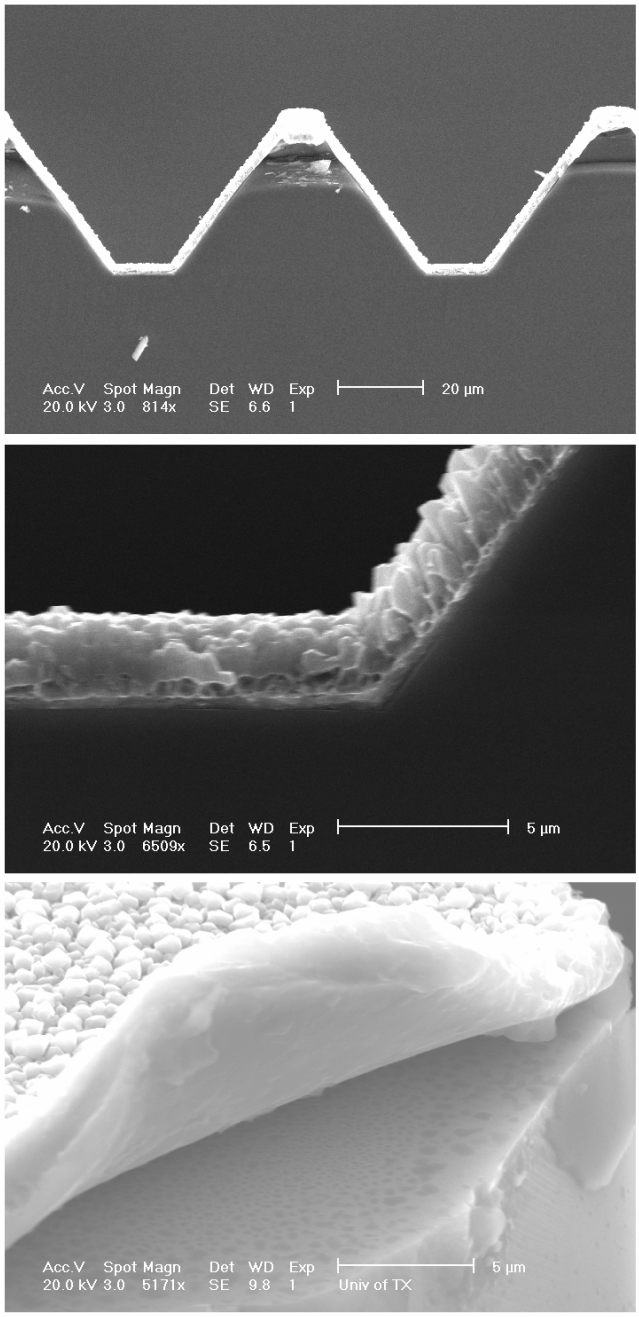

Figure 2.9. SEM of an aluminized grating showing several grooves (*top*) and a corner detail of one groove (*middle*). The thickness of the aluminum reflective coating is approximately 2 µm. *Bottom:* The aluminum layer starts to peel after many thermal cycles (immersing the whole coated wafer in liquid nitrogen and warming it to room temperature). A grating in an instrument would never be exposed to such rapid temperature changes.

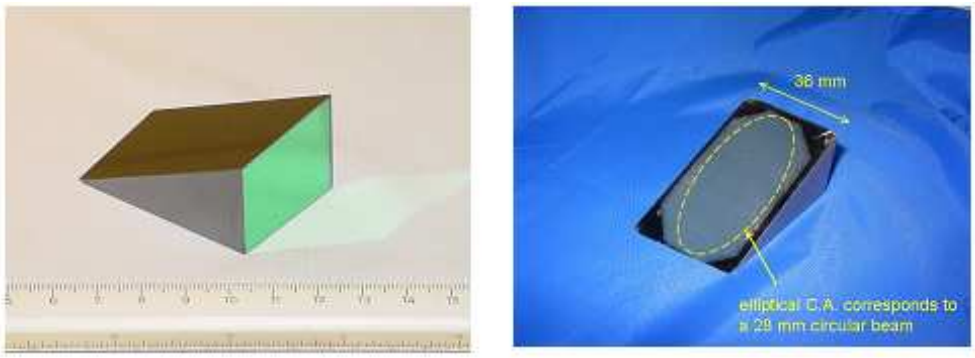

Figure 2.10. *Left:* Grating G1 – shaped to its finished prism form, with the entrance face coated with an anti-reflection coating optimized for 1.2-5 μm. *Right:* Grating G1 after a reflection coating (aluminum) was deposited on the grating surface. The ellipse drawn on the grating illustrates the boundary of the 23 mm collimated beam projected on the grated surface.

coating between 1.6 and 5 μm was 3% or less. The reflective coating on the groove surfaces was done in-house and consists of a layer of aluminum approximately 2 μm thick which was deposited on the groove surfaces using a sputterer (see Figure 2.10 showing photographs of the completed grating G1).

2.3 MEASURED PERFORMANCE OF COMPLETED GRATINGS

We have used thin silicon wafers to test all aspects of our in-house processing, to tune all steps, and to test our equipment. Once we were confident in our ability to process thin silicon substrates, we moved on to thicker substrates adjusting the parameters in our processing steps to accommodate larger silicon mass and area. Once a grating is completed, we visually inspect it for large area defects (any visible damage on the surface, scratches, breaks in the groove pattern) and then conduct optical tests which can provide further clues about our process. Optical tests are designed to provide us with information about wave front shape and error, point-spread function and efficiency of our gratings. Analyzing the errors using optical testing of the etched gratings gives us valuable clues about how we should improve the process and what area needs improvement the most.

2.3.1 Imaging/Visual Confirmation of Our Process

SEM is a useful tool for verifying the groove shape, size and orientation (see Figure 2.5) as well as for estimating the number and type of surface defects. We have also used it to estimate etch rates by measuring the amount of undercutting (see Figure 2.6), to test our nitride removal process using hot phosphoric acid (see Figure 2.8), and to test the metallization of groove surfaces (see Figure 2.9). The use of SEM is limited to

wafers especially when we observe groove profiles as the vertical clearance inside the SEM chamber is only a few millimeters. Large defects in etched substrates can also be observed with a naked eye or with a microscope.

2.3.2 Efficiency

Our method for measuring grating efficiency utilizes monochromatic spectra taken at several wavelengths. Monochromatic light is diffracted into discrete orders given by the grating equation (Eq. 2.2). The intensity distribution in diffracted orders for high order echelle gratings is given by the blaze function (e.g. Born & Wolf 1997):

$$\frac{I(\beta)}{I_0} = \left(\frac{\sin\left[\frac{\pi s}{\lambda}(\sin\beta - \sin\alpha)\right]}{\left[\frac{\pi s}{\lambda}(\sin\beta - \sin\alpha)\right]} \right)^2 \tag{2.9}$$

where *s* is the effective groove width. Because the three gratings analyzed here are in high orders, their order intensity distributions will be determined by Eq. 2.9. For gratings operating in the scalar limit such as G0, G1 and G3, we can correct the measured efficiency at an arbitrary wavelength to the efficiency at the blaze wavelength. In this paper, we measure the relative grating efficiency which is equal to the intensity of light diffracted by the grating divided by the intensity of light incident on the grating surface but with the effects of silicon reflectivity/transmissivity and groove tops removed. In doing so, we are only testing the quality of groove surfaces deconvolved from the material properties.

Our test setup consists of two bench spectrographs with a layout identical to that of a Twyman-Green interferometer (see Figure 2.11). The first spectrograph uses two

visible light HeNe lasers (543.5 nm and 632.8 nm) and the second uses an IR HeNe laser (1.523 μm) as a light source. In both setups, light from the lasers is collimated using Oriel collimators (the IR collimator does not contain a spatial filter but the optical one does). The beam diameter was changed to accommodate different grating sizes and beam splitter clearance. For the visible light setup, the beam size is 15 mm for G0 and 25 mm for G1 and G3. For the IR setup, the beam size is 10 mm for all gratings. Beam splitters in both setups direct light into two arms. One arm always contains a reference mirror and the other the grating being tested. With the reference mirror image always present in the recorded spectra, we can measure relative efficiencies of our gratings by comparing intensities of light in diffracted orders to the intensity of the reference mirror image. Light from both spectrograph arms is focused onto a CCD or an IR camera and recorded as a monochromatic spectrum. The CCD contains a 1024×1024 array of 13 μm square pixels. The IR camera is an Indigo AlphaNIR camera with an InGaAs array consisting of 320×256 pixels (30 μm square pixels) sensitive in the 0.9-1.7 μm bandpass. The CCD is cooled with a fan and the IR camera is cooled with a Peltier cooler. They both operate at ambient temperature (no cryogenic cooling is required). Camera lenses in both setups are interchangeable. We use either a f=125 mm (for IR setup) or f=200 mm (for visible setup) lens to record a spectrum consisting of 2-10 orders on the detector or a f=838 mm lens to resolve the diffraction spot and analyze the grating point-spread function (PSF). When recording a monochromatic spectrum, we obtain 20-50 exposures with the CCD or IR camera as well as dark frames which are used to remove features intrinsic to the detector. To extract a 1D spectrum, we sum over 10-20 rows or columns of the image centered on the brightest order in the cross-dispersion direction and subtract the nearby area of the same size. Monochromatic spectra are shown in Figures 2.12 and 2.13 for

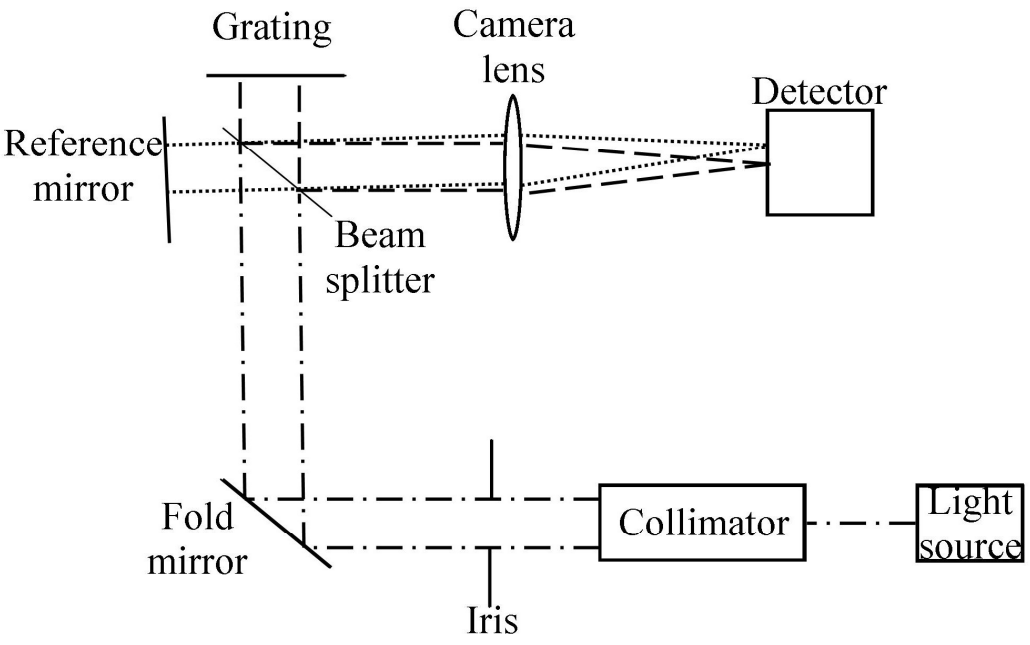

Figure 2.11. Bench test setup.

green and infrared light. At 543.5 nm, gratings are used as front-surface devices. At 1.523 μm, gratings are used as immersion echelles.

The results of our relative efficiency determinations for all three wavelengths are summarized in Table 2.2. Our method for measuring the relative efficiency of a grating using monochromatic light consists of adding the relative efficiencies of several observed orders closest to the blaze order and normalizing it to the maximum efficiency, η_0:

$$\text{Relative efficiency} = \frac{\sum_{\text{observed orders}} \eta_i}{\eta_0} \tag{2.10}$$

η_0 is the maximum relative efficiency that can be measured in the observed orders which accounts for geometrical losses due to the presence of groove tops, efficiency losses due to the finite number of orders observed, and, if necessary, the difference between the reflectivity of the reference mirror and the grating.

There are several steps involved in correcting raw measured efficiencies. The first step is integrating light in all orders that appear on the detector and comparing it to the output from a silicon reference mirror (for uncoated gratings) or a gold reference mirror (for coated gratings) to get $\eta_{measured}$. The effect of silicon reflectivity is thus removed from the measurement of uncoated gratings and the measured efficiencies reflect only the performance of the grating itself. The second column in Table 2.2 contains $\eta_{measured}$ corrected for the beam splitter transmission in two arms ("arm coefficient"). The arm coefficient is the consequence of the displacement of the beam coming from the reference mirror with respect to the beam coming from the grating. The beams from two arms hit the beam splitter at slightly different angles so the reflectivity/transmissivity of the beam splitter is slightly different for the two arms. The

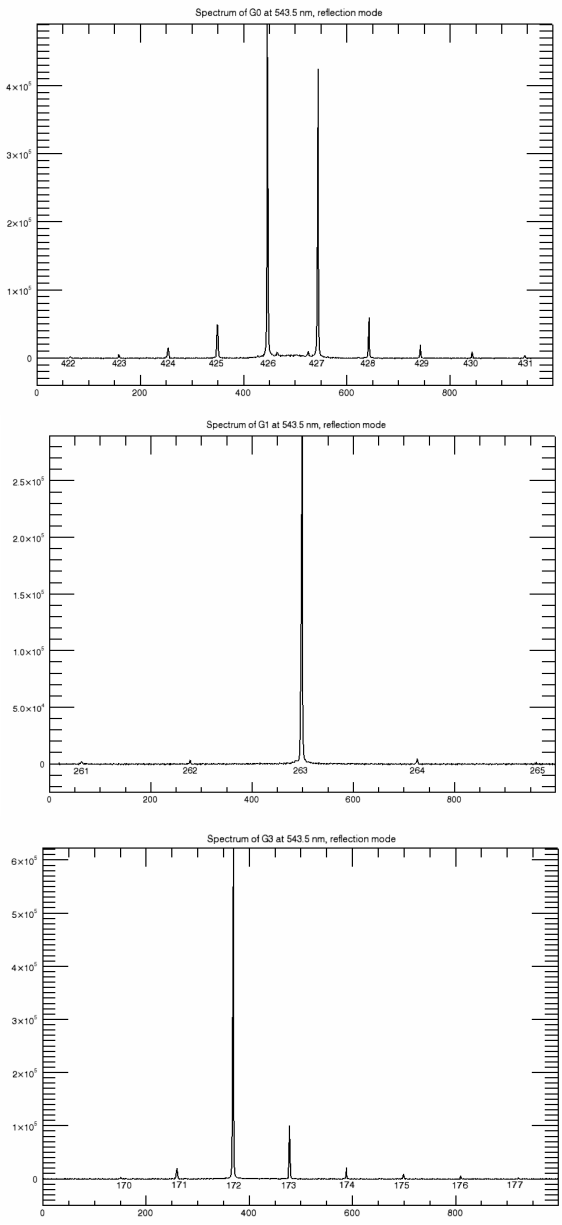

Figure 2.12. Front-surface, monochromatic spectra of G0 (top), G1 (middle), and G3 (bottom) at 543.5 nm. The lower scale on the x-axis gives position along the spectrum in pixels while the upper scale identifies the order number of the peaks. The y-axis scale is in counts integrated over several rows in the cross-dispersion direction. The gratings show a steady improvement in eliminating scattered light and ghosts going from the earliest work (G0) to our most recent effort (G3).

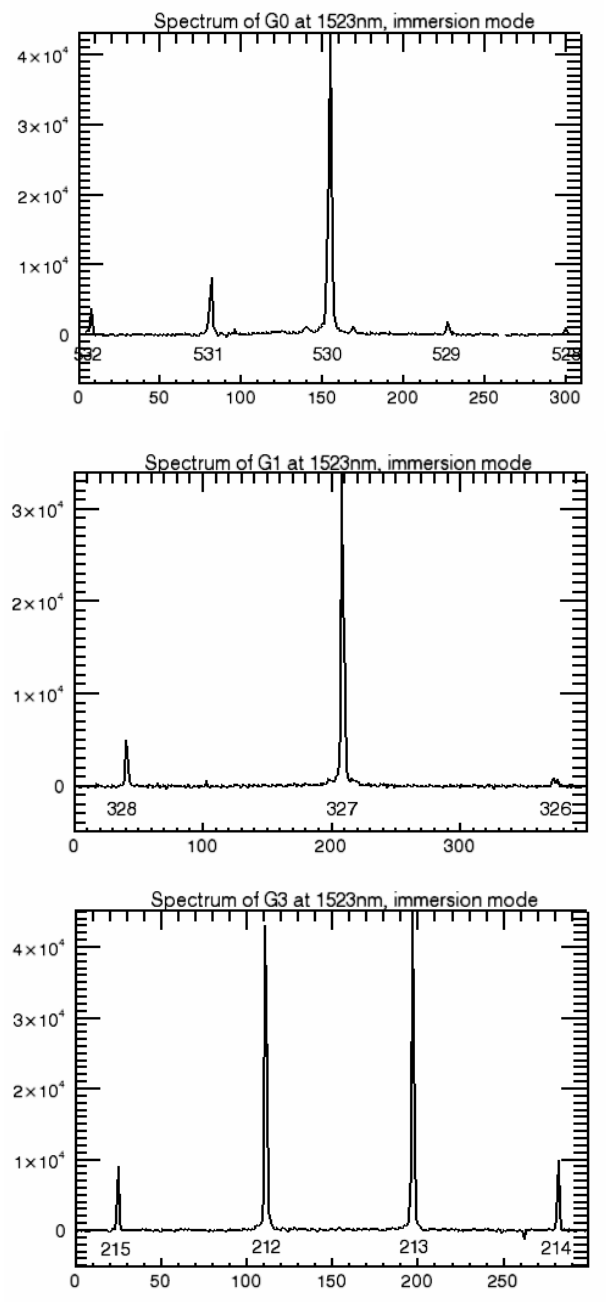

Figure 2.13. Monochromatic spectra of G0 (top), G1 (middle), and G3 (bottom) in immersion at 1.523 μm. The lower scale on the x-axis gives position along the spectrum in pixels while the upper scale identifies the order number of the peaks. The y-axis scale is in counts integrated over several rows in the cross-dispersion direction. The gratings show a steady improvement in eliminating scattered light and ghosts going from the earliest work (G0) to our most recent effort (G3).

arm coefficient varies for all three wavelengths and its value was determined experimentally to be 1.038-1.100. Data recorded with the IR camera is also corrected for the apparent non-linear behavior of the camera by dividing by 1.3 (also determined empirically for a set ratio of reference mirror signal/grating signal).

Two factors determine η_0 in most cases. The first one is the light loss due to the presence of groove tops which direct light out of the range of our observations. This factor is only taken into consideration for visible wavelengths where the gratings are used as front-surface devices. When used in immersion, groove tops are hidden and therefore do not play a role in the diffraction of incident light (correction factor is 1). The second factor is due to the mismatch between the blaze function minima and the interference maxima effectively causing light loss into adjacent orders (Schroeder & Hilliard 1980). This factor was determined by calculating positions and intensities of all propagating orders and dividing the sum of intensities for orders we were able to observe by the sum of all intensities in propagating orders. The total correction factor is then equal to the product of two correction factors and is given for each case in the third column of Table 2.2. Relative efficiency is given in column 4 in Table 2.2 and is the ratio of measured to maximum efficiency. Calculation of peak blaze efficiencies (given in column 5 in Table 2.2 for reference) is based on the method outlined by Schroeder and Hilliard (1980). The device throughput can be calculated by multiplying columns 4 and 5. Our measurements indicate that our gratings have been steadily improving in quality and we can now achieve throughput efficiencies of 70% or better on the blaze for the shortest wavelength in our measurements. G3 meets our requirement for an echelle grating with relative efficiency >80% at 2 μm in immersion. All three gratings are comparable and in most cases even better than commercially available echelles.

Table 2.2. Measured relative efficiencies at three different wavelengths.

Grating	$\eta_{measured}$	η_0	η/η_0	**Theoretical blaze efficiency**
		λ=543.5 nm		
G0	63%	91%	69%	86%
G1	63%	88%	72%	86%
G3	78%	91%	86%	86%
		λ=632.8 nm		
G0	62%	91%	68%	87%
G1	64%	88%	72%	86%
G3	78%	90%	87%	87%
		λ=1523 nm		
G0	48%	95%	62%	92%
G1	68%	96%	71%	97%
G3	80%	93%	86%	93%

2.3.3 Resolving power and point spread function

Visible wavelength interference analysis of the grating was done with an optical (Zygo) interferometer. It was a very valuable tool in testing the wave front shape and predicting the point spread function of our gratings. The limitation of the data taken with the Zygo interferometer is that the light source for the Zygo is a HeNe laser at 632.8 nm and therefore we had to perform tests of the gratings in reflection and then predict its performance in immersion at 1.523 μm. In Figure 2.14, we show the point-spread function (PSF) of G1 directly measured in immersion and the PSF of G1 predicted from the Zygo measurements for G1 used in immersion. The Zygo gives an accurate picture of what the grating performance will be in immersion and we will rely on it in the future to estimate the PSF of our gratings before we cut and shape them into prisms. We measured the infrared PSF of all three gratings with our modified bench setup. The beam size is limited by the size of the beam splitter to 10 mm in diameter. The short focal length lens was replaced with an f = 838 mm lens which produced diffraction limited images. The diameter of the Airy disk is $1.22\lambda f/(D_{beam}\Delta x_{pixel})$=5.2 pixels where Δx_{pixel}=30 μm is the pixel size for the IR camera. Images like the one shown for G1 PSF were dark subtracted. The first step in analyzing the images was to fit a 2D Gaussian function in order to measure the width of the diffraction spot. The results of this step are summarized in Table 2.3. Predicted resolving power, $R_{predicted}$, is calculated using Eq. 2.1. Demonstrated resolving power, $R_{demonstrated}$ was calculated using the following formula for angular dispersion in the Littrow mode:

$$\frac{d\beta}{d\lambda} = \frac{2n\tan\delta}{\lambda} \tag{2.11}$$

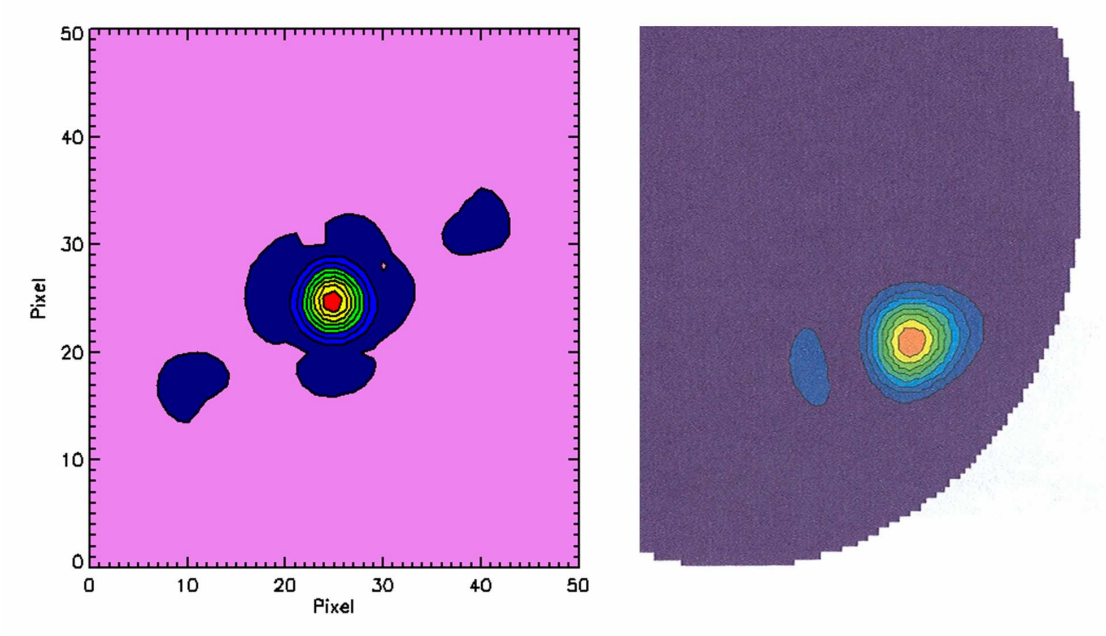

Figure 2.14. Comparison of PSFs measured directly at 1.523 μm (*left*) and predicted from the wave front measured by Zygo (*right*).

and corrected for pixel sampling. From this equation, we can calculate

$$\Delta\lambda = \frac{\lambda}{2nf\ \tan\delta}\Delta x \tag{2.12}$$

where Δx=30 μm×FWHM$_x$ (in pixels) and $R_{demonstrated}=\lambda/\Delta\lambda$. We demonstrated measured resolving power of as much as 75,000 at 1.523 μm using our immersion gratings.

The next step is to obtain 1D PSFs shown in Figure 2.15 by summing over 10 pixels in the cross dispersion direction around the peak of the diffraction spot in order to determine Strehl ratios of G0, G1 and G3. The Strehl ratio is defined as the peak value of intensity (normalized to the total power in the PSF) for an aberrated image relative to its value for an unaberrated image. Optical systems with a Strehl ratio greater than 0.8 are usually considered diffraction limited. A system with the Strehl of >0.8 would have an RMS wave front error of $<\lambda/14$. We calculated the area under the 1D spectral PSF for each grating and normalized the PSF by the ratio of that area to the area under the mirror PSF which is in this case our unaberrated PSF. The peak value of the normalized grating PSF is the Strehl ratio. The Strehl ratios for gratings G0, G1, and G3 are shown in Table 2.3. The last two columns contain values of Strehl ratios measured directly from the infrared spectra in immersion and calculated from the wavefront errors determined from the Zygo interferometers shown in Figure 2.16. They are in agreement and the biggest discrepancy was seen in G0, where the measured Strehl was 0.71 and the Zygo determination of the Strehl was 0.82 but it is not too surprising because the quality of G0 varies across the surface and it depends strongly on which part of the grating surface is used.

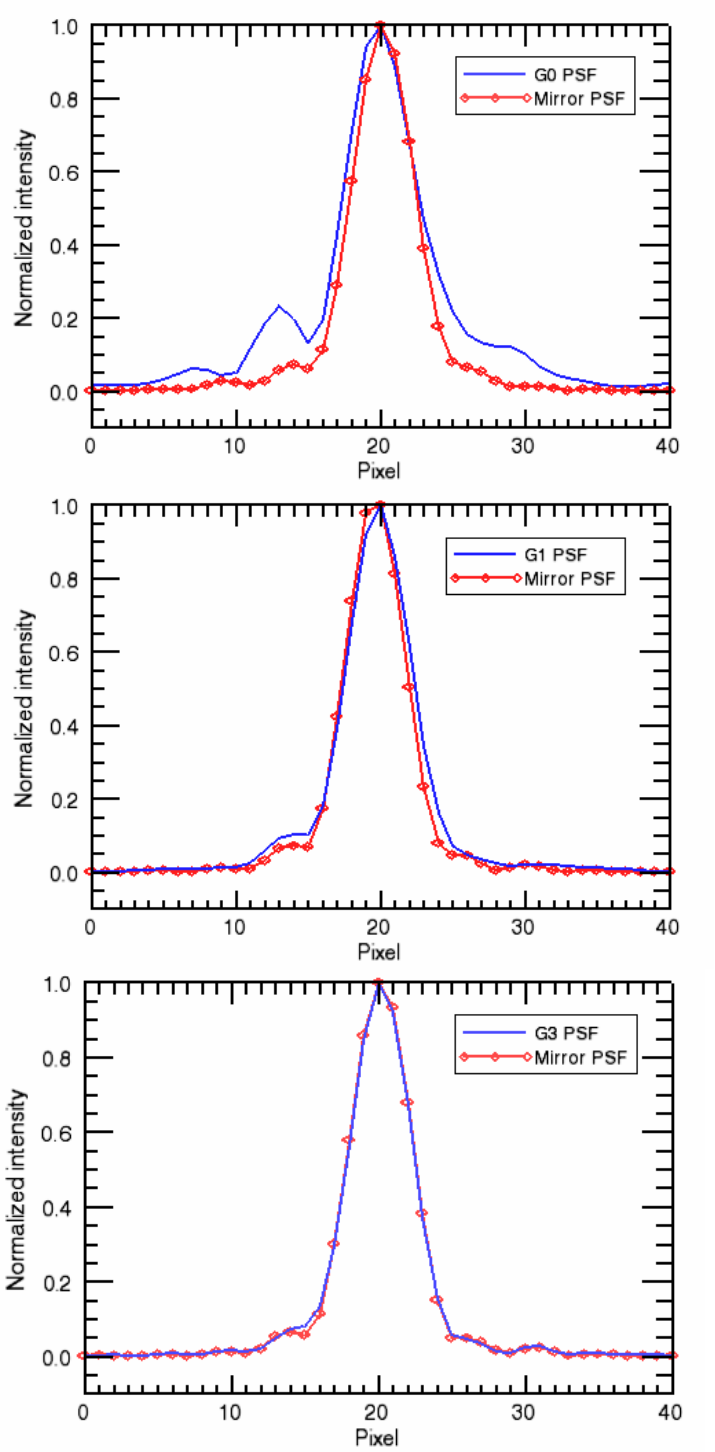

Figure 2.15. Spectral PSFs of G0 (*top*), G1 (*middle*), and G3 (*bottom*) compared to the PSF of a mirror.

We conclude that the performance of G1 and G3 is diffraction limited at 1.523 μm when used as immersion gratings and that G0 can attain diffraction limited performance in some areas of the grating at 2 μm. The agreement between the front surface tests using the Zygo interferometer and direct immersion tests is another confirmation of our method that uses front surface measurements, both spectroscopic and interferometric, to test and predict the performance of echelles in immersion.

2.3.4 Wave front aberrations and grating defects

Errors in the groove shape and spacing and groove surface roughness are factors that degrade the performance of diffraction gratings by lowering their efficiency and causing unwanted features in the observed spectra. These errors and defects manifest themselves as ghosts, satellites, grass, and diffuse scatter (Palmer et al. 1975). We discuss our observations of these errors as well as ways to improve the performance of future gratings.

2.3.4.1 Grass

Random errors in groove positions cause a small number of grooves to be out of phase with the rest of the grooves so that the condition for constructive interference is destroyed for these grooves. They are seen as "grass", i.e. scatter between orders in a monochromatic spectrum. We have previously observed grass in the spectrum of G0 and concluded that the intensity distribution of light in the grass matches that of the blaze function for a single groove (Marsh et al. 2003, Chapter 3). In this paper, we estimated the fraction of light in grass, η_{grass} (we use η to denote the fraction of light in the grass because the value is measured relative to a reference mirror and corrected for the

Table 2.3. Width of PSF and measured resolving power.

Grating	**FWHM$_x$**	**FWHM$_y$**	$R_{demonstrated}$	$R_{predicted}$	**Strehl ratio**	
					from IR PSF	**from Zygo**
Mirror	4.78	4.90				
G0	5.99	5.11	45,500	64,100	0.71	0.82
G1	5.10	4.79	75,400	90,500	0.91	0.90
G3	4.74	4.90	26,000	28,900	0.99	1.0

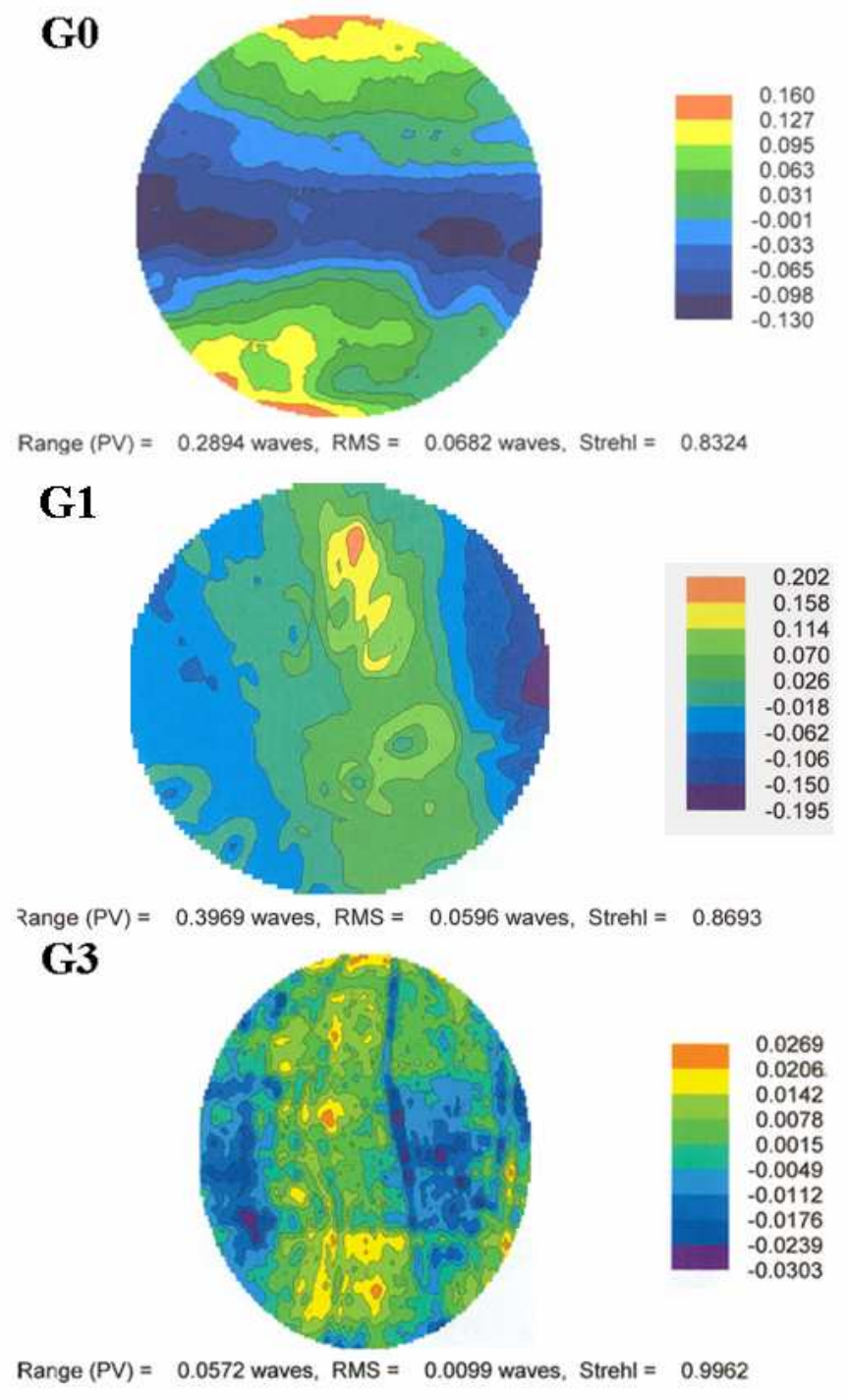

Figure 2.16. Interferograms G0, G1, and G3 taken with the Zygo interferometer. All three gratings exhibit diffraction limited performance on the scales shown.

presence of groove tops rather than uncorrected intensity), from our spectra by integrating over 10-20 rows of the spectrum images to obtain a 1D spectrum (the same method we used to measure efficiencies), and then subtracting out previously determined efficiency $\eta_{measured}$ in observed orders as well as any observed ghosts. The angular range of integration in the cross dispersion direction was only 0.07° so the diffuse scattered light, while it may raise the value of light intensity scattered in grass, should not contribute to it significantly. Measured values for scattered light in grass are given in Table 2.4. The intensity of light in grass is given by (Palmer et al. 1975):

$$\frac{\eta_{grass}}{\eta_0} = \left(\frac{2\pi}{\lambda} 2\varepsilon_{spacing} \sin\delta \right)^2 \tag{2.13}$$

Eq. 2.13 is an approximation derived from Eq. 2.4 for small values of $\varepsilon_{spacing}$. Using the above equation, we estimated $\varepsilon_{spacing}$, that is, the portion of the spacing error we can assign to random displacements of groove positions, using the measured values of η_{grass}. η_0 is given in Table 2.2. This is the error that represents the accuracy with which we can position lines in the passivation layer and subsequently etch grooves. We immediately notice that the random spacing errors, $\varepsilon_{spacing}$, derived from the observed grass intensity are both very small and close to the same value for all three gratings. This result implies that we have good control over the pattern transfer process and good repeatability, even for thick silicon substrates. The total measured errors, ε_{phase}, derived from the Zygo interferograms, are larger than the spacing errors and differ more strongly from grating to grating. As we will show, the larger values of ε_{phase} derived for G0 and G1 result from repetitive errors which produce ghosts rather than grass (see Section 2.3.4.3). Also, G0 has a somewhat larger RMS error which is most likely the result of using a SiO_2

Table 2.4. Scattered light due to random errors in groove positions.

Grating	$\frac{\eta_{grass}}{\eta_0}$	$\varepsilon_{spacing}$	ε_{phase}	ε_{phase} **from Zygo interferograms**[a]
G0	7.9%	17 nm	14 nm	43.2 nm
G1	4.6%	12 nm	11 nm	37.7 nm
G3	1.9%	13 nm	6.9 nm	6.3 nm

[a]Even though we recorded interferograms of the whole grating surface (which for G1 and G3 was the whole etched area of the silicon disk), we quote here the RMS front error estimated from areas shaped and sized to match the area used in the spectroscopic measurements for which $\varepsilon_{spacing}$ was determined (see Figure 2.16).

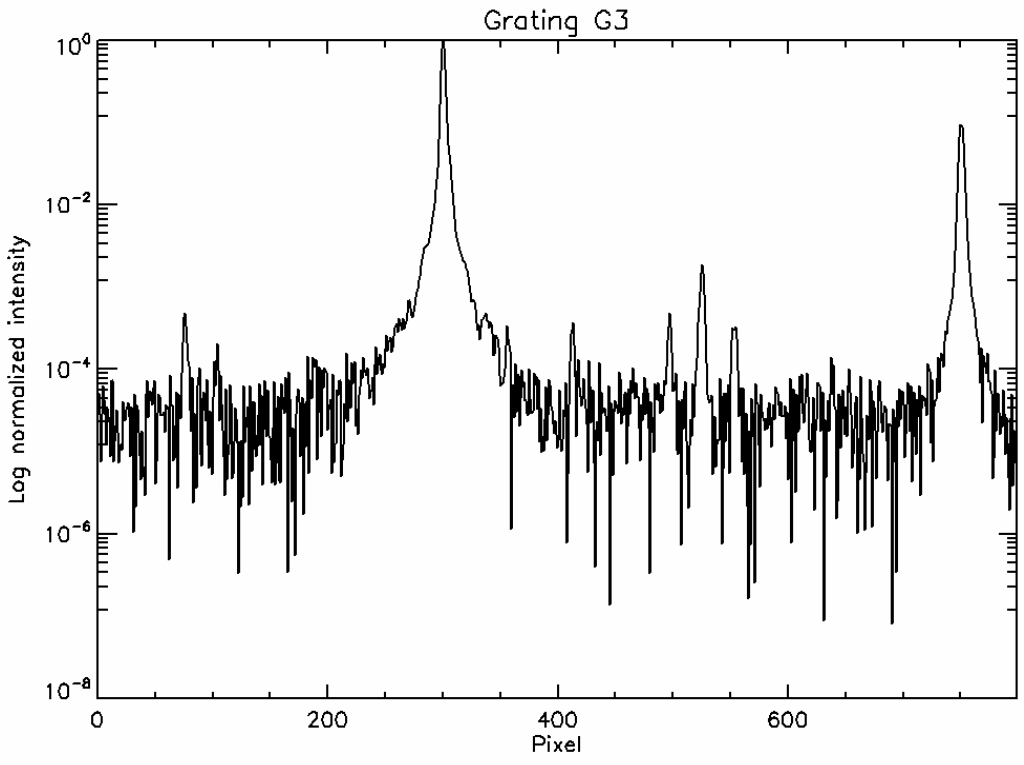

Figure 2.17. By taking several thousand exposures of the monochromatic spectrum of G3 at 543.5 nm, we were able to observe the grass in detail.

passivation layer. SiO_2 is subject to destruction when etching in a water-based KOH solution therefore needs to be thicker than the nitride passivation layers used in G1 and G3. Si_3N_4 by contrast is not attacked by KOH solutions allowing us to use much thinner (up to 10 times) layers of it.

The scattered light in grass of our most recent grating G3 (see Figure 2.17) is comparable to a commercially produced R2 echelle used in the 2d coudé spectrograph on the 2.7 m telescope at the McDonald Observatory (Tull et al. 1995).

2.3.4.2 Diffuse scattered light

Any deviation in the height of a groove surface from a perfectly smooth surface up to scale sizes of the order of λ is called groove microroughness. Small scale roughness of the groove surfaces causes incident light to be scattered in random directions. In extreme cases where the amount of scattered light is large, we can observe a halo around the center of the spectrum. More typically, the large angular scale of the diffuse scattered light makes it very difficult to perform direct measurements. Instead, we have to use indirect techniques involving profilometry and atomic force microscope (AFM) to measure the surface roughness ($\varepsilon_{roughness}$). We have done this for one of our grisms, G2 (see Chapter 4), but due to height constraints in an AFM (vertical travel <4 μm), we are unable to measure any of the gratings discussed in this chapter. There is a wealth of information published about the temporal evolution of roughness of (100) surfaces (e.g. Palik et al. 1991, Findler et al. 1992), but very little is available about (111) surfaces. Sato et al. (1998) discuss the roughness of (111) surfaces but only for aqueous KOH solutions without the addition of isopropanol and ultrasonic energy which we know improve the surface finish of etched (100) surfaces (Baum and Schiffrin 1997).

Total integrated scattering is given approximately by (Bennett & Mattsson 1999):

Table 2.5. Estimate of microroughness from the AFM data and calculated total diffuse scattered light at three key wavelengths.

Grating	$\varepsilon_{roughness}$	$\frac{I_{diffuse}}{I_0}$ **at 632.8 nm**	$\frac{I_{diffuse}}{I_0}$ **at 1.523 μm**[a]	$\frac{I_{diffuse}}{I_0}$ **at 3.5 μm**[a]
G2	1.7 nm	0.1%	0.2%	0.04%

[a]Estimates are given for grating used in immersion at 1.523 μm and 3.5 μm. The corresponding internal wavelengths are 441 nm and 1023 nm.

$$\frac{I_{diffuse}}{I_0} = \left(\frac{2\pi n}{\lambda} 2\varepsilon_{roughness} \right)^2 \tag{2.14}$$

where $\varepsilon_{roughness}$ is the RMS surface roughness as measured by the AFM. We measured average $\varepsilon_{roughness}$ of 1.7 nm on a 2 μm×2 μm area of groove surface for G2. The summary of predicted $I_{diffuse}$ for G2 using Eq. 2.14 for several wavelengths is given in Table 2.5. These values are lower limits for G0, G1, and G3 for diffuse light due to microroughness.

Surface microroughness can be traced to several factors: imperfections in silicon crystal (e.g. when the etch encounters an oxygen atom), H_2 bubbles that linger on the surface after the reaction took place, impurities in the KOH solution itself (Hein et al. 1997), temperature variations in the etch solution or during the etch, etc. In our etching method, we have used both ultrasonic agitation and isopropanol to promote the H_2 bubble detachment. Silicon material we procure is of very high purity with low oxygen concentration even though it is unclear how much impurities actually affect immersion grating manufacture (Kuzmenko & Ciarlo 1998). The surface is treated with hot phosphoric acid after the KOH etch to remove residual polymers. This combination of materials and etch process variables resulted in an excellent groove surface quality even at the shortest wavelengths at which silicon transmits IR radiation.

There are other sources of diffuse scattered light such as large groove defects (breaks in grooves, pyramid formations due to impurities in the crystal) that we are unable to account for in the predicted value from the AFM roughness measurement. We have observed these “macrodefects” using both visible light microscopes and SEM.

2.3.4.3 Ghosts

When grooves are displaced from the perfect spacing σ with a periodic variation, they result in the appearance of secondary images or ghosts. When ghosts are near the parent line, they are called Rowland ghosts. We have observed Rowland ghosts in G0 which are the result of errors in the ruled mask used to pattern the substrate (Keller et al. 2000, Marsh et al. 2003). The period and amplitude of the periodic groove spacing error are P=780 μm and A=13.5 nm. In an attempt to eliminate ghosts, we acquired standard photolithographic masks which do not suffer from stitching and periodic errors. The use of the new masks eliminated the periodic error in the dispersion direction in G1 and G3. We still observed ghosts in both gratings, however, but these ghosts were displaced from the dispersion direction by an angle of 30° (see Figure 2.14) and they matched very well the directionality of the periodic wave front error easily spotted in the Zygo image of G1 (see Figure 2.16, *middle*). We decided to apply the analysis appropriate for Rowland ghosts and compare the results to the Zygo data in order to determine whether the periodic pattern really is the source of ghosts in these two gratings.

The relationship between the period of the spacing error and the distance of the Rowland ghost from the parent line in Littrow configuration is given by (Stroke 1967):

$$\Delta x_M = M \frac{\lambda f}{P \cos \delta} \tag{2.15}$$

where Δx_M is the distance between the parent line and M-th order Rowland ghost, M is the ghost order, P is the period of the spacing error. From Eq. 2.15, we deduce P=5.6 mm for G1 and P=0.61 mm for G3. In the wave front space observed in the Zygo interferogram, these distances will be shortened by cos δ in the cross-dispersion direction. The projected period in the wave front space is 5.1 mm which agrees well with the

measured 4.0 mm from the fringes seen in the interferogram of the whole surface of grating G1 (not shown here). The displacement of the ghosts from the dispersion direction and the size of the period indicates that the spacing error is not due to errors in the mask pattern but rather to problems during the contact printing of the mask lines onto the photoresist layer which we also confirmed visually by observing interference fringes while contacting the mask with the photoresist coated disks.

The relationship between the ghost intensity and the parent line intensity for the first pair of Rowland ghosts is given by (Stroke 1967):

$$\frac{I_{ghost}}{I_{line}} = \left(\frac{2\pi n}{\lambda} A \sin\delta \right)^2 \tag{2.16}$$

where A is the amplitude of the spacing error, and I_{ghost} and I_{line} are intensities of the ghost pair and the parent line respectively. We derive A=23 nm for G1 and A=9.2 nm for G3. From the interferogram of G1, we estimate A=28 nm/sin δ=31 nm in excellent agreement with the direct measurement. Integrated intensity in the ghosts is 8.2% and 0.5% of parent line intensities for G1 and G3 respectively at 1.523 μm in immersion.

Depending on the application the ghosts seen in our gratings may not represent a problem. Since they are displaced in the spatial direction as well as dispersion direction, we can define the extent of each order in a cross dispersed spectrograph so it doesn't include any contribution from ghost lines. Since the intensities scale as $1/\lambda^2$, their contribution will drop down to 1.5% level in the spectra of G1 (integrated in a pair of ghosts) around 3.5 μm for G1.

2.4 CONCLUSION

We have produced gratings appropriate for use in high resolution IR spectrographs (*R* from 20,000 to 100,000) as immersion devices from 1.1 to 5 μm. We have developed a method to reliably produce grating with any blaze angle and groove spacings from a few μm to a few hundred μm. We tested and used both kinds of passivation layers with silicon nitride yielding better results and more robust process than silicon oxide. Standard photolithography masks also produced results superior to glass ruled masks (diffraction limited performance in all cases and less scattered light indicating smaller number of surface defects and smoother groove surfaces). However, the simplicity and relatively inexpensive nature of transferring patterns to a silicon oxide layer should not be neglected in cases where diffraction limited performance is not a requirement at all wavelengths or the gratings are used at sufficiently long wavelengths. We thoroughly tested and evaluated these gratings as front surface as well as immersion devices and found the results to be consistent. Our testing method is now established and we are confident that, in the future, front surface tests can be used reliably to predict the performance of gratings in immersion.

Chapter 3.

Silicon Grisms and Immersion Gratings Produced by Anisotropic Etching: Testing and Analysis1

3.1 INTRODUCTION

Silicon diffraction gratings and grisms are very useful devices in the infrared because they can be compact and still maintain high resolving power. The wavelength of light in silicon is n = 3.4 times shorter than in air. When silicon diffraction gratings are used as immersion devices (light passing through the silicon prism before being diffracted by the grating and then leaving the prism through the same entrance face), the resolving power, $R=\lambda/\Delta\lambda$, of such a grating scales with n:

$$R = \frac{2nL\sin\delta}{\lambda} \tag{3.1}$$

where L is the length of the illuminated part of the grating and δ is the blaze angle. If we want to obtain the same resolving power as with a standard, front-surface grating, we can make the silicon grating 3.4 times shorter (and a collimated beam 3.4 times narrower) which will result in a significant reduction in the volume and therefore mass of our spectrometer. On large telescopes, where the overall spectrometer throughput at a given resolution is often driven by the mismatch between the slit size and the size of the seeing disk, an immersion grating spectrometer with the same size grating as a conventional instrument with the same R, can have a slit that is n times wider on the sky.

[1] Chapter 3 contains previously published work (Marsh et al. 2003).

For a grism, the resolution scales with n-1:

$$R = \frac{(n-1)L\sin\delta}{\lambda} \tag{3.2}$$

so a silicon grism would have a resolving power advantage ranging from a factor of ~1.8 (compared to KRS-5 with n ~ 2.4) to a factor of ~4.8 (compared to a glass grism with n ~ 1.5) with the same dimensions. As with the immersion gratings, we can use this advantage to either design a smaller grism or one with higher resolving power. In addition to the gain in resolving power we would realize from the use of silicon, the anistropic etching of the grating grooves offers two possible advantages. The first is that the etching process produces almost perfectly flat and smooth groove walls, properties that are especially important for efficiency in high orders where loss of power into nearby orders is a potential problem (Ershov et al. 2001). This high groove quality may not be achievable when ruling or machining other high-index materials. The second advantage is that etching allows us to produce much coarser grooves than can be made by ruling. This capability is important for long wavelength grisms and for devices to be used in high order or with small detectors. The high quality of the groove walls and the possibility of making coarse grooves can also make etched gratings preferable in some applications calling for conventional, front-surface gratings.

When producing infrared dispersive elements by anisotropic etching of silicon, the difference between a grism, an immersion grating and a front-surface grating is in the basic design (groove period and blaze angle) and in coatings (e.g. immersion grating will have an AR coating on its entrance face and a reflective coating on the grooves whereas a grism will have AR coatings on both the grooves and the entrance face). For purposes of

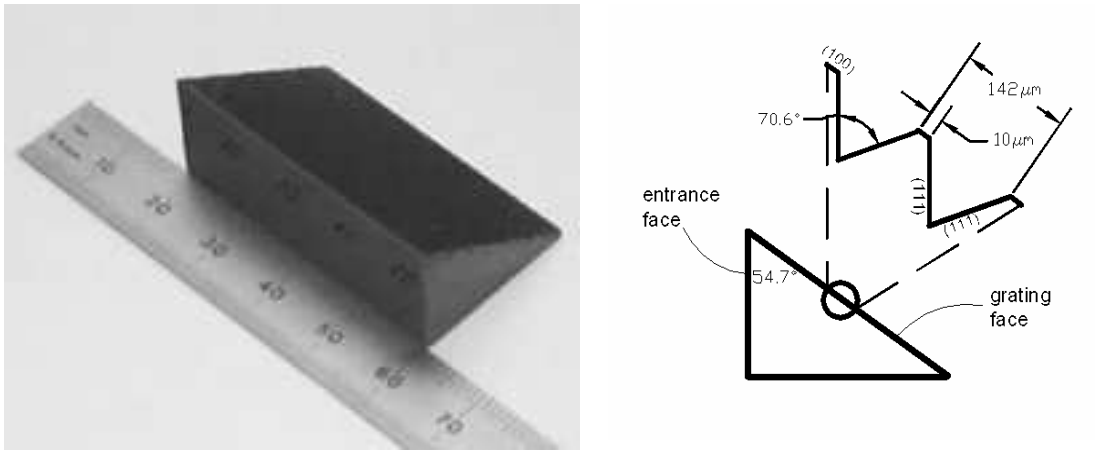

Figure 3.1. *Left pannel*: Sample prism used in this work for evaluation of our manufacturing process (Ershov et al. 2001). The prism opening angle is 54.7o. The entrance face (the side facing the ruler) is 17 mm × 42 mm and the hypotenuse face, which is 30 mm × 42 mm, has the grating etched into it. The grating pattern consists of symmetric grooves with a 142 μm period. *Right pannel*: Illustration showing the prism and the groove profile. Grooves are symmetric with an opening angle 70.5°. The groove period is 142 μm and the groove tops are 10 μm wide (artifacts of the process used to make the grating (Tsang & Wang 1975).

testing, however, a single (uncoated) grating can be used in all three modes. We have produced a prototype grating (Ershov et al. 2001) suitable for optical evaluation in all three modes. The grating was etched on an optically flat disk (15 mm thick, 70 mm in diameter). It has symmetric grooves spaced at 142 μm (see Figure 3.1, *right*). We contracted Janos Technologies Inc. to cut the disk into a prism and optically polish the entrance face. The prism (see Figure 3.1, *left*) has a 54.7° opening angle so the grating has a 54.7° blaze angle. The entrance face is 17 mm×42 mm and the grating surface etched into the hypotenuse of the prism is 30 mm×42 mm. The device was tested previously as a front-surface grating using two HeNe lasers (red at 632 nm and green at 543 nm; Ershov et al. 2001). We reported 70% efficiency at 632 nm, consistent with a 37 nm RMS error in groove spacing (the estimated RMS error in groove spacing from interferograms was 30 nm). The prism was left uncoated with the intention of testing the grating in immersion and transmission in the infrared at a later date.

3.2 TESTING SETUP

Silicon is opaque at optical wavelengths. Until now, we have only been able to test our gratings as front-surface devices and make indirect conclusions about their performance as immersion gratings and grisms (Keller et al. 2000, Ershov et al. 2001). However, we recently acquired an Alpha NIR camera (320×256 InGaAs array with 30 μm square pixels sensitive in the 0.9 - 1.7 μm region) from Indigo Systems which allowed us to expand our tests into the near-infrared. The thermoelectrically cooled detector operates after only a short cooldown time and focusing is made straightforward by a real-time image display.

Figure 3.2 illustrates the optical setups used to produce the spectra that we evaluated here. In the reflection (immersion) mode, the grating to be tested is positioned

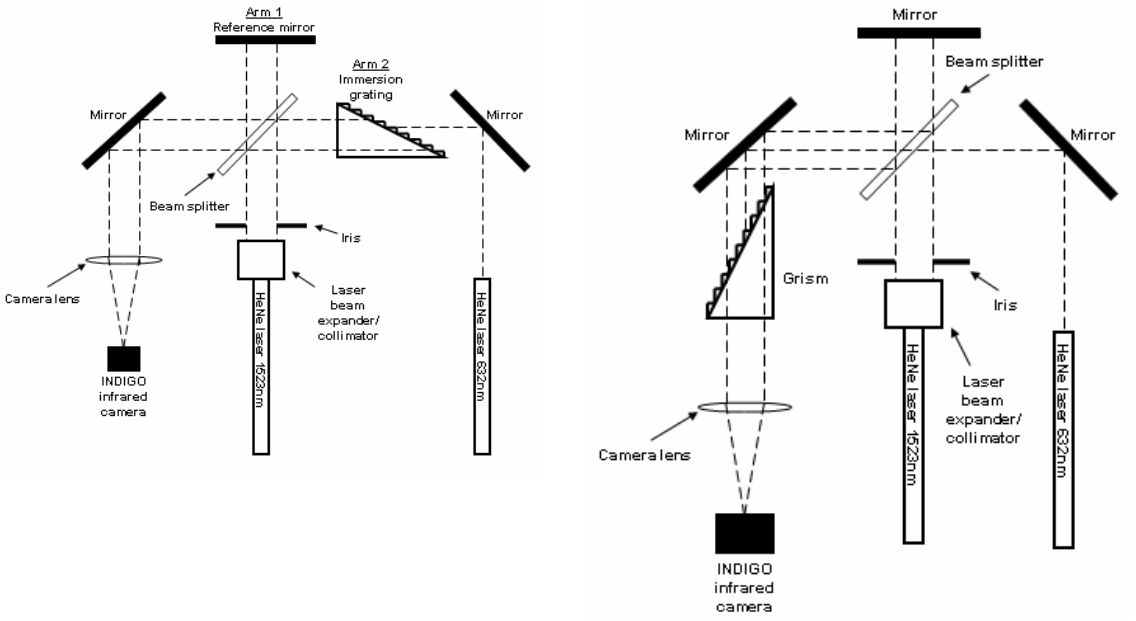

Figure 3.2. Test setup for immersion grating/front-surface grating (*left*) and grism (*right*). In both cases, the light source is an IR HeNe laser at 1.523 μm with a collimator producing a 10 mm beam. After passing through the beam splitter, the light is reflected by the reference mirror in Arm 1 or diffracted by an immersion or front-surface grating in Arm 2. In the grism mode, there is no Arm 2 and light passes through the grism on the way to the detector. The red HeNe laser was used for alignment.

in Arm 2 and a reference mirror in Arm 1. The reflection from the reference mirror and the spectrum from the grating are offset slightly in angle and both focused by a camera lens (usually of focal length 200 mm) onto the camera. In the transmission mode, there is no Arm 2 and the light reflected from the mirror in Arm 1 passes through the grism on the way to being focused by the camera lens onto the detector. In this mode, the reference signal is obtained in a separate exposure after removing the test sample from the beam.

We use a HeNe laser at 1.523 μm as a light source for our spectrometer setup and a red HeNe laser at 632 nm for alignment. First, we aligned the IR laser and all the optical elements in the light path to make the beam parallel to the optical bench surface and centered on the detector. Then we aligned the red HeNe laser beam to coincide with the optical discharge from the IR laser and made sure it was still parallel to the surface. We had to observe the discharge from the IR laser and position the red beam in the center of the collimated discharge representing the IR beam by eye since the IR camera cannot detect light at 632 nm. When test pieces are inserted into the setup, we insure that the gratings operate in Littrow by orienting them so that the principal order at 632 nm returns to the entrance aperture of the red HeNe laser. We are now able to use reflected red light for alignment in the reflection mode or diffracted red light in the immersion/transmission mode. Because the entrance face is cut at a small offset (~1^{o}) from the direction parallel to the grooves in order to redirect reflected light, we had to rotate the grating through a small angle to ensure the grating was in Littrow when operating in the reflection mode. This extra step was avoided in the grism mode by turning the grism so that light hits the grating side first allowing us to align diffracted red light from the grism with the incoming red beam.

Science images are stored on the host computer in datasets which include raw data as well as three arrays containing non-uniformity corrections and a bad pixel table. Images were corrected (gain, bias and bad pixel corrections) using the algorithm supplied by Indigo Systems and then saved as 2D FITS images for further analysis with IDL. Exposures were also taken with the laser turned off in order to remove background intrinsic to the camera. The first step in analysis was to subtract this background from all 2D images. The dispersion direction is along the rows of the camera so we summed 30-40 pixels along columns to get a 1D spectrum. Diffuse background is removed at this point by interactively fitting a line to the selected parts of the spectrum (usually close to endpoints) and the spectrum is then saved in FITS format.

3.3 RESULTS

We made throughput measurements in all three modes using an uncoated, polished silicon prism as a reference mirror since none of the grating surfaces had been coated. The performance of our grating in all modes was determined by integrating intensity in all observed orders and comparing this value to the reflection from the silicon mirror (the reflectivity of a single silicon surface at normal incidence is 30.6%). The measured arm coefficient of 1.09 (the difference in the return loss for the two arms due to the slightly different incidence angles of the reflected beams at the beam splitter) was used to correct all measurements in immersion/reflection but not for grism measurements since there was no Arm 2 in transmission. The summary of measurements and predicted performances is given in Table 3.1. The measurement errors mostly result from uncertainties in the arm coefficient measurements. The upper bound on arm coefficient measurement error is 3.0%. The absorption coefficient for silicon is 0.0103 cm^{-1} at 1.5

Table 3.1. Measured throughputs at 1.523 μm compared to a silicon grism (front surface reflectivity of 30.6% for normal incidence). Predicted η/η_0 values given in the last column are based on the RMS spacing error of 37 nm calculated from the measured throughput at 632 nm. Due to non-simultaneous measurements of grisms and the reference mirror, errors in efficiency determination in the transmission mode are large resulting in measured efficiencies >100%.

Mode	**Measured throughput (η)**	**Ideal throughput (η_0)**	**Measured η/η_0**	**Predicted η/η_0 for $\Delta\sigma_{RMS}$=37 nm[a]**
Reflection (at 632 nm)[a]	70.0	93.0	76.3	76.3
Reflection	85.5	93.0	91.8	95.4
Immersion	25.9	48.2	53.7	56.8
Transmission	30.5	28.1	108	93.1

[a](Ershov et al. 2001)

μm at 290 K (Eagle Picher) resulting in 0.86% of incident light being absorbed by a silicon disk 10 mm in thickness. The error in our calculation resulting from neglecting absorption in silicon is then 1.7% for immersion and 0.9% for transmission.

When used as a front surface grating, our device had net throughput of 85.5%±3.0% in three orders at 1.523 μm. This measurement is compared to an ideal throughput of η_0=93% (values given in column 3 of Table 3.1). The value of η_0 differs from 100% because of losses resulting from shadowing by groove tops which effectively constitute a grating blazed at 0° thus removing 7% of light from the spectrum. Table 3.1 also lists a throughput predicted based on an RMS error in the groove positions of 37 nm (column 5). This value was derived from the reflection throughput measurements at 632 nm (Ershov et al. 2001) listed in the first row of the table. The difference between the measured relative throughput of 91.8% and predicted value of 95.4% is consistent with the measurement error for the grating in reflection. Since our grating is not blazed at exactly 1.523 μm, we calculated the throughput of our grating for monochromatic light at the blaze wavelength (Schroeder and Hilliard 1980) and got 57%.

In transmission, the measured throughput was 30.5%±0.9% in four orders at 1.523 μm. The large blockage from the adjacent grooves at the blaze angle of 54.7° (46% of the surface is shadowed by adjacent grooves) results in large geometrical losses and distribution of light over many orders (due to widening of the blaze function with smaller effective groove width). Our calculations indicate that only 28.1% of incident light on the grism should be diffracted into orders and that the rest should be lost in two reflections from silicon surfaces and geometrical shadowing. This shadowing effect becomes much smaller at shallower blaze angles. The relative throughput of our grism is 108% compared to the expected 93.1%. Clearly, the situation where the geometric blockage is very large requires more attention and more careful modeling. The measured

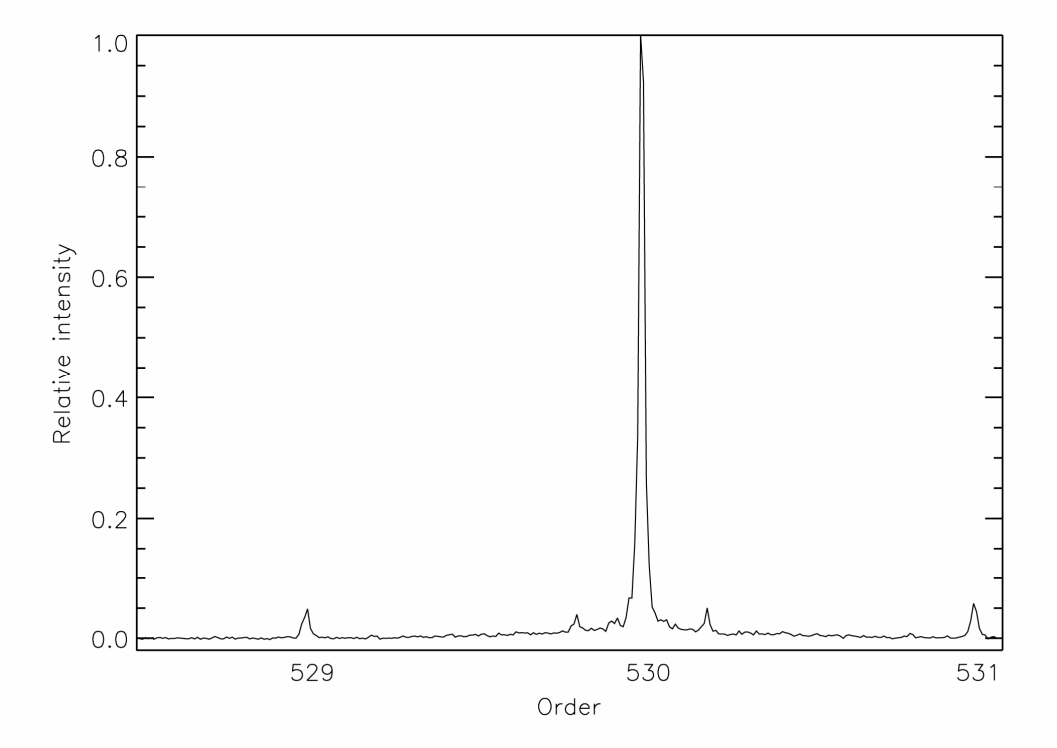

Figure 3.3. Immersion grating spectrum at 1.532 μm. Scattered light and ghosts are shown in more detail in Figure 3.6.

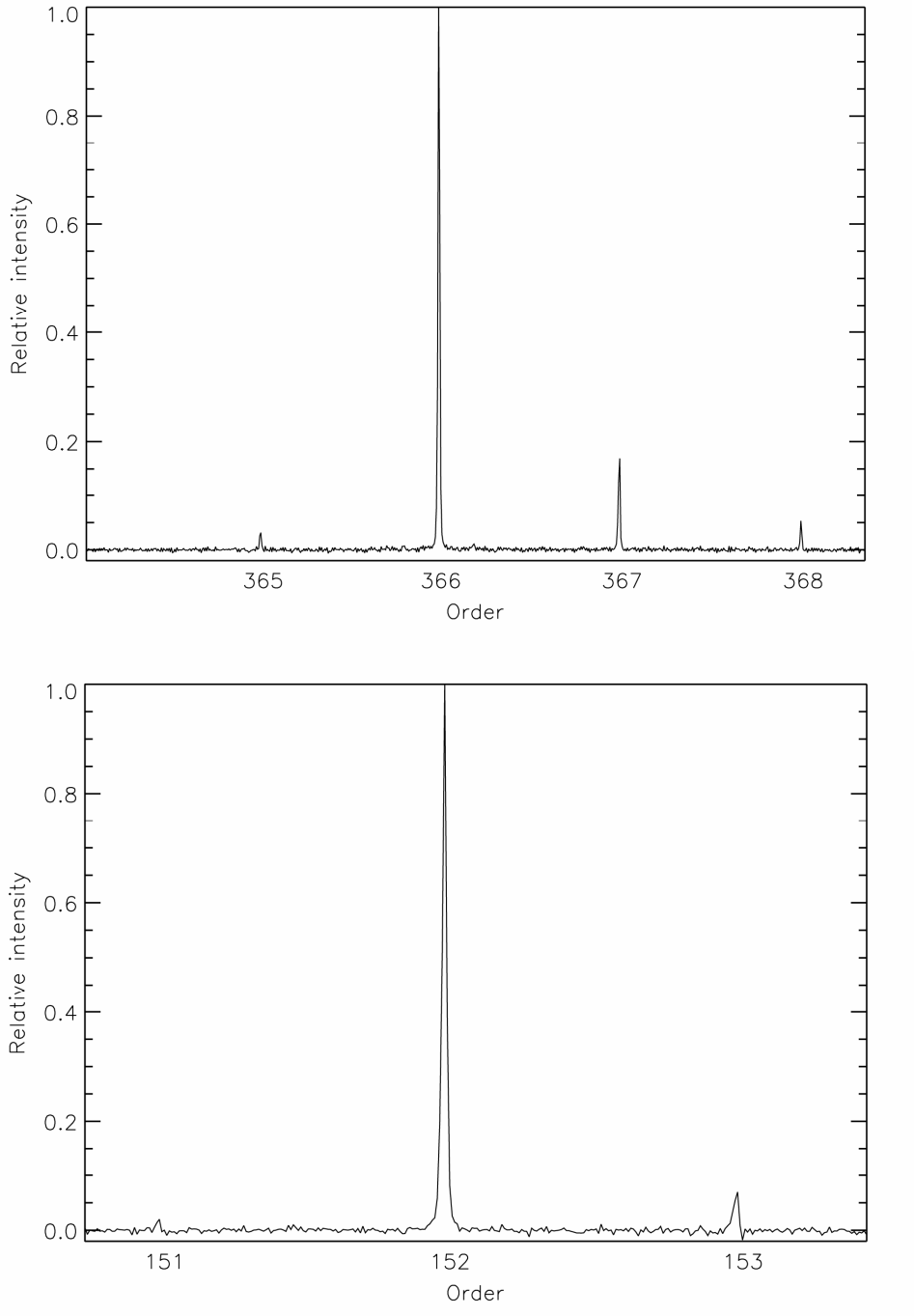

Figure 3.4. Spectrum of the grating used as a front-surface device at 632 nm (*top*) and 1.523 μm (*bottom*).

throughput of our grating in immersion was 25.9%±4.7% in three orders (after subtracting out scattered light and ghost contributions). There is no loss in immersion from geometrical blockage. In this mode, the beam undergoes two transmissions and one reflection at uncoated air/silicon interfaces. The maximum achievable throughput is therefore 48.2% relative to the silicon reference mirror. The measured relative throughput in three orders was 53.9%±4.7% in agreement with the predicted 56.8% (again, assuming $\Delta\sigma_{RMS}$=37 nm as determined from the front-surface measurements at 632 nm). Another 15.1% is recovered in blazed scattered light and 1.5% in Rowland ghosts (see Figure 3.6). In immersion, the blaze wavelength is very close to 1.523 μm and the throughput of our grating on the blaze (Schroeder & Hilliard 1980) would be 33%.

The presence of Rowland ghosts (small satellite lines found on each side of the parent spectral line) in the immersion spectrum indicates periodic errors in groove spacing in our case transferred from the photolithography mask. The distance of Rowland ghosts from the parent line is given by (Stroke 1967):

$$\Delta x = M \frac{\lambda f}{P \cos\delta} \tag{3.3}$$

at Littrow incidence where M is the ghost order, P is the period of the spacing error, and f is the focal length of the camera lens. The relative intensity of Rowland ghosts is proportional to the square of the amplitude of the periodic spacing error and for a grating in immersion it is given by (Stroke 1967):

$$\frac{I_{ghost}}{I_{line}} = \left(\frac{2\pi n}{\lambda} A \sin\delta \right)^2 \tag{3.4}$$

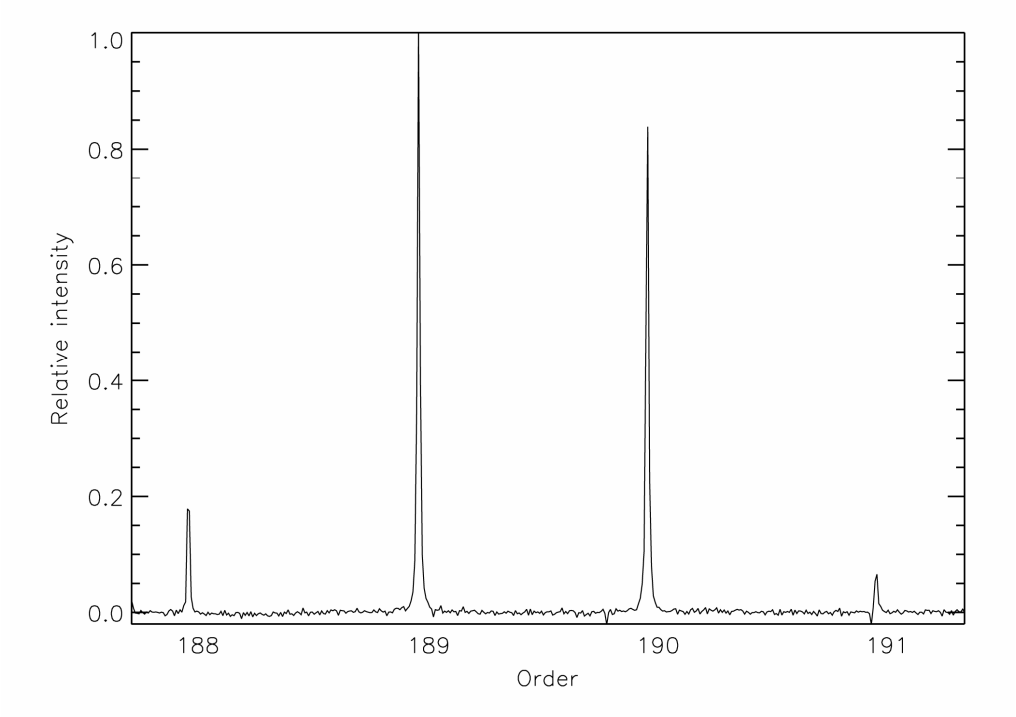

Figure 3.5. Grism spectrum at 1.523 μm.

From the measured distance (22.5 pixels) and intensity (~2.6%) of Rowland ghosts, we determined the period and amplitude of the spacing error P=780 μm and A=13.5 nm. The result is very close to the result we got previously (Keller et al. 2000), P=726 μm and A=17.5 nm, using front surface tests (λ=543 nm) of a grating etched on a silicon wafer. The periodic error causing Rowland ghosts in our spectra is solely the result of using a ruled mask. We have already used new e-beam masks which show no evidence of Rowland ghosts.

Scattered light normally present in a grating spectrum is usually a result of imperfections in groove walls. However, we also find scattered light in the immersion spectrum spread within the envelope defined by the blaze function. Blazed scattered light is most likely due to random errors in groove positions. The presence of both types of scattered light degrades the performance of our grating at 1.523 μm (which, in immersion, is the equivalent of 437 nm for a front-surface device). One of our primary goals for the immersion gratings project is to produce a device with good performance in the 3 - 4 μm band. We therefore modeled the performance of an immersion grating with our current level of groove position error but without the now avoidable repetitive error at 3.5 μm. Figure 3.7 shows the result of this calculation. The throughput of this grating on the blaze at 3.5 μm would be 61% in 227th order.

3.4 CONCLUSION

We tested a diffraction grating produced by wet etching of a silicon disk and then cut into a prism with the grating covering the hypotenuse side. Leaving the grating uncoated enabled us to test the grating in immersion, reflection and transmission and compare its performance in all three modes. We conclude that the performance of our grating is very close to the performance we expected based on our previous

measurements. The errors in groove spacing that degrade the performance of our grating in immersion can be attributed to mask imperfections. We have addressed this problem and are now able to acquire e-beam masks that do not have periodic errors.

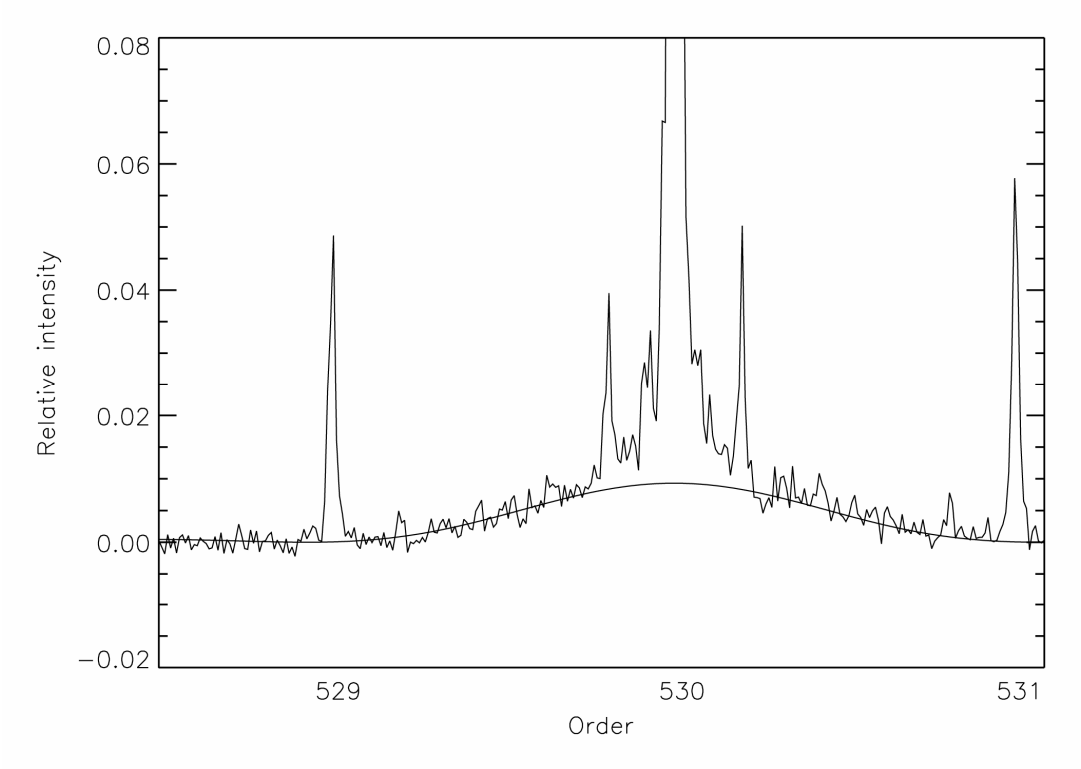

Figure 3.6. Immersion grating spectrum detailing scattered light and ghosts. Rowland ghosts are at a distance of 22.5 pixels from the parent line and their intensity ranges from 2.6% to 8.5% of the parent line. Scattered light has the shape of the blaze and in this case was fitted by the scaled blaze function.

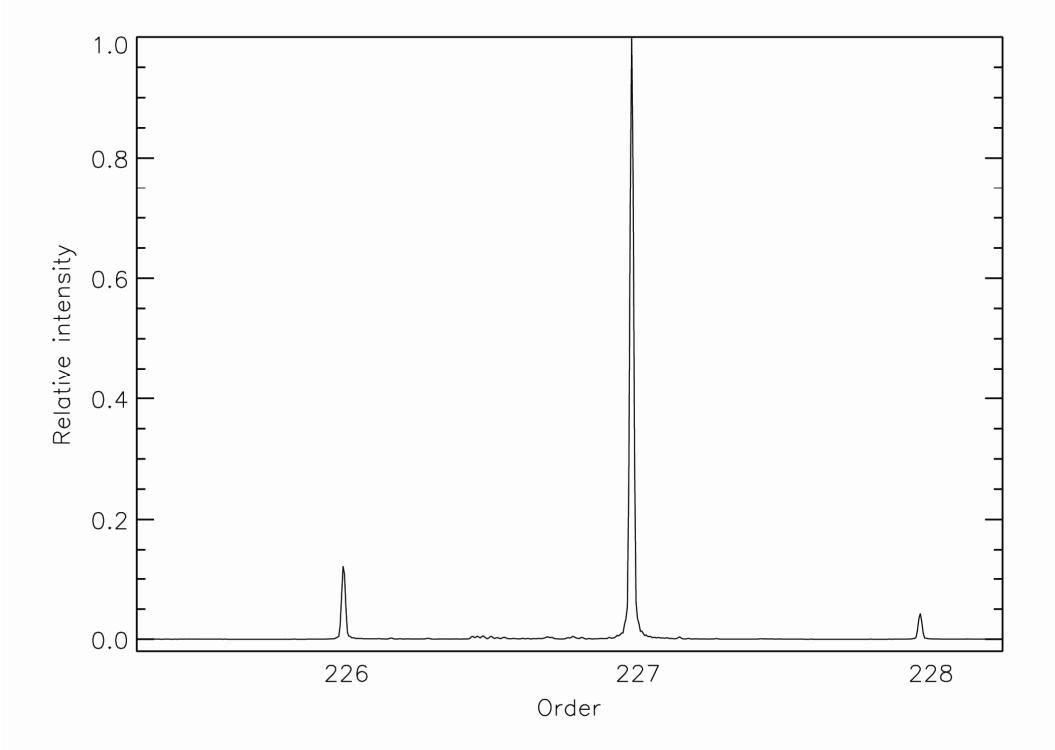

Figure 3.7. Simulated grating spectrum at 3.5 μm. The intensity if scattered light is significantly diminished and the grating performance is significantly improved.

Chapter 4.

Micromachined silicon grisms for infrared optics[2]

4.1 INTRODUCTION

Gratings mounted on or fabricated on wedged substrates combine the dispersive action of a diffraction grating with the varying optical path length across the prism, and are therefore called grisms, or Carpenter prisms. Typically, grisms are inserted into a beam of collimated or nearly collimated optical or infrared light and used to disperse the light as it is transmitted through the device. The primary geometrical parameters are the grism wedge angle δ and the grating period σ; these specify into which angles the various wavelengths and orders are diffracted. The grating equation applied to a grism is:

$$\frac{m\lambda}{\sigma} = n\sin\left[\delta - \sin^{-1}\left(\frac{\sin\alpha}{n}\right)\right] + \sin\beta \qquad (4.1)$$

where m is the order where the grating is used, λ is the (vacuum) wavelength, and n specifies the index of refraction of the grism material. The angle δ is the prism wedge angle, and α and β specify the angles of the incident and transmitted beams with respect to the normals at the entrance and grating (exit) faces of the prism (see Figure 4.1). A

[2] This chapter contains the paper authored by D.J. Mar, J.P. Marsh, and D.T. Jaffe, to be submitted to Applied Optics. The author of this dissertation contributed some of the text and made a significant intellectual contribution to this work. A substantial fraction of the material presented here is based on her research.

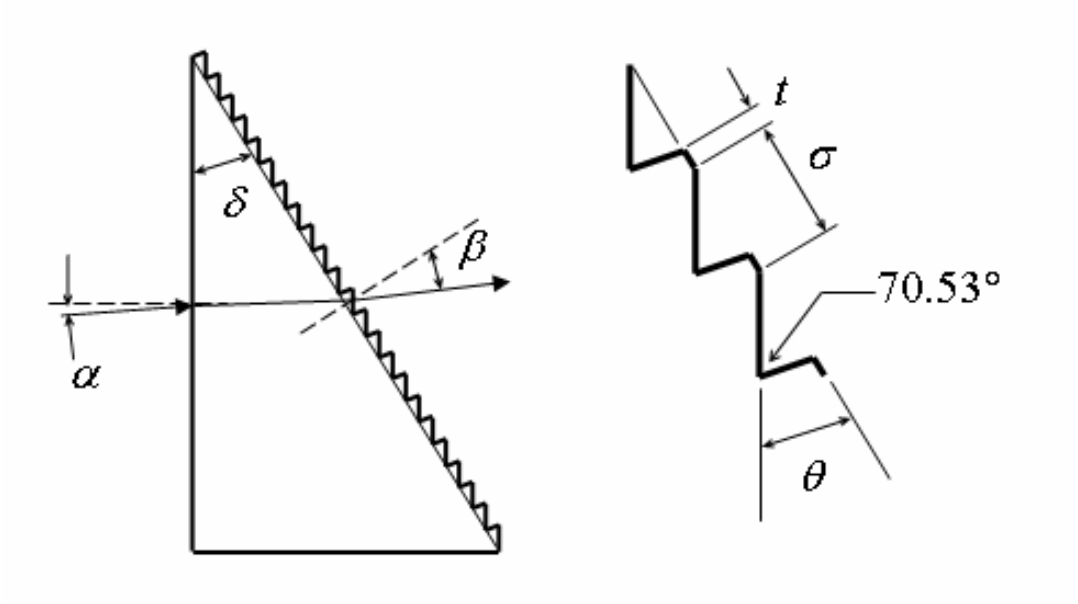

Figure 4.1. *Left*: Schematic diagram of a grism with wedge angle δ. The incident angle α and diffracted angle β are measured with respect to the corresponding normal to the surface of the grism and the sign convention is that both angles are positive in the sense drawn. *Right*: Detail of a silicon grating surface showing groove period σ. The plane of the figure is the (110) crystal plane. For the Littrow configuration shown here, the blazed facets are parallel to the entrance surface and $\theta=\delta$, where θ is the blaze angle between the groove facet and the grating surface . For silicon grisms in which the facets are adjacent {111} crystal planes, the valley angle measures 70.53°. For the situation in which the facets are non-adjacent, the valley angle is 109.47° (not shown in figure, but see Ershov et al. 2003). As shown, for acute valley angles, the projection along the optical axis of the unused facet and the groove top t partially coincide, reducing the geometric transmission loss.

beam that passes through without deflection satisfies $\beta=\alpha - \delta$, and Eq. 4.1 becomes

$$\frac{m\lambda}{\sigma} = n\sin\left[\delta - \sin^{-1}\left(\frac{\sin\alpha}{n}\right)\right] + \sin(\alpha - \beta) \tag{4.2}$$

Figure 4.1 shows an example of a blazed grating in which the groove facets are parallel to the entrance face. For grisms that are blazed this way, the blaze wavelength condition occurs when $\delta=\beta$:

$$\frac{m\lambda_{blaze}}{\sigma} = (n-1)\sin\delta \tag{4.3}$$

and light at the blaze wavelength passes through the grism undeviated. For modest angle grisms (δ<40°) used in low order, reasoning from scalar electromagnetic theory predicts a maximum in the efficiency at wavelengths near λ_{blaze}, although for larger δ a more rigorous treatment may be necessary (Nevière 1991). The diffraction-limited resolving power for nearly normal incidence ($\alpha\approx0$) is given by

$$R = \frac{\lambda}{\Delta\lambda} = (n-1)\ \tan\delta\ \frac{D}{\lambda} \tag{4.4}$$

where D is the pupil diameter. For a given wavelength λ and resolving power R, D is inversely proportional to n-1. Thus, the size of the pupil (and hence the optical apparatus) can be reduced by selecting grisms made from high index material rather than low index material. Equivalently, for a given D/λ ratio, the resolving power is increased by choosing a material with a high refractive index (see Table 4.1), or by going to larger grism angles.

The grating side of a grism is a periodic array of diffracting elements, and is usually formed by one of four methods: ruling, replication, diamond-machining or patterning/etching. For visible wavelengths, ruled gratings in glass or replica gratings in resin that can be mounted on prisms are commercially available (Carl Zeiss, Inc. 2004, Newport 2005). At longer wavelengths, however, optical transmission properties can limit the choice of material, as most resins become absorbing beyond about 3 μm. Also, the groove spacing of an infrared grating is typically larger than that for a visible light grating by about an order of magnitude. This can preclude the selection of ruled grisms, as it is difficult to control the blaze when removing large amounts of substrate material. Diamond-machining techniques (Davies et al. 2003) can generate both intricate and coarse structures on many substrates (including metals, Si, ZnSe, Ge, and many polymers) with very low surface roughness (~5 nm), but the surface may still possess long-wavelength machining defects such as cutting arcs and ripple. For large area gratings, there can still be issues with cutting tip wear, due to the serial way in which each groove is created. This serial processing is relatively slow and therefore demands high thermal and mechanical stability during the machining. An alternative fabrication method using lithography and anisotropic etching is, by contrast, a parallel method. These processes can produce coarser groove spacings with excellent blaze characteristics and surface quality. They are particularly suited for single-crystal materials in which the crystalline directions are maintained throughout the entire substrate. In this work we focus on near and mid-infrared applications using silicon (see Section 4.2).

In optical applications, grisms are often used as compact dispersers that do not appreciably deviate the direction of a collimated beam at the blaze wavelength. From Eq. 4.1 it can be shown that

$$\sin\beta = \frac{m\lambda}{\sigma} - n\sin\delta + \sin\alpha\cos\delta + O\left(\frac{\sin\alpha}{n}\right)^2 \qquad (4.5)$$

Table 4.1. Potential infrared grism materials and properties.

Reference	**Material**	**Index**[a]	**Grism type**[b]	**Bandpass (microns)**	**Comment**
Carl Zeiss Inc. 2004)	resin / BK-7	1.5 / 1.5	replica, hybrid	0.3 - 2.5	
	CaF2	1.4	ruled		
Rayner (1998)	KRS-5	2.4	ruled	0.5 - 35	
Ebizuka, Iye, and Sasaki (1998)	LiNbO3 / ZnS	2.2 / 2.2	etched, hybrid	0.35 - 4.6	birefringent
	ZnSe	2.5	ruled	0.6 - 21	brittle, low efficiency
	Si	3.4	etched	1.2 - 15, 17 - 35	monolithic
Kaüfl, Kühl and Vogel (1998)	Si / Ge	3.4 / 4.0	ruled, hybrid	1.8 - 23	

[a]The indices of refraction are for comparison purposes only, since the actual index varies with wavelength and temperature.
[b]Hybrid grisms are formed by fabricating the grating on a thin substrate and then attaching the grating to a thicker prism substrate (e.g. resin on BK-7).

This implies that small misorientations of the grism are not catastrophic (Kaüfl et al. 1998). For example, for a Si grism with n=3.4, δ=6.16°, and σ=87 µm operating at m=1, a device tilt of 1° in the dispersion axis leads to a deflection of the central blaze wavelength of less than 0.001°. It can also be shown from Eq. 4.1 that $d\beta/d\lambda$ is approximately constant with small changes in incidence angle $\Delta\alpha$. Since the transmitted light through a grism is not very sensitive to the angular orientation of the device (see Section 4.1), grisms may be mounted in filter wheels or similar inexpensive mechanisms that do not have extremely tight tolerances on the angular positioning.

The incident beam may in fact be slightly uncollimated. To estimate to what degree this is acceptable, we require that the change in α across half the f/cone results in an outgoing angle change corresponding to less than half the angular size $\Delta\beta=R^{-1}/2=\lambda/[2D(n-1)\tan\delta]$. For small α and β, Eq. 4.5 leads to

$$\Delta\alpha \approx \Delta(\sin\alpha) \approx \Delta(\sin\beta)/\cos\delta \approx \Delta\beta/\cos\delta = \lambda/[2D(n-1)\sin\delta] \qquad (4.6)$$

For λ=5 µm, D=25 mm, n=3.4, and δ=6.16°, Eq. (6) yields $\Delta\alpha$=0.4 mrad=1.3 arcmin. Because the light rays pass through the grism undeviated or nearly so, downstream optics can support both imaging or spectroscopic modes, depending on whether or not the grisms are in the path of the beam or not. The use of grisms can thereby simplify the design of a multifunction instrument. They therefore have found a place in many near-infrared (IRCS-Subaru, Kobayashi et al. 2000; NIRC-Keck, Matthews and Soifer 1994; NICMOS-Hubble, e.g. Freudling 1997), and mid-infrared (TIMMI2-ESO, Reimann et al. 1998; MIRSI-IRTF, Deutsch et al. 2003; VISIR-ESO, Lagage et al. 2004) astronomical spectrographs. Other potential applications for grisms include dispersion of wavelength-multiplexed light signals into an array of beams, thereby providing simultaneous

demultiplexing with a “single grating coupler” element instead of a bank of filters for optical communication in the near-IR (Philippe et al. 1985, Zhao et al. 2001) or confocal microscopy (Tearney et al. 1998, Pitris et al. 2003) at visible wavelengths. Another potential application uses combinations of grisms to compensate higher order dispersive effects when compressing and stretching light pulses, a technique that makes them potentially useful for time-domain laser pulse applications Tournois 1993, Kane and Squier 1997).

The work here demonstrates the fabrication of high quality silicon grisms with coarsely spaced grooves for near and mid-infrared spectroscopy applications (see Table 4.2). We discuss the choice of silicon as a suitable material, report on the techniques and methods used to fabricate the grisms, discuss factors that can limit their performance, and display finished devices that have high efficiency over large (2.5 cm and up) aperture diameters. As a direct consequence, the grisms exhibited here will provide a mid-infrared camera on an airborne astronomical observatory with moderate resolution spectroscopy capabilities. Large, coarsely-ruled silicon grisms may be combined in cross-dispersed configurations to enable a new capability: moderate to high-resolution spectroscopy in the near-IR using all-transmissive optics.

4.2 SILICON

Silicon is an important and useful optical material because of its optical and mechanical properties, and because process technologies have been developed for semiconductor VLSI electronics and MEMS applications. High-purity silicon transmits well in the near and mid-infrared (1.2 to 40 μm) wavelength regions (Fan and Becker 1950, Spitzer and Fan 1957, Runyan 1965, Schroder et al. 1978) and beyond, although there are some sub-regions in which silicon absorbs. Infrared lattice absorption can be

Table 4.2. Summary of design parameters for silicon grism devices shown in this paper. See Figure 4.1 for the definitions of the various dimensions.

Grating	δ **(°)**	θ **(°)**	σ **(μm)**	t **(μm)**	**designed for**	
					m	λ_{blaze} **(μm)**
G2	6.16	6.16	25	2.5	1	6.6
G3	32.6	32.6	87	6.0	14-23	8.2
G4	6.16	6.16	87	6.0	1	22.8
G5	11.07	11.07	142	10.0	2	33.3

observed from 8 to 25 µm (Collins and Fan 1953). Except for particularly strong absorption near 16 µm, the absorption can be reduced by lowering the temperature. Narrow and strong absorption features due to oxygen can occur near 9 µm and 19 µm (Kaiser et al. 1956, Hrostowski and Kaiser 1957, Livingston et al. 1984). For infrared applications from 1 to 40 µm, the use of float-zone (FZ) silicon is preferred because its lower oxygen content reduces these absorptions (see Figure 4.2). Other absorption features occur to 40 µm (Lord 1952). The short wavelength cutoff occurs at a wavelength of approximately 1.1 to 1.2 µm (Dash and Newman 1955, MacFarlane et al. 1958) at the silicon bandgap. At lower temperatures the cutoff moves slightly towards shorter wavelengths (~1.07 µm at 77 K). For silicon diffraction gratings that are fabricated using wet-etch processes to create the diffracting surfaces, a low oxygen content also contributes to the facet smoothness (Kwa et al. 1995, Merveille 1997), although it is not clear that the surface roughness of the facets is the dominant scattering process (Kuzmenko and Ciarlo 1998). The high index of refraction (n = 3.44 at λ = 2.4 µm) permits large dispersing power in a small device, as the resolving power in Eq. (4) can be larger by a factor of 5 than for a grism made from modest index material such a CaF_2 or from a resin. The optical index decreases from ~3.44 to ~3.41 as the temperature is lowered from 300 K to 77 K (Schroder et al. 1978, McCaulley et al. 1994). Mechanically, silicon is hard, possesses a high elastic modulus, and can be polished to high optical flatness. It is vacuum-compatible and its optical transmission in the near-infrared improves slightly with decreasing hydrostatic pressure (Neuringer 1959). When cooled to the cryogenic temperatures required for sensitive infrared optical measurements, it is mechanically stable and has a modest thermal contraction relative to those of metals and other mounting materials. It is possible to apply antireflection coatings to a polished silicon surface to enhance the near-IR (1.2 - 5 µm) transmission

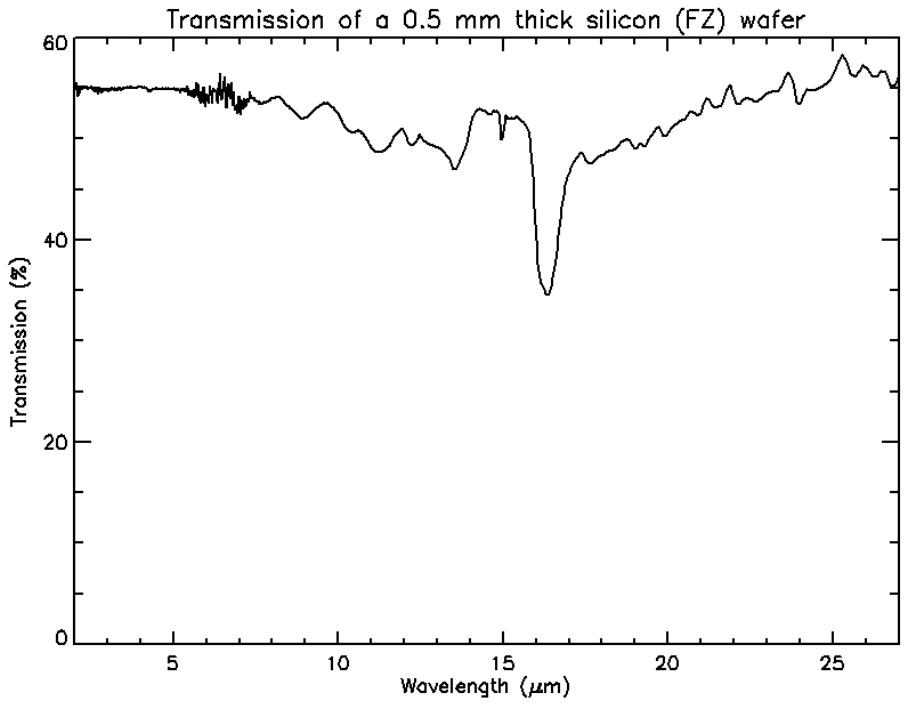

Figure 4.2. Infrared transmission from 3 to 27 μm of a 0.5 mm thick sample of high-purity float-zone Si, measured at 300 K using Fourier Transform Infrared Spectroscopy (FTIR). Except for lattice absorption near 16 μm, the sample has good transparency. The oxygen absorption features at 9 and 19 μm (Kaiser et al. 1956, Hrostowski and Kaiser 1957, Livingston et al. 1984) are largely absent in this case but will still cause a significant drop in transmission for thicker substrates. The reflectivity of a single silicon surface is 30% at 3-5 μm and the resulting transmission is 55% when contributions from all re-reflected light are accounted for.

at the silicon-vacuum (or silicon-air) interface.

Fabrication of diffraction gratings in silicon exploits lithographic processes that have been developed for industrial applications. The patterning of precisely positioned periodic grooves can be accomplished by photolithography methods (Thompson et al. 1994) that permit precise pattern transfer onto a silicon surface that has been polished optically flat. In combination with anisotropic wet-etch techniques that preferentially etch along the <100> directions hundreds of times faster than along the <111> directions (Lee 1969, Seidel et al. 1990), lithography permits the fabrication of precisely positioned and aligned {111} facets in the grating surface (Tsang and Wang 1975). Control of the groove orientation is achieved by the underlying atomic structure. For single crystal silicon, the orientation of the grooves is essentially perfect. The high etch anisotropy leads to groove profiles that are flat and smooth from the groove top to the valley (see Figure 4.3).

4.3 FABRICATION

Over the past decade, several groups have developed methods for fabricating diffraction gratings on silicon substrates (Wiedemann and Jennings 1993, Kuzmenko et al. 1994, Graf et al. 1994, Keller et al. 2000, Vitali et al. 2000, Ershov et al. 2001, Vitali et al. 2003, Ershov et al. 2003, Ge et al. 2003, McDavitt et al. 2004). Substrates that are considerably thicker than standard semiconductor wafers necessitate some modifications to semiconductor processing methods. We have developed methods to produce gratings with asymmetric groove profiles (see Figure 4.3), a necessary step for the production of low-order grisms (Ershov et al. 2003). We have been successful in producing high-quality gratings on monolithic substrates, thus producing grisms designed for use between 5 and 38 μm that are complete (see Figure 4.4) except for commercial anti-

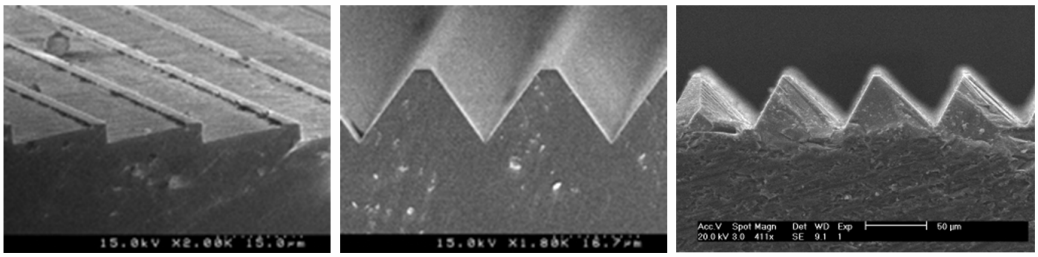

Figure 4.3. Scanning different blaze angles δ and groove constants σ: (a) δ=6.16° and σ=25 μm, (b) δ=54.7°and σ=25 μm, and (c) δ=63.4° and σ=80 μm. The grooves in (b) are symmetric with respect to the top surface. In all three panels the sloping faces are very nearly parallel to {111} crystal planes. From surface profilometry, we obtain valley angles of 72.12° with a measurement uncertainty of 0.05°. The small difference between this value and the $\cos^{-1}(1/3)$=70.53° angle between nearby {111} planes reflects undercutting arising from the finite etch anisotropy. This figure is taken from Ershov et al. (2003).

reflection coating. Our fabrication methods are described in this section.

Our production starts from blanks of high-purity monocrystalline silicon. Silicon is commercially available as boules of various diameters (e.g. 100 mm, 150 mm, 200 mm) and resistivities. For the lowest infrared absorption at λ>5 µm, single-crystal material with low-oxygen content is used. During wet-etch processes, crystal defects can produce pits and hillocks (Tan et al. 1996) that can scatter light in optical applications. These issues have led us to favor float-zone (FZ) material with resistivities in excess of 1000 ohm-cm. The crystal growth axis of silicon boules is accurate to within ~1°. This level of accuracy is insufficient to prevent dislocations from appearing during the micromachining of long grooves. We therefore have the boule oriented more precisely by using x-ray diffractometry to locate the crystal directions to within 0.05°. A precision {110} flat is then ground on one side of the boule. This flat is perpendicular to the grating surface and to the groove facets (see left image in Figure 4.1) and serves two purposes: it provides a stable platform upon which to mount the boule for subsequent cutting, and serves as an alignment marker in later lithographic steps. The boule is then sliced into blanks of sufficient thickness (typically 10-20 mm) to accommodate the grism and to guarantee its rigidity. The blaze angle θ is determined by bias-slicing the boule at the appropriate angle. For example, if the surface exposed by the slice is a {100} plane, a symmetric (θ=54.7º) grating will result (see middle panel of Figure 4.3), whereas rotating the boule around the <210> axis by some angle willproduce gratings with asymmetric groove profiles (see Ershov et al. 2003 and left and right panels in Figure 4.3). The exposed surfaces are then ground, etched to remove saw damage, and the top surface is polished to optical flatness (surface figures less than 1/50 wave RMS at 632.8 nm) using chemical-mechanical planarization (CMP) processes. This results in an extremely flat surface (RMS errors under 6 nm) while minimizing mechanical stresses at and near the

Figure 4.4. Images taken of silicon gratings after wet etching, before (*left*) and after (*center, right*) devices have been shaped into wedges. The left photograph is taken in Littrow (note the image of the camera) and the camera flash has been dispersed left-right by the grating. The major axis measures 76 mm. For the grisms in the center and right images, the wedge angles δ are clearly visible and the ruled surfaces are towards the viewer. In the center image, the polished entrance face of the grism on the right (grating area 51 mm×50 mm) is seen reflected in the ruled surface of the grism on the left (grating area 51 mm×57 mm). In the right image, the corresponding area is 37 mm×32 mm. Only commercially-available anti-reflection coatings are needed to complete the wedged grism devices. From left to right, these four gratings are G2, G5 & G4, and G3 as listed in Table 4.2.

surface (Nanz and Camilletti 1995). The blanks are then coated with a thin (60-100 nm) low pressure chemical vapor deposition (LPCVD) silicon nitride as a passivation layer.

At this point, we create a series of regularly spaced lines on the nitride layer using photolithography. Many of the lithography steps are described in previous papers (Graf et al. 1994, Keller et al. 2000, Ershov et al. 2001, Ershov et al. 2003). Our lithographic process employs a positive photoresist that is flood-illuminated by g-line (436 nm) and i-line (365 nm) light from a mercury-gallium lamp. To spin-coat the photoresist onto the massive blanks, we employ a custom-built spin table with sufficient torque to spin the combined moment of inertia of the puck and holder up to several thousand rpm in a period of a few seconds. Once the photoresist has been cured by heating the blank to 110°C for 20 min, a chrome-on-quartz mask containing the negative of the desired grating pattern is placed in contact with the photoresist layer. The flood illumination through the mask transfers the mask pattern to the photoresist layer. The exposure system is a custom designed apparatus that can accommodate a wide range of substrate thicknesses (0.5-35 mm). During the exposure step, the temperature of the silicon blank and the quartz mask are held to within a few °C across the grating, thereby preventing potential pattern transfer errors arising from the different thermal expansions of the substrate and mask.

After the photoresist has been exposed, an image of the mask pattern is produced in the photoresist layer by immersing the photoresist-coated blank in a commercial developer solution. Next, the nitride layer is patterned using a dry (plasma) etch. The photoresist layer serves as an etch mask during this step. Thick substrates undergoing plasma etching can display nonuniform etching, due to variations in the electric field profile and in the plasma density within a reactive ion etch (RIE) chamber that is normally used to process thin semiconductor wafers. We have modified our plasma

etcher to maintain uniformity of the plasma in contact with the patterned surface. After the dry etch, the photoresist is stripped by immersion in acetone. The groove facets themselves that form the grating are then created by anisotropic etching in an aqueous solution of potassium hydroxide and isopropanol, maintained at 68ºC by immersion in a recirculating water bath. Ultrasonic vibrations assist in detaching bubbles from the etched surface. During the wet etch, the etch rate and orientation anisotropy determine the amount of undercutting within the silicon. Both of these quantities are temperature-dependent. To prevent the temperature from dropping appreciably and affecting the rate and anisotropy when the silicon blank is immersed into the solution, we generally preheat the solution by several degrees.

Etching in potassium hydroxide creates a blazed grating over the entire patterned area of the silicon surface. A photograph of a processed blank is shown in the left panel of Figure 4.4 and scanning electron microscope (SEM) micrographs of micromachined silicon gratings are shown in Figures 4.3 and 4.5. The nitride strips that protected the groove tops (see Figure 4.5) during anisotropic etching are removed by immersing the grating in hot concentrated phosphoric acid. Removal of the nitride promotes adhesion of antireflection coatings that are subsequently applied to the grating surface.

To form a complete grism, the blank is cut into the desired prism shape. For the devices in this paper, the entrance faces are formed parallel to the grating facets ($\delta=\theta$). These faces are optically polished to high flatness, with final surface figures less than ~1/20 of a wave RMS at 632.8 nm. These devices are now complete (see middle and right panels in Figure 4.4) except for anti-reflection coating on the entrance and grating of the prism.

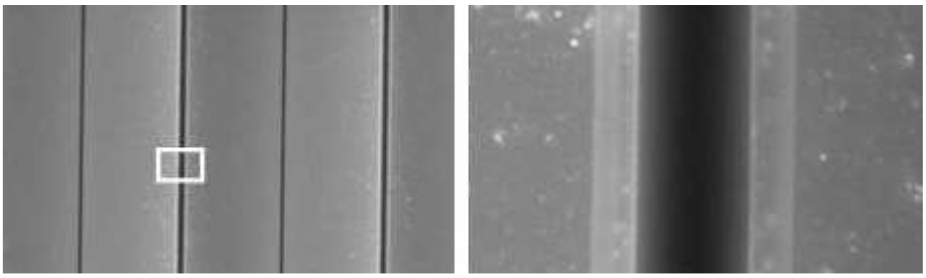

Figure 4.5. SEM micrographs of symmetric (θ=54.7°) gratings immediately after etching in potassium hydroxide, viewed normal to the grating face. The grating period is σ=142 µm. The thin dark vertical lines are the groove tops and valleys. The detailed view at right corresponds to the white box inset in the left panel. One can see the strip of silicon nitride covering the darker groove top and overhanging by approximately 2 µm at each edge of the groove top. The silicon nitride and the silicon hydroxide precipitates are effectively removed by washing the part in hot (150°C) ortho-phosphoric acid.

4.4 FACTORS AFFECTING GRATING PERFORMANCE

For applications such as infrared spectrographs which demand high sensitivity to faint sources, overall efficiency is a primary consideration. As light passes through the grism substrate and is diffracted by the grating, it is subject to losses that can limit the ideal optical performance of the grating: index mismatch loss at the entrance and exit faces, geometric losses, absorption and scattering within the bulk, scattering at the surface, and various types of groove errors (Jaffe et al. 1998). In this section we describe these potential sources of error and their possible effects on the grating performance.

Index mismatch losses (or Fresnel losses) take place at interfaces where there is a discontinuity in the index of refraction. Because the index of silicon is large (n=3.4), the substantial reflection loss at each of the two interfaces limits the transmission to $[4n/(n+1)^2]^2$=49%. By applying broadband anti-reflection optical coatings to the entrance and exit faces of the grism, the transmission can be raised to ~95%. Thick multilayer coatings might have even better throughput across a wide wavelength range, but may suffer from variations in thickness or uniformity that lead to phase errors, and may be challenging to apply to coarse gratings.

Losses occur where portions of the beam area are geometrically shadowed. For example, consider the right panel of Figure 4.1. For a normally-incident (α=0) beam from the left, most of the light passes through the vertical facet and is diffracted according to Eq. 4.1. However, at the top and bottom of each vertical facet, the light must pass through the shorter sloping facet in front of the groove top t. Depending on the value of α and on the details of the groove geometry, this light is diffracted into other directions and thereby lost from the main beam. In general, this loss is kept small when the projected areas of the unused facet and the groove top overlap as much as possible.

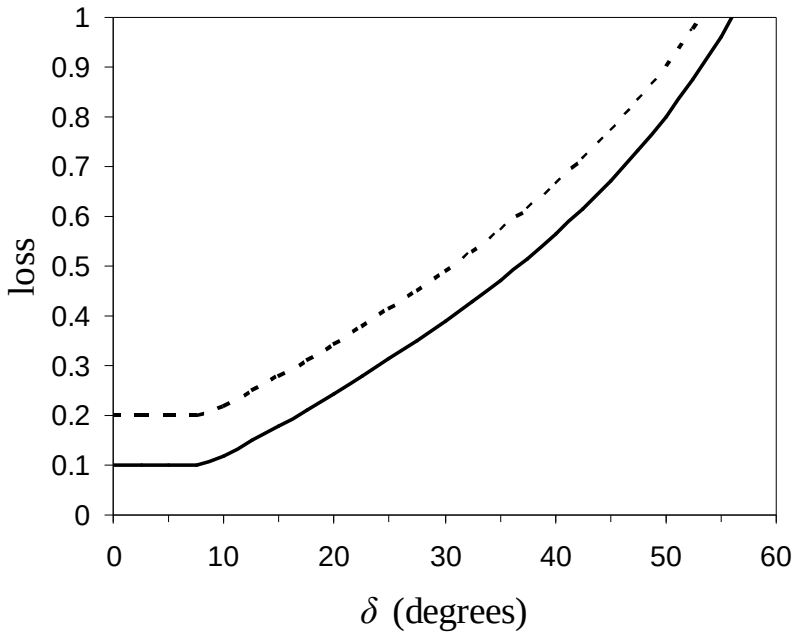

Figure 4.6. Geometric loss as a function of grism angle δ, for α=0 and fixed valley angles of 70.53° (solid curve) and 109.47° (dotted curve) between the facets of the grooves, for t/σ=5%. These curves include both the loss due to the unused area of the beam and the accompanying loss due to diffraction into undesired orders. For shallow angle grisms (δ<8°), the groove top dominates the shadowing and the curves are flat.

In the case of normal incidence and blaze parallel to the entrance face, the loss is minimized by using valley angles near 90° and keeping the groove top t as short as possible. However, a full EM calculation must be done to model the efficiency behavior of grisms in low order. The valley angle depends on the material and on the processing steps used to fabricate the grism. For silicon, it is possible to produce valley angles of either 70.53° or 109.47° depending on the crystal orientation (Ershov et al. 2003). Figure 4.6 shows that the choice of 70.53° is preferable, since the areas lost to the unused facet and to the groove top partially coincide in that case and therefore sustain less shadowing loss. The actual loss is a combination of geometric shadowing and diffraction (Babinet) loss. Scattering and absorption within the bulk silicon can also lower the optical throughput. To minimize these bulk effects the optical path length through the material should be kept as short as possible. The optical path length difference across the beam is the product of the beam diameter and n tan δ. Some additional substrate thickness is required to prevent flexure. By using high-resistivity (ρ>1000 Ω cm) float-zone silicon, for which the absorption coefficient can be small (e.g. $\alpha<10^{-3}$ cm^{-1} for λ between 1.2 and ~10 µm; Runyan 1965, Schroder et al. 1978), and by insuring that the grating fabrication steps neither create excessive damage to the silicon lattice nor introduce impurities that can scatter light, the absorption losses can be kept at the few percent level. Absorption features near 9, 16, and 19 µm, if present, may restrict the range of operating wavelengths. Processing silicon at elevated temperatures around 800-1000°C appears to be beneficial in reducing the infrared activity of oxygen defects (Hrostowski and Kaiser 1957); in our case, this processing is achieved during the deposition of the LPCVD nitride layer. Because the grism is a wedged device, differential bulk absorption/scattering occurs across the aperture. The linearly varying path length through the wedge results in an intensity that tapers exponentially across the grating and slightly

broadens the point spread function in the direction of the taper thus reducing the contrast in the sidelobe pattern. As illustrated in Figure 4.7, the effects on the width of the PSF are negligible.

Light can be scattered from imperfections at the grating surface. Some of these defects are randomly distributed, such as point defects and surface roughness. Leftover silicon nitride and other debris left on the surface (see the right panel of Figure 4.5) can also contribute to scattering. To assess the surface condition of the gratings on nanometer length scales, we use atomic force microscopy (AFM). Figure 4.8 shows an AFM scan of a 5 μm×5 μm portion of a groove facet of grism G2. As shown, the grooves are smooth: the surface roughness is less than 2 nm RMS and the groove facet is free from hillocks and etch pit formations (Tan et al. 1996, Campbell et al. 1995). Even if the grooves themselves are smooth (Figure 4.8) and flat (Figure 4.3), the overall grating performance could be degraded by any errors in the groove orientations and locations. Orientation errors are unlikely since the groove facets are aligned with the underlying silicon lattice, which is monocrystalline. Piston-type errors due to variations in groove placement arise from lithographic noise introduced during fabrication. Localized "jog" defects—abrupt changes in displacement within a single groove—could occur. Jog defects arise from pinholes in the silicon nitride, imperfections and impurities in the silicon lattice, or from irregularities in the width of the nitride lines that are patterned by the plasma etch. Ring-shaped variations in the density of jog defects were visible on early prototype devices. These patterns were attributed to variations in the plasma density during the RIE dry etch. After we made modifications to homogenize the electric field and plasma density in the plasma etcher, subsequent devices were largely free of these patterns. In other prototypes, the defects were visible across many adjacent grooves and were arranged in curved lines, indicating mechanical subsurface damage

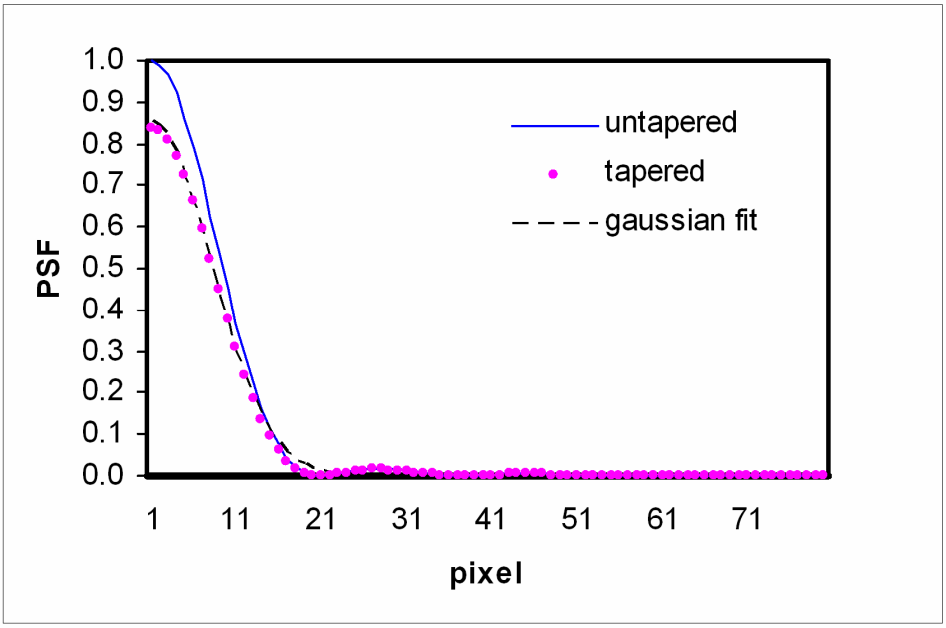

Figure 4.7. Computed point spread function for transmission of a 25 mm diameter collimated beam through a silicon grism with δ=32.6°, showing effect of absorption and tapering due to differential absorption in the silicon across the beam. The untapered (blue line) and tapered (dots) curves are calculated for Si absorption coefficients α=0 cm^{-1} and 0.2 cm^{-1} respectively. As shown, the main effect of absorption is to attenuate the intensity across the beam: the peak maximum has dropped by 16%. The width of the best Gaussian fit to the tapered profile (dotted line) has increased only slightly (approximately 0.1%) over the width of the best fit (not shown) to the untapered profile (solid line). At the center of the beam, the length in the Si is 8 mm.

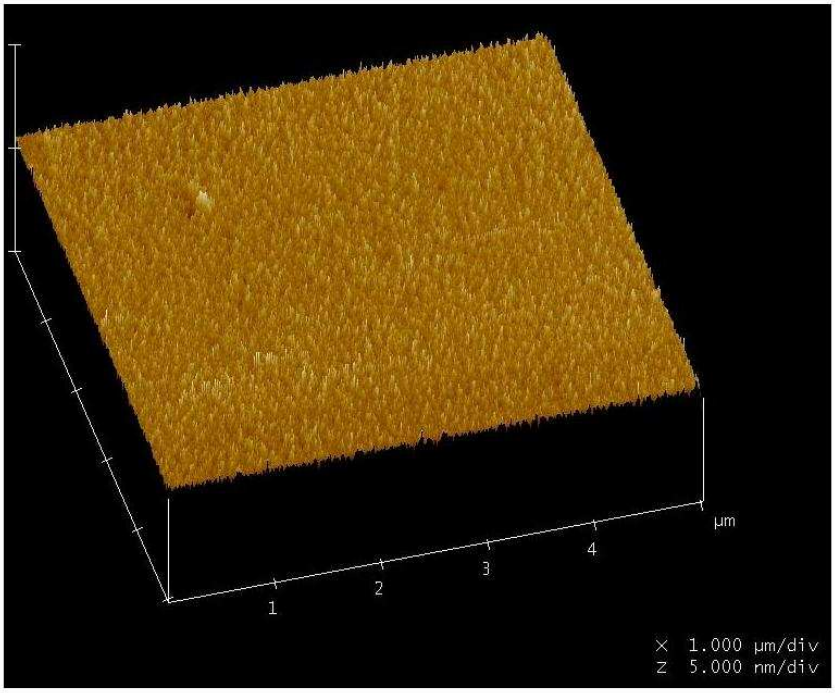

Figure 4.8. Three-dimensional representation of the surface of a groove facet obtained using an atomic force microscope (AFM). The field measures 5 µm×5 µm. The surface roughness over this area is measured to be 1.6 nm RMS. The roughness is unchanged across the entire facet. The bump at the upper left is 4 nm in height. The scan is taken from an offcut of grism G2 (δ=6.16° and σ=25 µm).

introduced during the CMP polishing step. If these jog displacements are large compared with the wavelength, they lead to inter-order power in the blaze. Assuming that these errors are Gaussian and uncorrelated, the grism phase error is

$$\varepsilon = \frac{2\pi(n-1)}{\lambda}\Delta\sigma_{RMS}\sin\delta \tag{4.7}$$

where $\Delta\sigma_{RMS}$ is the RMS deviation across the grating surface in the dispersed direction only. The phase errors degrade the peak efficiency in the following Strehl expression:

$$\frac{\eta}{\eta_0} = \exp\left(-\varepsilon^2\right) = \exp\left[-\left(\frac{2\pi(n-1)}{\lambda}\Delta\sigma_{RMS}\sin\delta\right)^2\right] \tag{4.8}$$

where η_0 is the maximum possible efficiency (see Chapter 2) . To maintain at least 80% of the incident power in a diffraction-limited spike, Eq. 4.8 implies that in silicon (n=3.4), the RMS errors must be maintained at $\Delta\sigma_{RMS}\sin\delta<\lambda/23$. If the silicon grating is used as a front surface reflective device in Littrow, the corresponding expression to Eq. 4.7 for the phase errors is $\varepsilon_o=2(2\pi)(\Delta\sigma_{RMS}\sin\delta/\lambda)$ and the corresponding 80% criterion is similar: $\Delta\sigma_{RMS}\sin\delta<\lambda/19$. The actual errors in the groove positions can be a combination of both Gaussian random errors and slow variations over longer spatial wavelengths. These long-wavelength errors could be introduced by various steps in the lithography, such as imperfectly flat substrates, imperfect contact between the lithography mask and the substrate, non-uniformity during the plasma etch, or variations in the wet etch environment (Jaffe et al. 1998).

To better understand these error sources, we have developed an array of diagnostics including SEM and AFM scans, surface profilometry, and optical

measurements in the visible and infrared. The information gained has been used to improve our grating fabrication procedures. Many groove error sources have been eliminated and those that remain are very small. In the next section we will demonstrate the excellent optical performance of our fabricated grisms and discuss what the results imply for the geometric, bulk, surface, and groove errors loss mechanisms discussed here.

4.5 PERFORMANCE MEASUREMENTS

To establish the extent to which the various sources of errors could affect the optical performance, we evaluate our fabricated silicon grisms by a combination of methods, including atomic force microscopy, scanning electron microscopy, surface profilometry, and optical measurements taken in reflection and transmission. The geometrical shape of the grooves across the surface is very good. From AFM and SEM scans, we know that the groove facets are smooth (see Figures 4.3 and 4.8), with roughness less than 2 nm RMS. Using surface profilometry and SEM micrographs of etch undercut, we obtain valley angles of 72.12º with profilometry measurement uncertainties less than 0.05º. This value is close to $\cos^{-1}(1/3)=70.53°$, the theoretical maximum value determined by the intersection of adjacent {111} families of crystal planes. The difference in angle is due to a finite anisotropy ratio of the etch rates in the <111> and <100> crystal directions and it leads to a global tilt of the grating facets (see Chapter 2). Although finite, the anisotropy ratio is large (~60) and nearly constant, leading to groove facets that are smooth, flat, and parallel to each other. If the anisotropy is known in advance, one should account for this at the orientation step in the processing. Absolute control of the blaze angle is particularly important at low orders for properly setting the blaze wavelength, as can be seen from Eq. 4.3. Of course, uniformity of the blaze across the grating is important for any optical application.

To evaluate the transmission performance of these grisms, we illuminate them using a collimated beam of λ=1523 nm laser light and then focus the diffracted beams onto an InGaAs focal plane array. The beam diameter is limited to 10 mm by our test equipment. By suitable choices of the camera focal ratio, we can obtain a point spread function (PSF) by measuring the shape of a single diffraction order (Figure 4.9), or we can estimate the device throughput by imaging a series of adjacent orders (Figure 4.10). Figure 4.9 shows the normalized one-dimensional PSF of grism G3. As shown, the shape and width of the diffraction spots are virtually identical to those obtained for a flat mirror and agree with the theoretical curve for a circular aperture, verifying diffraction-limited performance over the beam aperture. Before normalizing the PSFs, the peak value of the grism PSF is 48% of that measured for the mirror, consistent with the Fresnel losses at the two air-silicon interfaces (T=49% for n=3.4). Figure 4.10 shows transmission spectra for grisms G3, G4, and G5. These data were obtained using the same beam (10 mm diameter, λ=1523 nm) as for Figure 4.9, but the camera optics are faster and the field-of-view correspondingly greater. Each of the spectra in Figure 4.10 consists of a series of orders, because the laser wavelength is not on the blaze for these grisms. Between orders, no ghosts are visible. By summing up thepower in the series of orders, we measure the efficiencies listed in Table 4.3. The raw transmission is simply the ratio of power in the observed diffraction orders to the power incident on the entrance face, and should be nearly equal to the efficiency on the blaze. Since the grisms are not yet equipped with anti-reflection coatings, the raw transmission cannot exceed the value permitted by index mismatch (49%). The relative transmission efficiency values include corrections for the Fresnel losses and geometric losses due to the groove top (see Chapter 2). The remaining power is almost certainly scattered, since absorption is expected to be negligible for the substrate thicknesses (less than 2 cm) at λ=1523 nm. As the efficiencies are 75-90% of

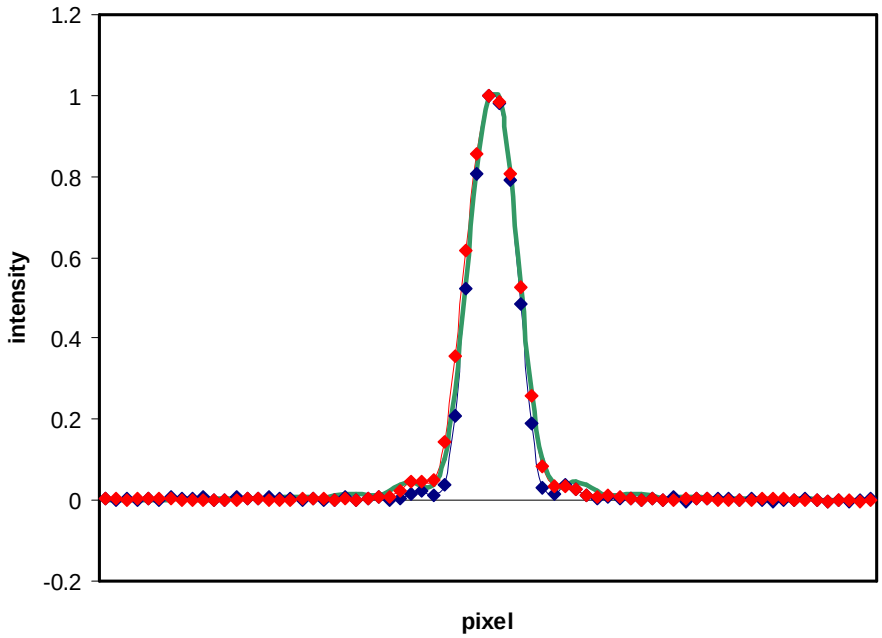

Figure 4.9. Normalized one-dimensional PSF taken in transmission using a 10 mm diameter beam with λ=1523 nm. Red points show the PSF measured for grism G3, and is a magnification of the brightest diffraction order shown in the first plot of Figure 4.10, below. The horizontal axis is the dispersion direction. Blue points show the corresponding data taken from a reference mirror. Both the data from the grism and the mirror nearly coincide with the theoretical curve (green) calculated for a circular aperture, indicating diffraction-limited performance. Before normalizing, the peak value of the grism PSF was 48% of that measured for the mirror PSF, as expected for nearly perfect transmission through two uncoated Si surfaces.

the theoretical maximums permitted by geometric and index mismatch limitations, this indicates that the grisms are of excellent optical quality.

This picture is strengthened by external reflection measurements using HeNe lasers at green (543.5 nm), red (632.8 nm), and near-infrared (1523 nm) light. In Figure 4.11 we show reflection spectra taken using a collimated 25 mm beam from a green HeNe laser with λ=543.5 nm. Since this wavelength is not on the blaze for any of the grisms shown, the incident beam is diffracted into multiple orders. As before, no diffraction ghosts are visible between the orders. By summing up the power in the series of orders, we can obtain an estimate of the on-blaze efficiency (see Chapter 2). For the three spectra in Figure 4.10, these reflection efficiencies range from 70-90% of the theoretical maximum permitted by geometry (see Figure 4.5) and the silicon refractive index. The relative reflection efficiencies are close to the relative transmission efficiencies, indicating that reflection tests in the visible may be used as surrogate measurements to assess the quality of the grating without requiring a transmission measurement in the infrared. This is reasonable since the two measurements have comparable effective wavelengths and place roughly the same demands on the phase accuracy of the grating surface.

Grism G3 is intended to be used at moderate orders (m=14-23). We may estimate the device throughput at the blaze wavelength by starting from the efficiency measured in high order and accounting for what transmission can be expected for a suitable commercial anti-reflection coating. Assuming a single-pass coating transmission of 95%, we estimate that G3 has an end-to-end throughput of (0.95)2(0.25)/(0.49) = 46%. Somewhat higher throughput values are expected for grisms G4 and G5 because their geometric losses will be approximately one-third of that for G3. To estimate the throughput accurately for G4 and G5 at their blaze wavelengths requires a detailed

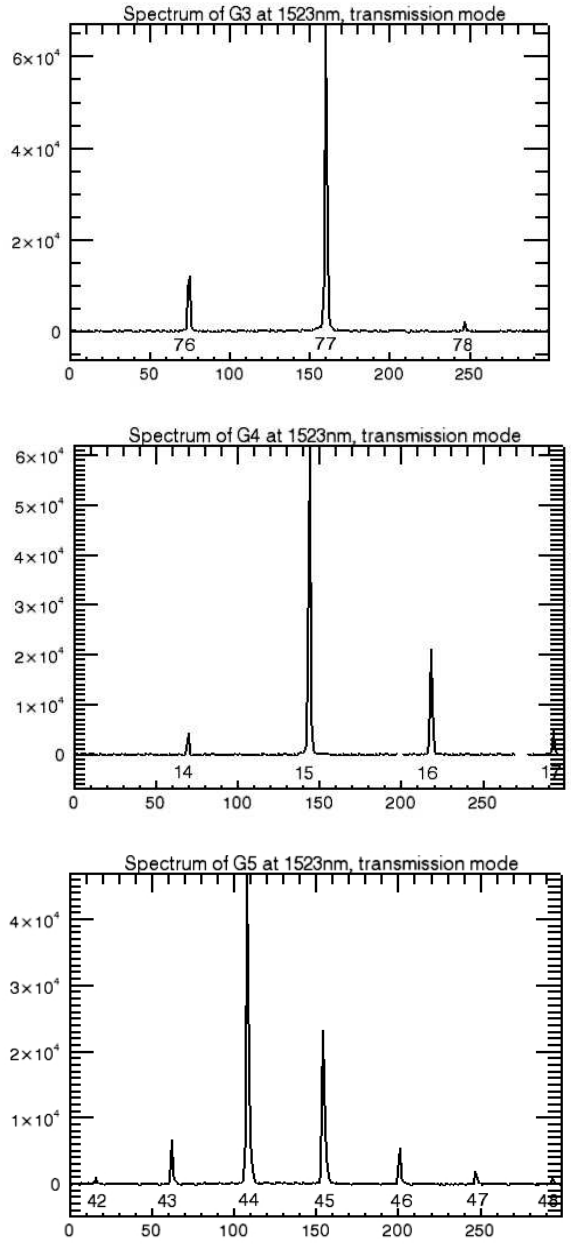

Figure 4.10. Transmission spectra of grisms G3 (*top*), G4 (*center*), and G5 (*bottom*), taken using a 10 mm diameter collimated beam with λ=1523 nm. Order numbers are indicated near the bottom of each peak.

Table 4.3. Efficiencies for the three grisms whose transmission spectra are shown in Figure 4.10. The raw *T* measures the ratio of transmitted to incident light at λ=1523 nm. The relative *T* corrects for expected Fresnel (the grisms are uncoated) and geometric (see Figures 4.1 and 4.5) losses and reflects the overall quality of the fabricated gratings. The values >100% are consistent with efficiencies ~100% in the transmission mode (our estimated systematic errors were 10-15%). The relative *R* is measured using reflected light at λ=543.5 nm (Figure 4.11), corrected for Fresnel and geometric losses. For details about the correction calculations, see Chapter 2.

Grism	**Order *m* at 1523 nm**	**Raw *T* (%) (1523 nm)**	**Relative *T* (%) (1523 nm)**	**Relative *R* (%) (543.5 nm)**	**Relative *T* (%) predicted from *R***
G3	77	31	109	80	96
G4	15	44	104	78	95
G5	44	48	114	70	94

electromagnetic calculation, since these devices are designed for use in low orders. We have not done that in this paper.

Reflection measurements also provide the (external) surface error plot and the two-dimensional point spread function (PSF) shown in Figure 4.12. The surface plot is obtained using a Zygo interferometer by illuminating the grating in Littrow using collimated red HeNe light. As shown by the surface plot, the surface deviations are correlated into structures with spatial wavelengths approaching 10 mm or more. However, these deviations are small and the overall surface figure ($\Delta\sigma_{RMS}<10^{-2}$ waves RMS) is excellent. Clearly, we can expect excellent performance of these grisms at their design wavelengths (λ=1 to 40 µm).

4.6 APPLICATIONS

The silicon grisms whose performance is described in Section 5 were designed to equip FORCAST, a cryogenic mid-infrared (5-40 µm) camera operating at liquid helium temperatures (4 K) with medium resolution spectroscopic capability (Keller et al. 2000, Keller et al. 2003). All four of the gratings have been fabricated successfully and demonstrate optical performance at a level at which we can expect diffraction-limited performance over the 22 mm collimated beam of the instrument. Three of the four grating blanks have been successfully shaped into grisms, while the fourth was not cut according to specification and will have to be remade. To finish these devices requires the application of suitable broadband antireflection coatings to the entrance and grating faces of each grism. This is challenging for the mid-infrared bands (17.1-28.1 µm and 28.6-37.4 µm) where the choice of available coating materials is limited and some development work will be necessary. Initial development is encouraging, though, and a suitable coating has already been developed for the 4.9 - 8.1 µm wavelength range. This

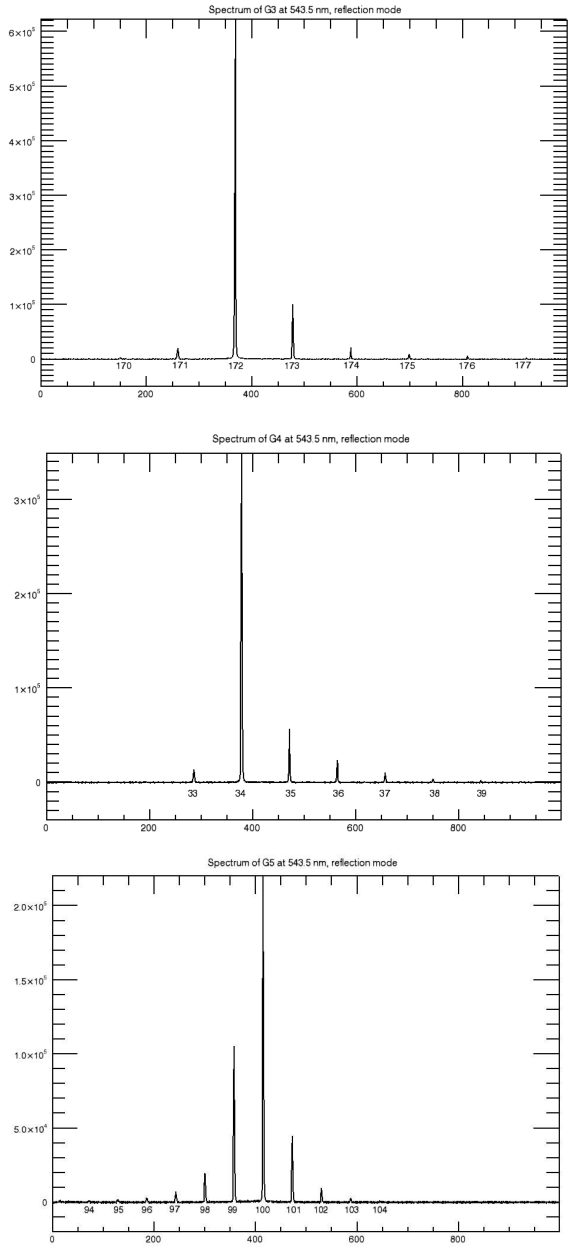

Figure 4.11. Reflection spectra of grisms G3 (top), G4 (middle), and G5 (bottom), taken using a 23 mm (G3) or 25 mm (G4, G5) diameter collimated beam with λ=543.5 nm. Order numbers are indicated near the bottom of each peak. The panels correspond to those in Figure 4.10.

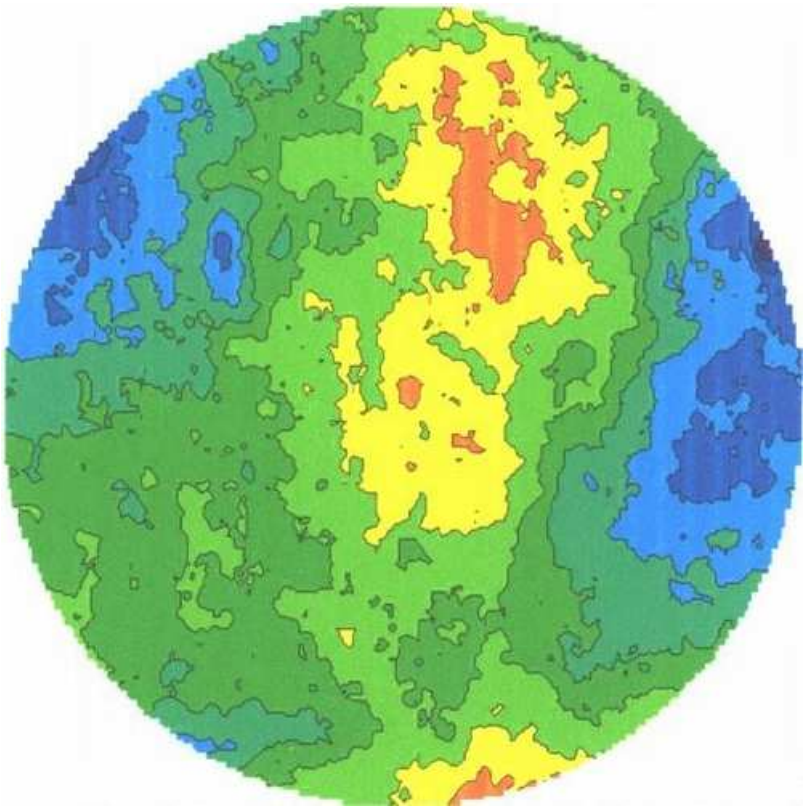

Figure 4.12. Surface error plot of grism G2 (σ=25 μm and δ=6.16°), as obtained from front-surface reflectivity measurements using λ=632.8 nm laser light. Each color contour represents approximately 1/150 of a wave. The RMS deviation over the indicated 25 mm diameter aperture is approximately 10^{-2} waves, although the actual surface variations are not completely uncorrelated.

coating can be applied to Si grating facets with good uniformity, is mechanically robust, can survive multiple rapid thermal cycles between 300 K and 77 K, and raises the single-interface transmission from ~70% to better than 92% over this region.

Grism G5 (δ=6.16º, σ=87 µm, right grism in center panel of Figure 4.4) is uncoated, but has been installed into FORCAST to assess its performance when installed into a cryogenic environment. An early spectrum taken with this grism is shown in Figure 4.13. Line fits to some of the deep absorption lines between 19 and 27 µm yield a resolution $\lambda/\Delta\lambda \approx 150$, limited by the slit. This verifies that the grism resolution is at least as great as this value.

These large, coarsely-ruled silicon grisms can be combined in cross-dispersed configurations to provide moderate resolution spectroscopy in the near-IR using all-transmissive optics. For example, the cross-dispersed configuration (G3×G2) in FORCAST, provides a resolution of R=1200 with a coverage from 4.9 to 8.1 µm in a single exposure.

These grisms are developed in conjunction with silicon immersion gratings (see Chapter 2), which require deeply blazed gratings and consequently thicker blanks. The optical tolerances on the groove placement are more stringent in the case of immersion gratings, and we have developed methods that are compatible with production of both immersion and transmission devices. As a benefit, the optical performance for the grisms shown here exceeds what is required for applications.

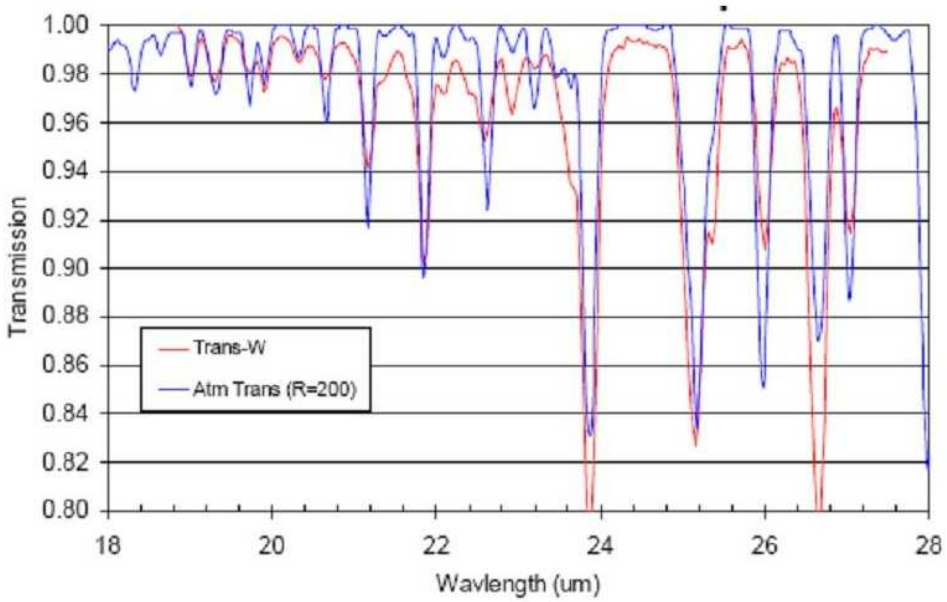

Figure 4.13. Grism lab transmission spectrum (red) for a 2.9 pixel slit showing water absorption lines taken using grism G5 (see center panel of Figure 4.4). Shown in blue is an ATRAN calculation for atmospheric transmission expected from SOFIA for 7.3 µm of precipitable water vapor and 45^{o} from zenith at a spectral resolution of 200. The measurement resolution is limited by the slit.

Chapter 5.

Future Developments

The next generation of silicon diffractive optics will require substrates larger than the current state of art. As we move toward larger substrates, we will need to change some steps in our process and replace a few pieces of equipment. We outline here several key improvements and changes to the process that will need to take place in the near future.

Our current process is limited to boules up to 4" in diameter and disks up to 1.5" thick. The current substrate sizes and the manufacturing equipment are adequate for the current generation of immersion gratings (e.g. ImGES grating G1) but they will be unable to accommodate larger grating sizes. The Giant Magellan Telescope (GMT) proposal calls for a near-IR high resolution spectrograph with R~100,000. This goal can be accomplished with an R3 immersion echelle with the beam diameter of 83 mm and diffraction limited resolving power of 860,000 at 2 μm (Jaffe et al. 2006). In order to make a grating with grooves that cover a grating of length of 300 mm, we will need substrates at least 12” in diameter and 3.5” thick. Our spin table and UV exposure equipment will need to be replaced or upgraded for bigger substrates. Photolithography masks also become an issue. While masks can be procured in larger sizes (7”×7”) their thickness is only 0.125” and therefore their flatness becomes a much bigger issue. An alternative approach is a direct method for writing the pattern onto the photoresist coated substrate using a custom laser system. Prototypes of such systems are still being built and tested but none are available for testing currently. However, if we were able to

successfully use one of these direct writing systems, their advantage over the contact mask method we currently use would be clear – we would eliminate all errors due to photolithography masks (transfer errors from the mask to the passivation layer, errors due to masks warping due to thin masks, and the errors due to possibly non-flat mask substrates used for photolithography masks).

The method of photoresist deposition would also change for large substrates from the spin-on method currently used to vapor deposition which yields better results (more uniform photoresist layer with smaller number of defects). Currently, the grating performance is limited by the periodic errors in our gratings which we attribute to the imperfect photoresist deposition and mask contact. The resulting photoresist layer has very good quality in the middle but, at the substrate edge, it accumulates producing a raised area around the rim in some places. Subsequently, the mask contact with photoresist is not perfect and the mask tilt is responsible for the periodicity of groove spacing error tilted relative to both the spectral and spatial planes. We modeled errors present in the G1 wave front at 632.8 nm using a combination of a random groove displacement error (ε_{RMS}=11 nm/sin δ=12.3 nm) and a periodic error with P=5.5 mm and A=28 nm (both estimates from the direct Zygo determination and from IR PSF measurements agree – see Section 2.3.4.3). This combination yields an RMS wave front error of 25.7 nm or an RMS wave front error of 25.7 nm$\times$sin δ=23 nm. The estimated RMS wave front error is smaller than the total RMS wave front error observed in Figure 2.16 for G1 (32 nm) but it gives us an estimate of how much we could improve our grating performance. The wave front error of our gratings is clearly dominated by the periodic error, and now that we have the experience with using photolithographic masks on thick substrates, we will be able to eliminate the periodic errors from our gratings. The improvement we could achieve by eliminating masks in our process would be

considerable if we eliminated ghosts from our gratings. Our measured RMS error would drop from 32 nm (λ/20) to 11 nm (λ/57) or better if we improve our control over the photoresist deposition and pattern writing. The scattered light in grass of our most recent grating G3 (see Figure 2.17) is comparable to a commercially produced R2 echelle used in the 2d coudé spectrograph on the 2.7 m telescope at the McDonald Observatory (Tull et al. 1995).

Current RIE systems at J.J. Pickle Center are limited by the depth of the chamber, i.e. the distance between two electrodes positioned at the top and the bottom of the chamber. With our 1.5" high substrates, we are nearing the top electrode and compromising the directionality of the plasma inside the chamber. Decreased directionality causes some side etching into the areas masked by the photoresist and the thinning of the nitride lines. This thinning does not necessarily occur uniformly over the whole area of the substrate and represents a concern for even larger and thicker substrates. We are already looking into purchasing an RIE system with a taller chamber which will be altered to accommodate substrates up to 2" thick. This will substantially improve anisotropy of the silicon nitride etch and yield more vertical walls in the silicon nitride etch mask. The resulting pattern will be more uniform across the whole area of the substrate.

Temperature control has not been much of a problem to date since substrates have not exceeded 0.5 kg in weight. However, future substrates will cross the 1 kg limit and, even though silicon has a very high thermal conductivity, the change in the temperature of the bath when a large piece of silicon at room temperature is submerged will be large. As an example, we calculated the temperature of our standard KOH bath after a silicon disk 262 mm in diameter and 74 mm high (appropriate for an R3 echelle grating according to GMTNIRS requirements) was submersed in it. If we assume that the mass

of the KOH solution is the same as the mass of the disk, and that the disk is at room temperature while the KOH bath is at 70°C, we find that the bath temperature will drop to 62°C. Since the etch rate of the (100) silicon plane peaks between 60 - 70°C, the rate change is not very steep but it is significant. To prevent large temperature changes during the etching process and minimize the temperature effects on etch rates, we will need to preheat the substrates to temperatures closer to 68°C and include stirring in our bath.

In order to move on to the next generation of silicon diffractive optics, we will need to make extensive changes to our processing equipment and even use new technologies which are not yet available or fully tested. Our knowledge of the grating production process has steadily been improving over the last 15 years and we are confident that we can continue to make use of the advances in the silicon processing technology to make gratings on very large substrates.

Appendix A

Directing stray light in an immersion grating

When deciding on the final shape of the silicon prism, we have two tilted surfaces to consider: the entrance face and the bottom (unused) size of the prism. Here we discuss each surface separately and ways to decrease the amount of stray light due to the immersion grating in a cross-dispersed spectrograph. We work out the example of the grating G1.

A.1 ENTRANCE FACE TILT

The reflectance of silicon in the near-IR is 30% at normal incidence. Therefore, it is necessary to coat the entrance face of a silicon immersion grating with an anti-reflective coating to prevent large losses due to two reflective light losses at the entrance face (the first time is when the light goes in and the second time is when the light comes out). While commercially available AR coatings for silicon have excellent performance, they are still imperfect, and we can expect some small fraction of light (typically ~1%) to be reflected back. For an echelle grating with the entrance face parallel to the groove surfaces, the light reflected back from the AR coated entrance face will be dispersed by the cross-disperser and will be seen as a bright stripe on the detector. Even though the amount of light reflected back is only a few percent, as it is dispersed by the cross-disperser alone, its intensity on the detector will be much larger than the light dispersed by both gratings. To remedy this problem, we must tilt the entrance face of our immersion echelles in the cross-dispersion direction thereby making a quasi-Littrow

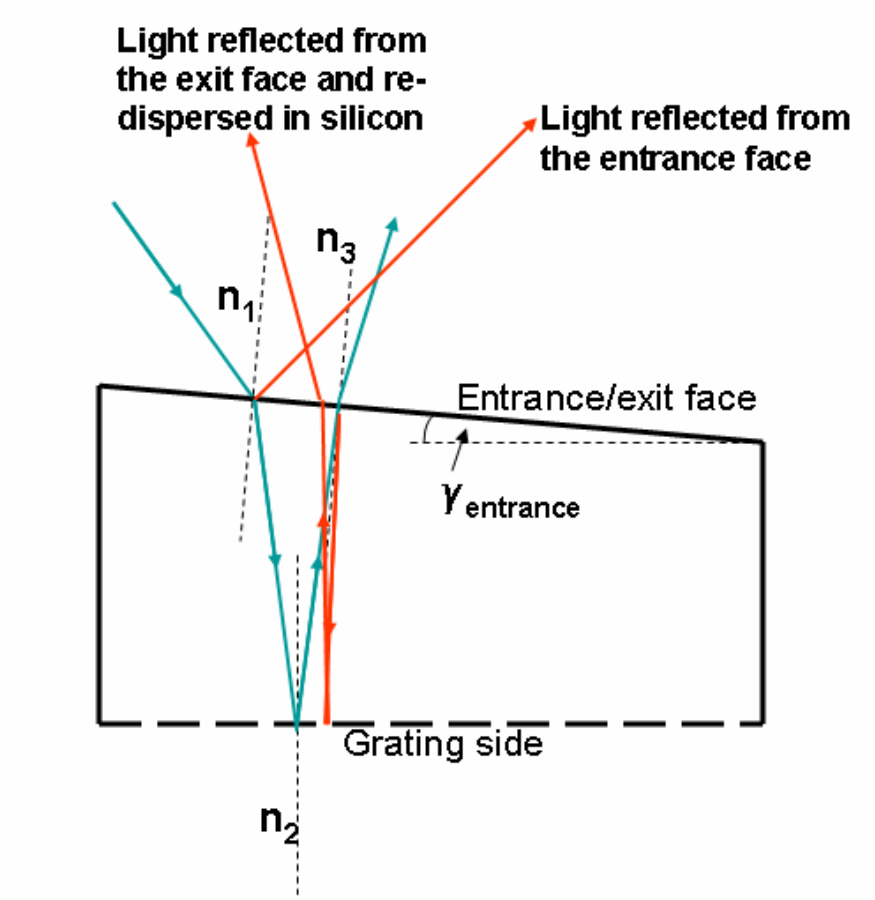

Figure A.1. View from top demonstrating the effect of tilting the entrance face. Blue arrows are used to mark the path of diffracted light and red arrows mark the path of reflected light.

setup. The modified grating equation accounting for the non-normal grating incidence inside silicon is:

$$m\lambda = \sigma n(\sin\alpha + \sin\beta)\cos\gamma \qquad \text{(A.1)}$$

If we are only redirecting the reflection from the AR coated entrance face, we will need to tilt the entrance face by some angle $\gamma_{entrance}$ which can be estimated using the following calculation (illustration is given in Figure A.1 and the calculation uses the same notation). We assume parameters given in the ImGES proposal for the array and camera lens and use G1 as the grating. For a 2048×2048 array, 18 μm pixels, total length of the chip=36.9 mm, offset length=total length of the array/2=18.4 mm. Focal length of the camera is f_{camera} =320 mm. At each of the normals, n_1, n_2 and n_3, to the entrance face or grating surface (see Figure A.1), we have three beams to consider: incident, reflected, and refracted. Below is the summary of the most important ones for our calculation:

Incidence angle at n_1 : $\gamma_{incident}$

Refracted angle at n_1 : $\sin\gamma_{incident} = 3.45 \sin\gamma_{Si,1}$

Incidence and reflection angle at n_2 : $\gamma_{Si,2} = \gamma_{Si,1} - \gamma_{entrance}$

Incidence angle at n_3 : $\gamma_{Si,3} = \gamma_{Si,2} - \gamma_{entrance} = \gamma_{Si,1} - 2\gamma_{entrance}$

Refracted angle at n_3 : $3.45 \sin\gamma_{Si,3} = \sin\gamma_{diffracted}$

For $\gamma_{Si,2} > \gamma_{entrance}$, the total beam displacement is $\gamma_{incident} + \gamma_{diffracted}$ and the incident beam reflection will be offset from the diffracted beam by $\gamma_{incident} - \gamma_{diffracted}$. For $\gamma_{Si,2} < \gamma_{entrance}$, the total beam displacement is $\gamma_{incident} - |\gamma_{diffracted}|$ and the incident beam reflection will be offset from the diffracted beam by $\gamma_{incident} - |\gamma_{diffracted}|$. If we wanted a grating in the

Littrow mount (inside silicon), then we need to set $\gamma_{Si,2}$=0. If we also choose the entrance face tilt of $\gamma_{entrance}$=1°, then $\gamma_{Si,1}=\gamma_{entrance}$=1° and $\gamma_{incident}$=3.45°. The diffracted beam is parallel to the incident beam but offset from it. If we, however, allow $\gamma_{Si,2}$=1° (i.e. the grating is now in the quasi-Littrow mount), the blaze is shifted by 5Å, then $\gamma_{incident}$=6.87° and $\gamma_{diffracted}$=0°. The total offset between the incident and diffracted beams is 6.87° or f_{camera}*angular beam displacement=38.4 mm. The incident beam reflection from the entrance face will be displaced by 2×6.87° from the incident beam and 6.87° from the diffracted beam. This displacement is sufficient to ensure that the unwanted reflection is moved in the cross-dispersion direction so that it doesn't hit the array.

Now we need to examine what happens to the diffracted beam inside silicon that hits the entrance face on the way out (see Figure A.2). The light in this beam will have the incidence angle at n_2 of $\gamma_{Si,3}=\gamma_{Si,2}-\gamma_{entrance}=\gamma_{Si,1}-2\gamma_{entrance}$ in the cross-dispersion direction and a range of angles in the dispersion direction given by 90°-(α-β) where β is given by the grating equation. Upon reflection from the exit face, this light will be re-dispersed by the grating with the new (β,γ) coordinates. We only consider the first reflection here. After the light hits the grating with (63.4°,$\gamma_{Si,2}$) the first time, the diffracted light will have coordinates (β,$\gamma_{Si,2}$), and the reflected beam incident on the grating for the second time will have coordinates (α+(α-β),$\gamma_{Si,2}$-2$\gamma_{entrance}$). So, for our previous example ($\gamma_{entrance}$=1°, $\gamma_{Si,2}$=1°), the light will simply retrace the path of the incident beam in the cross-dispersion direction. For different tilts, we will need to calculate all the dispersion angles for the light reflected inside the dielectric. However, we can estimate that the intensity of redispersed light will be 1-*T*, where *T* is the transmissivity of the AR coating, of the light in the observed spectrum at each wavelength but displaced from it in one or both directions.

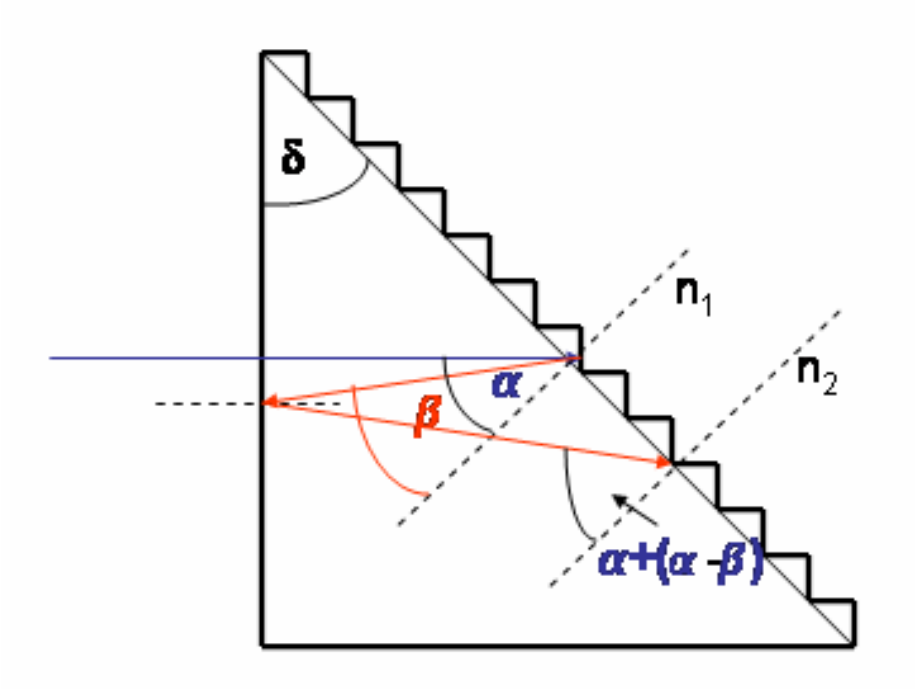

Figure A.2. View from the side. The light marked with red arrows is reflected from the exit face and re-dispersed by the grating.

A.2 BOTTOM TILT

Stray light can come from the light partially reflected from the bottom side of the prism (see Figure A.3). This light will be refracted in the dispersion direction, and depending on the exact grating and spectrograph geometry, may end up on the detector.

We denote the angle at which diffracted light hits the bottom edge of the entrance face with $\beta_{critical}$. For all $\beta<\beta_{critical}$, the light diffracted at the angle β will hit the bottom of the prism. To calculate the critical angle for G1, we use the following parameters:

Entrance face = 25mm

Beam size = 22mm (diameter)

$\delta = 63.4°$

Length of the bottom side of the prism = 49.9 mm

Grating length = 55.8 mm

The clearance on either size of the beam is 1.5 mm (marked green in Figure A.3). The angle ε is given by

$$\varepsilon = \arctan\frac{1.5}{x_1} = 1.83^{\circ} \quad \text{where} \quad x_1 = 23.5 * \tan 63.4^{\circ} \tag{A.2}$$

Light reflected from the bottom will be incident on the entrance face at the angle ε and refracted at the angle $3.45 \times \sin \varepsilon$. The range of ε for which light will be transmitted outside is $1.83^{o} < \varepsilon < \arcsin(1/n) = 16.85^{o}$. The corresponding range of angles β is then given by $46.56^{o} < \beta = \alpha - \varepsilon < 61.57^{o}$.

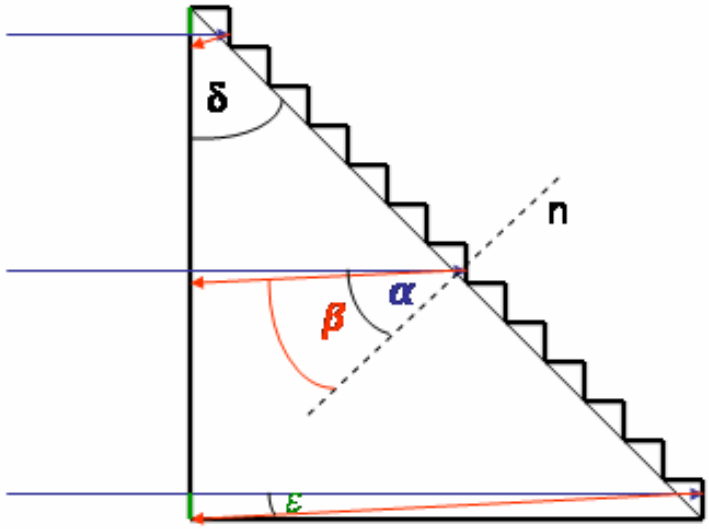

Figure A.3. Diagram showing the critical angle at which a fraction of diffracted light starts to hit the bottom of the prism.

To estimate the intensity of stray light, we must explore the intensity profile of a single groove in order to determine the intensity of diffracted light, $I(\beta)/I_0$, at the range of angles $46.56^o < \beta < 61.57^o$. The normalized intensity profile is given by:

$$\frac{I(\beta)}{I_0} = \left[\frac{\sin \frac{ksp}{2}}{\frac{ksp}{2}} \right]^2 \tag{A.3}$$

where $k = 2\pi n / \lambda$ (in silicon), $p = \sin\beta - \sin\alpha$. The effective groove width, s, is determined by the groove geometry (illustrated in Figure A.4). For G1, s=35.8 μm. The partial blaze function for G1 is shown in Figure A.5 for the 140th order (λ_{blaze}=3.5 μm). Throughout the discussion here we assume that the incident light is white, i.e. that it fills the blaze function shown in Figure A.5. To estimate the fraction of reflected light from the bottom surface, we correct the intensity profile by multiplying by the fractional area of a circular beam given in Figure A.6. Figure A.7 illustrates the product of fractional area and the intensity profile. The stray light contribution resulting from the light hitting the bottom of the prism is on the order of <0.1% in any given direction. The total integrated scattered light in the transmitted range, $46.56^o<\beta<61.57^o$, is 2%. However, the range of angles used in this calculation well exceeds the range of angles within which the light will land on the array and it will depend on the spectrograph geometry. We can further influence where this light goes by tilting the bottom side of the prism. In Figure A.8, we show two suggested cuts. In the first case (see Figure A.8, *left*), we have effectively changed the γ angle of the outgoing light by ϕ_{tilt}. In the second case, we have effectively changed the β angle of the diffracted beam hitting the bottom surface. We have chosen the first cut because it allowed us to steer all the stray light completely

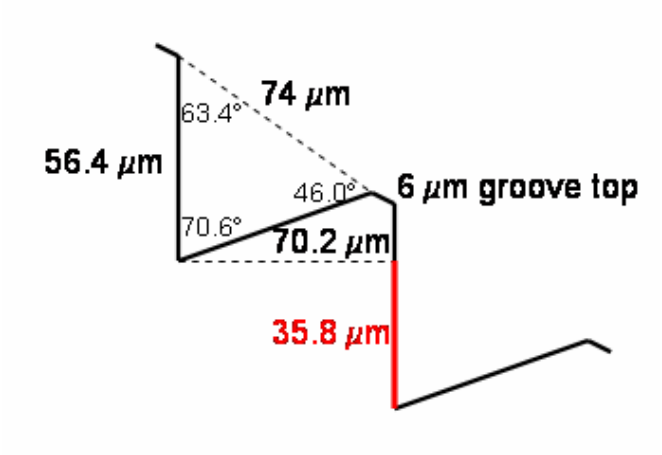

Figure A.4. Groove geometry. The effective groove width is highlighted in red.

outside of the beam and it only required a single cut. The second case would require an additional cut to produce the V-shaped bottom.

In conclusion, the two sources of stray light caused by the grating geometry and finite reflectance of the AR coating do not seem to contribute more than a total of a few percent to the scattered light caused by groove surface roughness and other “normal” defects in gratings. We can also remove even that very small contribution by cleverly orienting the entrance face as well as the bottom of our immersion grating.

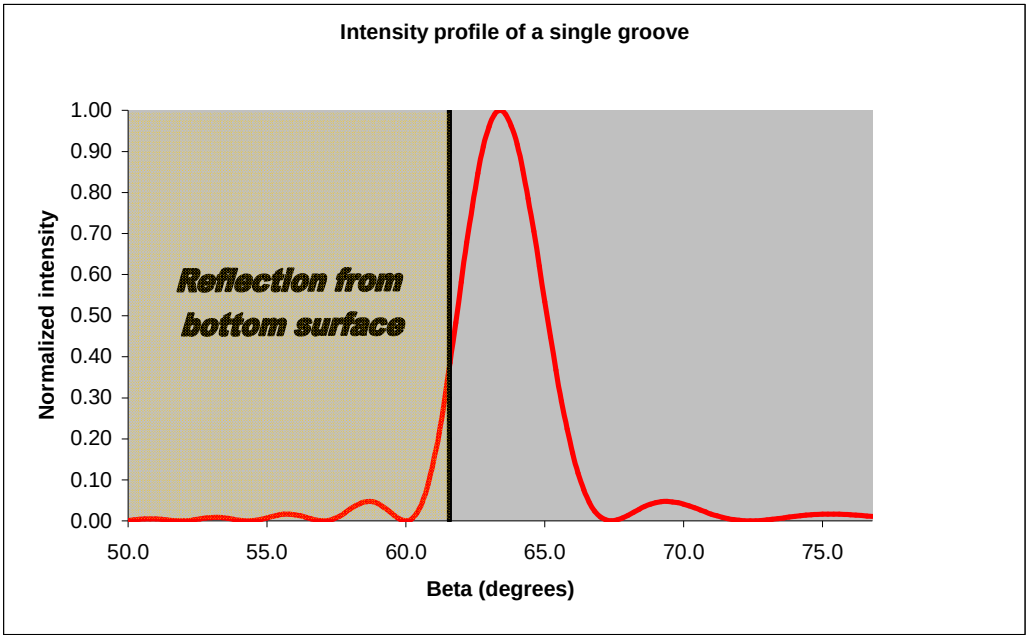

Figure A.5. Intensity profile of a single groove inside silicon normalized to 1.0. The x-axis is the diffracted angle, β.

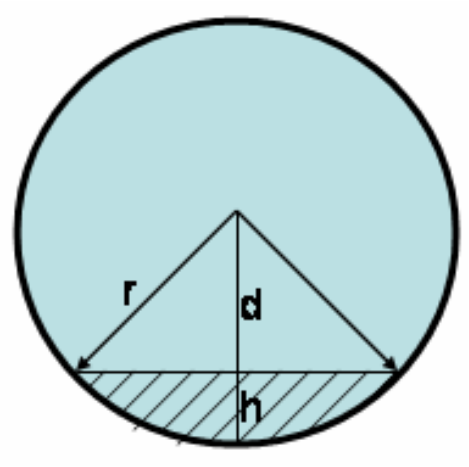

$$r = h + d$$

$$\text{Area} = r^2 \arccos\frac{r-h}{r} - (r-h)\sqrt{2rh-h^2}$$

where $h = x_1 \tan(\alpha - \beta) - 1.5$

$$\text{Fractional area} = \frac{\text{Area}}{\pi r^2}$$

Figure A.6. The shaded area of the circle is the fractional area of the beam hitting the bottom of the prism.

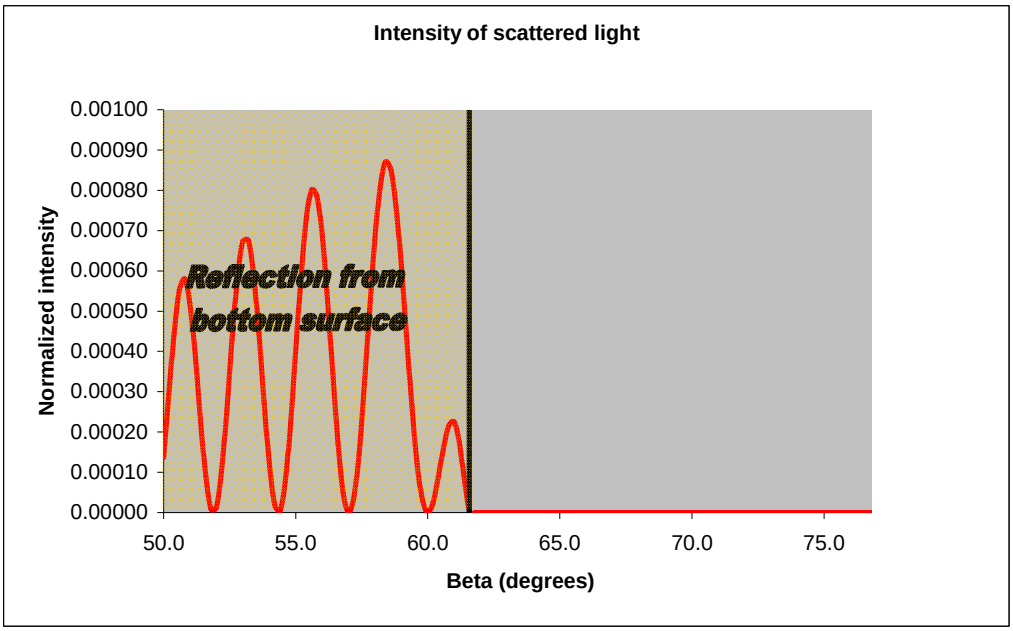

Figure A.7. Intensity of scattered light as a function of angle of diffraction (in silicon).

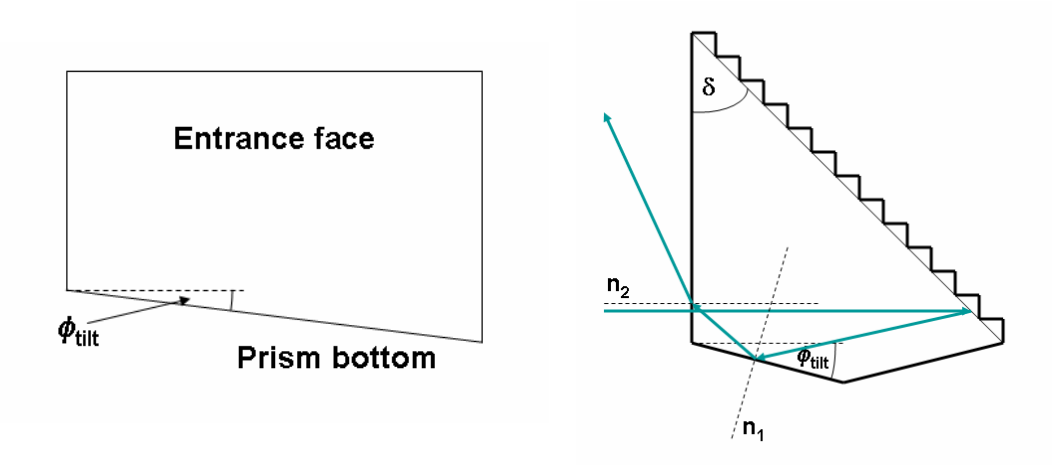

Figure A.8. *Left*: First suggested cut which effectively changes the γ angle of outgoing light. *Right*: Second suggested cut which effectively changes the β angle of outgoing light.

Bibliography

Bassous E. “Fabrication of novel three-dimensional microstructures by the anisotropic etching of (100) and (110) silicon.” *IEEE Transactions on Electron Devices* ED-25 (1978): 1178-1185.

Baum, T. and Schiffrin, D. J. “AFM study of surface finish improvements by ultrasound in the anisotropic etching of Si<100> in KOH for micromachining applications.” *J. Micromech. Microeng.* 7 (1997): 338-342.

Bennett, J. M. and Mattsson, L. *Introduction to Surface Roughness and Scattering*. Washington: Optical Society of America, 1999.

Born, M. and Wolf, E. Principles *of Optics. Cambridge*: Cambridge University Press, 1997.

Campbell, S. A., Cooper, K., Dixon, L., Earwaker, R., Port, S. N., and Schiffrin, D. J. “Inhibition of pyramid formation in the etching of Si p(100) in aqueous potassium hydroxide-isopropanol.” *J. Micromech. Microeng.* 5 (1995): 209-218.

Carl Zeiss, "Grating Catalog", available at http://www.zeiss.de, 2004.

Collins, R. J. and Fan, H. Y. "Infrared Lattice Absorption Bands in Germanium, Silicon, and Diamond." *Phys. Rev.* 93 (1954): 674-678.

Dash, W. C. and Newman, R. "Intrinsic optical absorption in single-crystal germanium and silicon at 77K and 300K." *Phys. Rev.* 99 (1955): 1151-1155.

Davies, M. A., Evans, C. J., Patterson, S. R., Vohra, R., and Bergner, B. C. "Application of precision diamond machining to the manufacture of micro-photonics components." In *Lithographic and Micromachining Techniques for Optical Component Fabrication II: Proc. SPIE Vol. 5183*, edited by Ernst-Bernhard Kley and Hans Peter Herzig, 94-106, 2003.

Deutsch, L. K., Hora, J. L., Adams, J. D., and Kassis, M. "MIRSI: a Mid-InfraRed Spectrometer and Imager." In *Instrument Design and Performance for Optical/Infrared Ground-based Telescopes: Proc. SPIE Vol. 4841*, edited by Masanori Iye and Alan F. Moorwood, 106-116, 2003.

Ebizuka, N., Iye, M., and Sasaki, T. "Optically anisotropic crystalline grisms for astronomical spectrographs." *Appl. Opt.* 37 (1998): 1236-1242.

Ershov, O. A., Jaffe, D. T., Marsh, J. P., and Keller, L. D. "Production of high-order micromachined silicon echelles on optically flat substrates." In *Lithographic and Micromachining Techniques for Optical Component Fabrication: Proc. SPIE Vol. 4440,* edited by Ernst-Bernhard Kley and Hans Peter Herzig. 301-308, 2001.

Ershov, O. A., Marsh, J. P., Allers, K. N., and Jaffe, D. T. "Infrared Grisms Using Anisotropic Etching of Silicon to Produce a Highly Asymmetric Groove Profile." In *IR Space Telescopes and Instruments: Proc. SPIE Vol. 4850,* edited by John C. Mather, 805-812, 2003.

Fan, H. Y. and Becker, M. "Infra-Red Absorption of Silicon." *Phys. Rev.* 78 (1950): 178.

Findler, G., Muchow, J., Koch, M., and Münzel, H. "Temporal evolution of silicon surface roughness during anisotropic etching processes." In *Proceeding of IEEE Conference on Micro Electro Mechanical Systems '92*, 62-66. Held in Travemünde, Germany, 1992.

Fraunhofer, J. von. "Neue Modifikation des Lichtes durch gegenseitige Einwirkung und Beugung der Strahlen, und Gesetze derselben." *Denkschriften der königlichen Akademie der Wissenschaften zu München*. 1821-1822, 8 (1822): 1-76. Published in Joseph von Fraunhofer's *Gesammelte schriften. Im auftrage der mathematisch-physikalischen Classe der Königlich Bayerischen Akademie der München*, 1888.

Freudling, W. "The NICMOS Grism Mode." In *The 1997 HST Calibration Workshop with a new generation of instruments: STScI Proc.*, edited by S. Casertano, R. Jedrzejewski, C. D. Keyes, and M. Stevens, 207-216. Baltimore: Space Telescope Science Institute, 1997.

Fujii, Y., Aoyama, K.-I., and Minowa, J.-I. "Optical demultiplexer using a silicon echellete grating." *IEEE Journal of Quantum Electronics* QE-16 (1980): 165-169.

Graf, U. U., Jaffe, D. T., Kim E. J., Lacy, J. H., Ling, H., Moore, J. T., and Rebeiz, G. "Fabrication and evaluation of an etched infrared diffraction grating." *Appl. Opt.* 33 (1994): 96-102.

Ge, J., McDavitt, D. L., Miller, S., Bernecker, J. L., Chakraborty, A., and Wang, J. "Breakthroughs in silicon grism and immersion grating technology at Penn State." In *Instrument Design and Performance for Optical/Infrared Ground-based Telescopes: Proc. SPIE Vol. 4841,* edited by Masanori Iye and Alan F. Moorwood, 1006-1015, 2003.

Greene, T. P., Tokunaga, A. T., Toomey, D. W., and Carr, J. S. "CSHELL: A High Spectral Resolution 1-5 μm Cryogenic Echelle Spectrograph for the IRTF." In *Infrared Detectors and Instrumentation: Proc. SPIE Vol. 1946*, edited by Albert M. Fowler, 313-324, 1993.

Grenon B. J., Defibaugh, D. C., Sprout D. M., and Taft C. J. “Manufacturing performance of the ALTA 3000 mask laser writer.” In *15th Annual BACUS Symposium on Photomask Technology and Management: Proc. SPIE Vol. 2621*, edited by Gilbert V. Shelden, 14-18, 1995.

Hein, A., Dorsch, O., and Obermeier, E. "Effects of metallic impurities on anisotropic etching of silicon in aqueous KOH-solutions." In *Transducers ’97: Proceedings of International Conference on Solid-State Sensors and Actuators Chicago*, 687-690, 1997.

Hinkle, K. H., Cuberly, R., Gaughan, N., Heynssens, J., Joyce, R. R. Ridgway, S. T., Schmitt, P., and Simmons, J. E. "Phoenix: A Cryogenic High-Resolution 1-5 micron Infrared Spectrograph." In *Infrared Astronomical Instrumentation: Proc. SPIE Vol. 3354*, edited by Alfred M. Fowler, 810-821, 1998.

Hinkle, H. H., Drake, R., and Ellis, T. A. “Cryogenic single-crystal silicon optics.” In *Instrumentation in Astronomy VIIIL Proc. SPIE Vol. 2198*, edited by David L. Crawford and Eric R. Craine, 516-524, 1994.

Hrostowski, H. J. and Kaiser, R. H. "Infrared Absoprtion of Oxygen in Silicon." *Phys. Rev.* 107 (1957): 966-972.

Hulthén, E. and Neuhaus, H. "Diffraction gratings in immersion." *Nature* 173 (1954): 442-443.

Jaffe, D. T., Keller, L. D., and Ershov, O. A. "Micromachined silicon diffraction gratings for infrared spectroscopy." In *Infrared Astronomical Instrumentation: Proc. SPIE Vol. 3354*, edited by Alfred M. Fowler, 201-212, 1998.

Jaffe, D., Mar, D., and Segura, P. *Conceptual design for a high resolution near-IR spectrograph for the Giant Magellan Telescope*, 2006.

Kaiser, W., Keck, P. H., and Lange, C. F. "Infrared Absorption and Oxygen Content in Silicon and Germanium." *Phys. Rev.* 101 (1956): 1264-1268.

Kane, S. and Squier, J. "Grism-pair stretcher-compressor system for simultaneous second- and third-order dispersion compensation in chirped pulse amplification." *J. Opt. Sci. Am. B* 14 (1997): 661-665.

Käufl, H. U., Kühl, K., and Vogel, S. "Grisms from germanium/silicon for astronomical instruments." In *Infrared Astronomical Instrumentation: Proc. SPIE Vol. 3354*, edited by Alfred M. Fowler, 151-158, 1998.

Keller, L. D., Jaffe, D. T., Ershov, O. A., Benedict, T., and Graf, U. U. "Fabrication and testing of chemically micromachined silicon echelle gratings." *Appl. Opt.* 39 (2000): 1094-1105.

Keller, L. D., Herter, T. L., Stacey, G. J., Gull, G. E., Pirger, B., Schoenwald, J., Bowmann, H., and Nikola, T. “FORCAST: a facility 5-40 micron camera for SOFIA.” In *Airborne Telescope Systems: Proc. SPIE Vol. 4014*, edited by Ramsey K. Melugin and Hans-Peter Roeser, 86-97, 2000.

Keller, L. D., Herter, T. L., Stacey, G. J., Gull, G. E., Schoenwald, J., Pirger, B., and Nikola, T. "FORCAST: the faint object infrared camera for the SOFIA telescope." In *Airborne Telescope Systems II: Proc. SPIE Vol. 4857*, edited by Ramsey K. Melugin and Hans-Peter Roeser, 29-36, 2003.

Kendall, D. L. "On etching very narrow grooves in silicon." *App. Phys. Let.* 26 (1975): 195-198.

Kendall, D. L. and Shoultz, R. “Wet Chemical Etching of Silicon and 10 Challenges for Micromachiners.” In *SPIE Handbook of Microfabrication, Micromachining, and Microlithography, Vol. 2.*, edited by P. Rai-Choudhury. SPIE Optical Press. 41-97, 1997.

Kobayashi, N., Tokunaga, A. T., Terada, H., Goto, M., Weber, M., Potter, R., Onaka, P. M., Ching, G. K., Young, T. T., Fletcher, K., Neil, D., Robertson, L., Cook, D., Imanishi, M., and Warren, D. W. "IRCS: infrared camera and spectrograph for the Subaru Telescope." In *Optical and IR Telescope Instrumentation and Detectors: Proc. SPIE Vol. 4008*, edited by Masanori Iye and Alan F. Moorwood, 1056-1066, 2000.

Kuzmenko, P. J. and Ciarlo, D. R. "Improving the optical performance of etched silicon gratings." In *Infrared Astronomical Instrumentation: Proc. SPIE Vol. 3354*, edited by Alfred M. Fowler, 357-367, 1998.

Kuzmenko, P. J., Ciarlo, D. R., and Stevens, C. G. "Fabrication and testing of a silicon immersion grating for infrared spectroscopy." In *Optical Spectroscopic Techniques and Instrumentation for Atmospheric and Space Research: Proc. SPIE Vol. 2266*, edited by Jinxue Wang and Paul B. Hays, 566-577, 1994.

Kuzmenko, P. J., Little, L. M., Davis, P. J., and Little, S. L. "Modeling, fabrication, and testing of a diamond-machined germanium immersion grating." In *IR Space Telescopes and Instruments: Proc. SPIE Vol. 4850*, edited by John C. Mather, 1179-1190, 2003.

Kwa, T. A., French, P. J., Wolffenbuttel, R. F., Sarro, P. M., Hellemans, L., and Snauwaert, J. "Anisotropically etched silicon mirrors for optical sensor applications." *J. Electrochem. Soc.* 142 (1995): 1226-1233.

Lagage, P. O., Pel, J. W., Authier, M., Belorgey, J., Claret, A., Doucet, C., Dubreuil, D., Durand, G., Elswijk, G. E., Giradot, P., Käufl, H. U., Kroes, G., Lortholary, M., Lussignol, Y., Marchesi, M., Pantin, E., Peletier, R., Pirard, J.-F., Pragt, J., Rio,

Y., Schoenmaker, T., Siebenmorgen, R., Silber, A., Smette, A., Sterzik, M., and Veyssiere, C. "Successful Commissioning of VISIR: the mid-infrared VLT instrument." *The Messenger* 117 (2004), 12-16.

Lee, D. B. "Anisotropic Etching of Silicon." *J. Appl. Phys.* 40 (1969): 4569-4574.

Livingston, F. M., Messoloras, S., Newman, R. C., Pike, B. C., Stewart, R. J., Binns, M. J., Brown, W. P., and Wilkes, J. G. "An infrared and neutron scattering analysis of the precipitation of oxygen in dislocation-free silicon." *J. Phys. C* 17 (1984): 6253-6276.

Loewen, E., Maystre, D., Popov, E., and Tsonev, L. "Echelles: scalar, electromagnetic, and real-groove properties." *Appl. Opt.* 34 (1995): 1707-1727.

Lord, R. C. "Far infrared transmission of silicon and germanium." *Phys. Rev.* 85 (1952): 140-141.

McDavitt, D., Ge, J., Miller, S., and Wang, J. "Silicon immersion gratings for very high resolution infrared spectroscopy." In *Optical Fabrication, Metrology, and Material Advancements for Telescopes: Proc. SPIE Vol. 5494*, edited by Eli Atad-Ettedgui and Philippe Dierickx, 536-544, 2004.

MacFarlane, G. G., McLean, T. P., Quarrington, J. E., and Roberts, V. "Fine Structure in the Absorption-Edge Spectrum of Si." *Phys. Rev.* 111 (1958): 1245-1254.

Madou, M. *Fundamentals of Microfabrication*. Boca Raton: CRC Press LLC, 1997.Mahajan, V. N. *Optical Imaging and Aberrations, Part II*. Bellingham: SPIE Press, 2001.

Marsh, J. P., Ershov, O. A., and Jaffe, D. T. "Silicon grisms and immersion gratings produced by anisotropic etching: testing and analysis." In *IR Space Telescopes and Instruments: Proc. SPIE Vol. 4850*, edited by John C. Mather, 797-804, 2003.

Marsh, J. P., Mar, D. J., and Jaffe, D. T. "Silicon Diffraction Gratings as Immersion and Front-Surface Devices." In preparation. 2006.

Matthews, K. and Soifer, B. T. "The near infrared camera on the W. M. Keck telescope", *Experimental Astronomy* 3 (1994): 77-84.

McCaulley, J. A., Donnelly, V. M., Vernon, M., and Taha, I. "Temperature dependence of the near-infrared refractive index of silicon, gallium arsenide, and indium phosphide." *Phys. Rev. B* 49 (1994): 7408-7417.

McLean, I. S., Becklin, E. E., Bendiksen, O., Brims, G., Canfield, J., Figer, D. F., Graham, J. R., Hare, J., Lacayanga, F., Larkin, J. E., Larson, S. B., Levenson, N. G., Magnone, N., Teplitz, H. I., Wong, W. "Design and development of

NIRSPEC: a near-infrared echelle spectrograph for the Keck II telescope." In *Infrared Astronomical Instrumentation: Proc. SPIE Vol. 3354*, edited by Alfred M. Fowler, 566-578, 1998.

Mele, T. C., Nulman, J., and Krusius, J. P. "Selective and anisotropic reactive ion etch of LPCVD silicon nitride with CHF_3 based gases." *J. Vac. Sci. Technol. B* 2 (1984): 684-687.

Merveille, C. "Surface quality of {111} side-walls in KOH-etched cavities." *Sensors and Actuators A* 60 (1997): 244-248.

Nanz, G. and Camilletti, L. E. "Modeling of Chemical-Mechanical Polishing: a Review." *IEEE Trans. Semiconductor Manufacturing* 8 (1995): 382-389.

Neuringer, L. J. "Effect of Pressure on the Infrared Absorption of Semiconductors." *Phys. Rev.* 113 (1959): 1495-1503.

Nevière, M. "Electromagnetic study of transmission gratings." *Appl. Opt*. 30 (1991): 4540-4547.

Newport Corporation, Diffraction Gratings Catalog, available from http://www.newport.com, 2005.

Palik, E. D., Glembocki, O. J., Heard, Jr., I., Burno, P. S., and Tenerz, L. "Etching roughness for (100) silicon surfaces in aqueous KOH." J. *App. Phys.* 70 (1991): 3291-3300.

Palmer, E. W., Hutley, M. C., Franks, A., Verrill, J. F., and Gale, B. "Diffraction gratings." *Rep. Prog. Phys*. 38 (1975): 975-1048.

Philippe, P., Valette, S., Mata Mendez, O., and Maystre, D. "Wavelength demultiplexer using echelette gratings on silicon substrate." *Appl. Opt.* 24 (1985): 1006-1011.

Pitris, C., Bouma, B. E., Shiskov, M., and Tearney, G. J. "A grism-based probe for spectrally encoded confocal microscopy." *Opt. Express* 11 (2003): 120-124.

Rayner, J. T. "Evaluation of a solid KRS-5 grism for infrared astronomy." In *Infrared Astronomical Instrumentation: Proc. SPIE Vol. 3354*, edited by Alfred M. Fowler, 289-294, 1998.

Reimann, H.-G., Weinert, U., and Wagner, S. "TIMMI2: a new MIR multimode instrument for ESO." In *Infrared Astronomical Instrumentation: Proc. SPIE Vol. 3354*, edited by Alfred M. Fowler, 865-876, 1998.

Runyan, W. R. *Silicon Semiconductor Technology*, McGraw-Hill, 1965.

Sato, K., Shikida, M., Yamashiro, T., Tsunekawa, M., and Ito, S. “Roughening of single-crystal silicon surface etched by KOH water solution.” *Sensors and actuators A* 73 (1999): 122-130.

Schroder, D. K., Thomas, R. N., and Swartz, J. C. "Free Carrier Absorption in Silicon." *IEEE Journal of Solid-State Circuits* 13 (1978): 180-187.

Schroeder, D. J. and Hilliard, R. L. "Echelle efficiencies: theory and experiment." *Appl. Opt.* 19 (1980): 2833-2841.

Seidel, H. “The mechanism of anisotropic electrochemical silicon etching in alkaline solutions.” In *Technical Digest: IEEE Solid-State Sensor and Actuator Workshop*, 86-91. Held at Hilton Head Island, SC, USA, June 4-7, 1990.

Seidel, H., Csepregi, L., Heuberger, A., and Baumgartel, H. "Anisotropic etching of crystalline silicon in alkaline solutions--part I. orientation dependence and behavior of passivation layers." *J. Electrochem. Soc.* 187 (1990): 3612-3626.

Sica Jr., L. "High Resolution Diffraction Grating." U.S. Patent 4,475,792 (1984).

Smith, J.-D. T., Rinehart, S. A., Houck, J. R., Van Cleve, J. E., Wilson, J. C., Colonno, M. R., Schoenwald, J., Pirger, B., and Blacken, C. "SCORE 1+: enhancing a unique mid-infrared spectrograph." In *Infrared Astronomical Instrumentation: Proc. SPIE Vol. 3354*, edited by Alfred M. Fowler, 798-809, 1998.

Spitzer, W. and Fan, H. Y. "Infrared Absorption in n-Type Silicon." *Phys. Rev.* 108 (1957): 268.

Stroke, G. W. "Diffraction gratings." In *Handbuch der Physik* 29, 1967: 426-758.

Sze, S. M. *Physics of Semiconductor Devices*. New York: John Wiley and Sons, 1981.

Tan, S. S., Reed, M. L., Han, H., and Boudreau, R. "Mechanisms of Etch Hillock Formation." *J. Microelectromech. Sys.* 5 (1996): 66-72.

Tearney, G. J., Webb, R. H., and Bouma, B. E. "Spectrally encoded confocal microscopy." *Opt. Lett.* 23 (1998): 1152-1154.

Thompson, L. F., Willson, C. G., and Bowden, M. J. editors. *Introduction to Microlithography*, 2nd ed. Oxford: Oxford University Press, 1994.

Tournois, P. "New diffraction grating pair with very linear dispersion for laser pulse compression." *Electron. Lett.* 29 (1993): 1414-1415.

Tsang, W. T. and Wang, S. "Preferentially etched diffraction gratings in silicon." *J. Appl . Phys.* 46 (1975): 2163-2166.

Tull, R.G., MacQueen, P.J., Sneden, C., and Lambert, D.L. “The high-resolution cross-dispersed echelle white-pupil spectrometer of the McDonald Observatory 2.7-m telescope.” *Publications of the Astronomical Society of the Pacific* 107 (1995): 251-264.

Van Gelder, W. and Hauser, V. E. "The etching of silicon nitride in phosphoric acid with silicon dioxide as a mask." *J. Electrochem. Soc.* 114 (1967): 869-872.

Vitali, F., Cianci, E., Foglietti, V., and Lorenzetti, D. “Fabrication of silicon grisms.” In *Specialized Optical Developments in Astronomy:Proc. SPIE Vol. 4842*, edited by Eli Atad-Ettedgui and Sandro D'Odorico, 274-281, 2003.

Vitali, F., Cianci, E., Lorenzetti, D., Foglietti, V., Notargiacomo, A., Giovine, E., and Oliva, E. “Silicon grisms for high-resolution spectroscopy in the near infrared.” In *Optical and IR Telescope Instrumentation and Detectors: Proc. SPIE Vol. 4008*, edited by Masanori Iye and Alan F. Moorwood, 1383-1394, 2000.

Wiedemann, G. R., Dave, H. H., and Jennings, D. E. "Immersion grating and etched gratings for infrared astronomy." In *Infrared Detectors and Instrumentation: Proc. SPIE Vol. 1946*, edited by Albert M. Fowler, 622-628, 1993.

Guenther Wiedemann, Bernard Delabre, Gotthard Huster, Alan F. Moorwood, Barbara Sokar. “High-resolution infrared echelle spectrograph (CRIRES) for the VLT.” In *Optical and IR Telescope Instrumentation and Detectors: Proc. SPIE Vol. 4008*, edited by Masanori Iye and Alan F. Moorwood, 1076-1083, 2000.

Wiedeman, G. and Jennings, D. E. "Immersion grating for infrared astronomy." *Appl. Opt.* 32 (1993): 1176.

Wynne, C. G. "Doubling spectral resolution." *Mon. Not. R. Astr. Soc*. 250 (1991): 796-801.

Zhao, F., Qiao, J., Deng, X., Zou, J., Guo, B., Collins, R., Villavicencio, V., Chang, K. K., Horwitz, J. W., Morey, B., and Chen, R. T. "Reliable grating-based wavelength division (de)multiplexers for optical networks." *Opt. Eng.* 40 (2001): 1204-1211.

Vita

Jasmina Pozderac Marsh was born in Banjaluka, Bosnia and Herzegovina, to Nadira and Ibrahim Pozderac on October 3, 1974. She completed high school at Gimnazija, Banjaluka, Bosnia and Herzegovina in 1993. After completing the freshman year at the University of Banjaluka, she emigrated to the United States and continued her education first at Brookhaven College, Farmers Branch, Texas and then at the University of Texas at Dallas where she received a Bachelor of Science degree in Physics in 1998 and a Master of Science Degree in Physics in 1999. In 1999, she entered the Department of Astronomy at the University of Texas at Austin. In 2001, she entered candidacy for the Doctor of Philosophy degree in Astronomy at the University of Texas at Austin.

Permanent address: 8210 Nairn Dr
Austin, TX 78749

This dissertation was typed by the author.